University of Nottingham
UK | CHINA | MALAYSIA

Creating Folic Acid Conjugated Gold Nanoclusters for Cancer Treatment

Miss Zhimin Liu

Ph.D. Thesis

School of Chemistry

2014-2018

Supervisor: Prof. Neil R. Thomas

Dr. Lyudmila Turyanska

Abstract

Gold nanoparticles and nanoclusters are widely researched due to their unique optical and electric properties and are size-limit being considered for bio-applications. These properties are predominantly distinctive in ultra-small thiol stabilized gold nanoclusters (Au NCs) and been significantly studied over the past decades. The proposed magnetic property make Au NCs a more promising candidate for bio-imaging and therapy including drug delivery and thermotherapy. However, its intrinsic magnetic property was poorly investigated. This project focuses on the investigation of biocompatible Au NCs with magnetic property.

By using as a capping agent, a bidentate ligand made of thioctic acid anchoring groups appended with a poly (ethylene glycol) short chain (TA-PEG), water-soluble gold nanoclusters with diameter of 1.7 ± 0.4 nm have been produced in a single-step aqueous reduction of gold precursors. A functionalized folic acid (FA) conjugated ligand (FA-PEG-TA) has been obtained and used to synthesize Au NCs with diameter of 1.6 ± 0.3 nm. Both targeting and non-targeting Au NCs solutions demonstrated good long-term colloidal stability, high thermal-stability (at T = 40 ºC, 50 ºC) and are

stabilized over a wide range of pH values pH 3-11 for non-targeting and pH 7-11 for folate derivatives. They were also found be paramagnetic by analyzing relaxation time T_1 of adjacent capping ligands attached to the Au NCs surface.

Both Au NCs were found to have low toxicity for MCF-7, a breast cancer cell line and HCT-116, a human colon cancer cell line in cell viability assays. In addition, FA-Au NCs showed a greater uptake by folate receptor (FR) -positive MDA-MB-231(human breast cancer cells) than PEG-Au NCs by three repeated experiments with results analyzed by Inductively coupled plasma mass spectrometry (ICP-MS). These findings demonstrated that the synthesized paramagnetic water-soluble Au NCs are promising biocompatible candidate for cancer treatment.

Acknowledgements

Firstly, I would like to express my sincere gratitude to my supervisors Dr. Lyudmila Turyanska and Prof. Neil R. Thomas for their continuous support of my Ph.D study and research, to their patience, motivation, encouragements and immense knowledge. Their detailed guidance helped me in both my academic work and life.

For their help with this project during my Ph.D. period, I also would like to acknowledge and thank Dr. Tracey D. Bradshaw, Dr. Huw E. L. Williams, Dr. Scott Young, Dr. Fabrizio Moro, and Dr. Michael W. Fay, who gave access to their laboratory and research facilities. Without their helpful support it would not be possible to conduct my research.

I would like to express appreciate to my *viva* examiners, Professor Paola Borri from Cardiff University and Dr. Graham Newton from University of Nottingham, for their precious time and valuable suggestions for my thesis and in-depth discussion during the *viva*.

I thank my fellow labmates Dr. James Krupa, Dr. Alex Wichlacz, Dr. David Harvey,

Mr. Mohammed Alnajjar, Matthew Stevenson, Mohammed Al-Obaidi, Malcolm Lamont, Tom Armstrong, Parisa Hamzavinejad Moghaddam and the whole NRT group for the discussions and all the fun we have had in the last four years. In particular, I am grateful to Dr. Francesco Zamberlan for enlightening me, with the first experience of organic research. I thank my friends: Xue Wu, Lingqiao, Wu, Lei Yang, Zhenyu Wang, Guanyu Wang, Yidong Liu, Xiaolu Pu, Thien Duong, Renna, Dr. Xuezhong Sun, Dr. Jie Ke for their accompany in Nottingham. Also, I thank my master's supervisor Prof. Luan and her group in ECUST for their support during my staying in Shanghai.

I would like to thank all my family members, my dear parents for their unconditional love and encouragement that brought me be where I am today and my little brother Zhipeng.

Finally, I would acknowledge access to facilities and services provided by University of Nottingham, School of Chemistry, Centre Biomolecular Science, Nano-Micro Research Centre and funding support from China Scholarship Council and the University of Nottingham.

Publication lists

1. F. Zamberlan, L. Turyanska, A. Patanè, **Z. Liu**, H. E. L. Williams, M. W. Fay, P. A. Clarke, Y. Imamura, T. Jin, T. D. Bradshaw, N. R. Thomas and A. M. Grabowska, Stable DHLA–PEG capped PbS quantum dots: from synthesis to near-infrared biomedical imaging. *Journal of Materials Chemistry B* **2018**, 6, 550-555.

2. **Z. Liu,** L. Turyanska, F. Zamberlan, T. Bradshaw, S. Young, F. Moro, M.W. Fay, H. E. L. Williams, and N. R.Thomas, Synthesis of folic acid functionalized gold nanoclusters for targeting folate receptor-positive cells. (Submitted, **2018**).

Abbreviations

Au NCs	Gold Nanoclusters
BSA	Bovine Serum Albumin
CLSM	Confocal Laser Scanning Microscopy
CT	Computed Tomography
DCM	Dichloromethane
DFT	Density Functional Theory
DHLA	Dihydrolipoic Acid
DLS	Dynamic Light Scattering
DMF	Dimethylformamide
DNA	Deoxyribonucleic Acid
DSC	Differential Scanning Calorimetry
EA	Elemental Analysis
EPC	Endothelia Progenitor Cells
ESI	Electrospray Ionization
FA	Folic Acid
FLIM	Fluorescence Lifetime Imaging
FR	Folate Receptors
FRET	Förster Resonance Energy Transfer
GFP	Green Fluorescent Protein
GSH	Glutathione
HAADF	High-Angle Annular Dark-Field
HAEC	Human Aortic Endothelial Cells
HCT	Human Colon Cancers Cells
HER2	Human Epidemal Growth Factor Receptor 2
HIV	Human Immunodeficiency Virus
HNPs	Heating Nanoparticles
HOMO	Highest Occupied Molecular Orbital
HRTEM	High Resolution Transmission Electron Microscopy
HSAB	Hard Soft Acid Base
HT	Hyperthermia Treatment

ICP-AES	Inductively Coupled Plasma Atomic Emission Spectroscopy
ICP-MS	Inductively Coupled Plasmon – Mass Spectrometry
IR	Infrared Spectroscopy
L-HNPs	Light-Heating Nanoparticles
LUMO	Lowest Unoccupied Molecular Orbital
MALDI	Matrix-assisted Laser Desorption
MBA	Mercaptobenzoic Acid
MCF-7	Michigan Cancer Foundation-7, A Breast Cancer Cell Line
M-HNPs	Magnetic-Heating Nanoparticles
MNPs	Magnetic Nanoparticles
MP-LSM	Multiphoton Laser Scanning Microscopy
MRI	Magnetic Resonance Imaging
MS	Mass Spectrometry
MTT	3-(4,5-Dimethylthiazol-2-yl)-2,5-diphenyltetrazolium bromide
MW	Molecular Weight
NCs	Nanoclusters
NMR	Nuclear Magnetic Resonance
NPs	Nanoparticles
PEG	Poly (ethylene glycol)
PTFE	Polytetrafluoroethylene
PTT	Photo Thermal Therapy
QDs	Quantum Dots
RPMI	Roswell Park Memorial Institute
SPDM	Spectral Position Determination Microscopy
SPR	Surface Plasmon Resonance
SQUID	Superconducting Quantum Interference Device
TA/LA	Thioctic Acid/Lipoic Acid
TEM	Transmission Electron Microscopy
TGA	Thermo-gravimetric Analysis
THF	Tetrahydrofuran
TLC	Thin-layer Chromatography
TOAB	Tetra-octylammonium Bromide

UV/Vis	Ultraviolet/visible
XMCD	X-ray Magnetic Circular Dichroism Spectroscopy
XPS	X-ray Photoelectron
XRD	X-ray Diffraction

Contents

Chapter 1

Introduction

Nanomaterials are of interest for applications in biotechnology, medicine, pharmacy, material sciences, computer sciences, engineering and environments.[1-6] The concept of nanoscience was first presented by Nobel laureate Richard P. Feynman in his lecture "There's Plenty of Room at The Bottom" in 1959.[7] The size, shape and composition are important for nanomaterials since they influence their physical and chemical properties.

Nanoparticles are materials with size ranging from 1 to 100 nm, possessing unique chemical and physical properties due to having a large surfaces area and nanoscale size.[8] They can be classified into groups as carbon NPs,[9] metal NPs,[10] ceramic NPs,[11] semiconductor NPs[12] and polymeric NPs.[13] Fabrication of NPs can be divided into two main types: the bottom-up approach and the top-down approach.[14] Among them, the colloidal synthesis method attracts more attention due to its cost-effectiveness, flexibility of the processes and scalability.[15]

Among different types of NPs, metal NPs are well-known for their localized surface plasmon resonance (LSPR) properties that result in a distinctive optoelectrical ability. The LSPR phenomenon is a collective oscillation of free electrons in nanosized structures of metals (*e.g.* Au, Ag, Cu, Al, *etc.*), resonantly induced by incident photons.[16]

Au NPs have been widely researched over the past few decades, mainly due to their high physical and chemical stability, good biocompatibility, easily functionalization surface and multi-optical properties related to surface plasmon.[17-19] The earliest known example of a gold nanomaterial dates back to the 4th century AD, when it was used for staining glass. An example of this is the Lycurgus cup, which is on display in the British Museum. The record of scientific study of gold nanomaterials starts with the report by Faraday in 1850s,[20] who reported that illuminating a liquid with a beam of light: "The cone was well defined in the fluid by the illuminated particles". These were gold nanoparticles of nano-crystalline face-centered cubic structured crystals with size smaller than 100 nm. Spherical AuNP solutions display a range of colours from brown to orange, red and purple for NPs with diameter from 1 to 100 nm. Examination of the absorption profile reveals a size-dependent absorption peak in the range of 500 to 550 nm (Figure 1.1).[21]

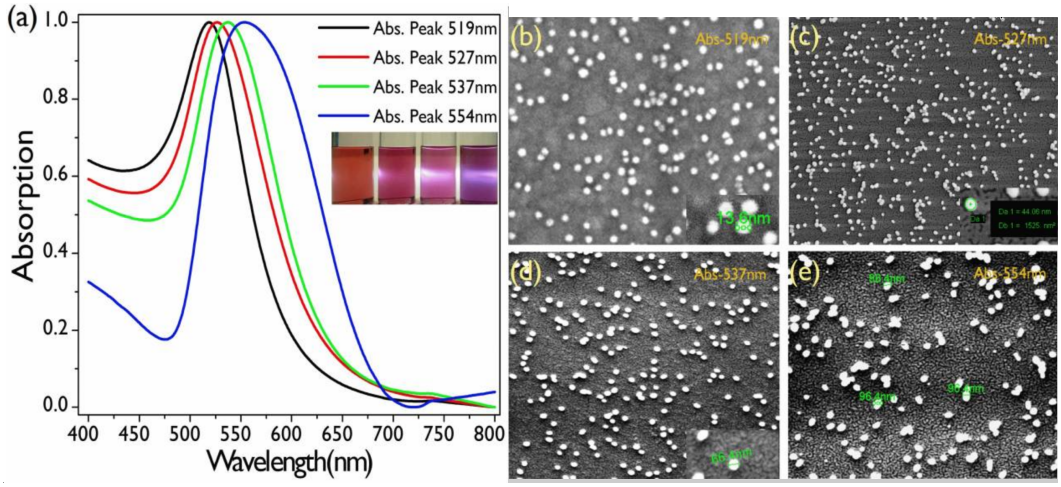

Figure 1.1 (a) The absorption spectra of the colloidal gold nanoparticles in water having different sizes **(Inset)** A photograph of the AuNP solutions. SEM images of colloidal gold nanoparticle of various sizes on substrate with average sizes of **(b)** 13nm, **(c)** 45nm, **(d)** 66nm, and **(e)** 96nm.[21]

1.1 Gold nanoclusters

Gold nanoclusters (Au NCs) are NP with $d < 2$ nm,[22] which are characterized by the absence of a surface plasmon band due to the loss of their metallic nature. Au NCs with certain number of Au atoms, such as Au_{25}, Au_{38}, Au_{64}, Au_{102}, Au_{144} are referred to "magic number clusters". These clusters have complete outer shell of face-centered cubic (fcc) lattice and hence have high stability and monodispersity.[23] These unique phenomenon are mainly originated from two aspects: the electronic shell and the geometric structures. Magic numbers of alkali-metal nanoclusters based on electronic shells were initially observed in mass spectra by Knight *et al.* in 1984.[24] Which now can be well explained by the spherical jellium model, the delocalized valence electrons

occupied shells.[25]. Regarding the geometric structures, it is the magic nanocluster's ability to minimize the surface energy with highly symmetricity arrangements. The shape of Au NCs is supposed to be polyhedral, which are classified as icosahedra and fcc polyhedral.[26] Mori *et al,*[26] proposed that "magic number" Au NCs usually have regular icosahedral shape shown in Fig 1.2. Li *et al.* reported that both Density Functional Theory (DFT) and empirical model calculations suggested that the icosahedral structure is more stable than either decahedral or FCC for Au_{147}.[27]

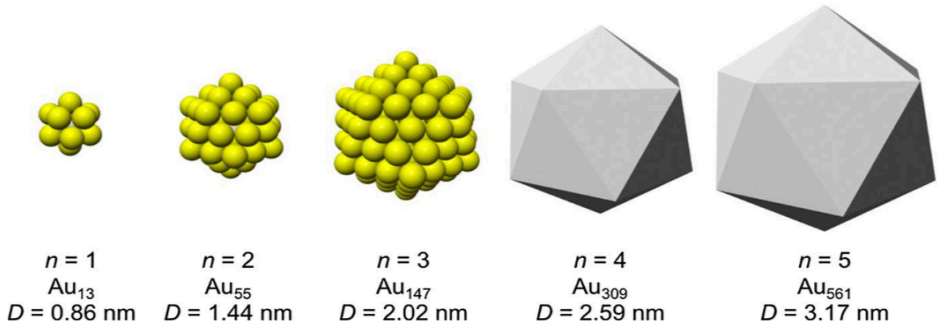

Figure1.2 An illustration of Au nanoparticles formed with a magic number of Au atom and estimated diameter based on regular icosahedral shape.[26]

AuNCs exhibit unique properties, such as discrete, molecule-like energy levels and tunable optical properties.[22] Moreover, Au NCs have several attractive features including optical chirality,[28, 29] stable fluorescence,[30-33] low toxicity and high biocompatibility[34] and are predicted to have, unexpectedly for metals, magnetic properties.[35] These properties make Au NCs a promising candidate for applications in catalysis,[36] biosensors,[37] biomarker detection[38] as well as for use in light harvesting,[39, 40] magnetic ablation[41] and bio-imaging.[32]

The combined optical and magnetic properties that make Au NCs a particular interest in the field of medical imaging and localized hyperthermia. For applications in biomedicine, the following criteria should be met:[32] (i) Solubility in physiological solvents and low toxicity; (ii) Small size to facilitate the uptake and avoid perturbation of the biological system; (iii) Optimal photo-physical properties including low photo-bleaching, absence of blinking and high quantum yield; (iv) Targeting to specific tissue or cell types.

To date, organic dyes,[42] GFP-like fluorescent proteins,[43] quantum dots[44] and gold nanoparticles have been researched widely for *in vivo* imaging. Organic dyes have bright fluorescence, however low photo-stability limits their application in long-term tracking, also their small Stokes shift restricts their multicolour imaging application.[44] GFP-like fluorescent proteins have the key advantage of being non-toxic and can be genetically encoded so that the labels will be produced by cells themselves; however, their photo-stability and emission wavelength range are very limited.[45] Hence, inorganic nanomaterials, such as semiconductors quantum dots are used to achieve stable and tunable photoluminescence. Concerns are currently raised about the possible leakage of heavy metals from QDs and their clearance from the body.[46-47] Au NCs have the potential to overcome all the limitations mentioned.

Au NCs with diameter $d < 2$ nm have high quantum yields of $\sim 10^{-1}$.[38, 48] The fluorescence emission of gold nanoclusters can be tuned from visible into infrared region (300 - 800 nm) by changing size and ligand composition,[30,49] and their photo-

stability was demonstrated to be proved 5 times greater than that of organic dyes.[50-51]

1.2 Synthesis and properties of gold nanoclusters

1.2.1 Synthesis of Au NCs

Two main routes to fabricate gold nanoclusters have been reported: the physical etching method (dry route); and the chemical reduction method (wet route).[52] In the dry route, gold nanoclusters are produced by etching large gold nanoparticles with thiols[53, 54] or multivalent polymers as ligands.[55] This method has multiple steps and is a time-consuming procedure, it will also generate NPs with a wide size range.

The chemical reduction method of making gold nanoclusters can be performed in both polar and non-polar solvents. Typically, dissolved precursor salts of Au (III) or Au (I) are reduced to Au (0) by a reducing agent in the presence of capping ligands.[17] Capping ligands bind to the surface gold atoms of the nanoclusters, which act as electron donors (Lewis acid). The commonly used ligands are carboxylic acids, amines, phosphines and thiols, whereas the ligand-to-metal binding strength follows the order O < N < P < S, according to Pearson's Hard Soft Acid Base (HSAB) concept.[56] Typical reducing agents are, tri-sodium citrate ($Na_3C_6H_5O_7$), and sodium borohydride ($NaBH_4$), and are selected depending on the desired size of nanoclusters and polarity of solvent used. Strong reducing agents induce a high nucleation rate rather than a high growth rate, thus leading preferentially to the formation of ultra-small gold nanoclusters.[17, 55, 57]

In 1994, Brust published a method that been referred to as the Brust-Schiffrin synthesis (Figure 1.3).[58] In this two-phase method, chloroauric acid is dissolved in deionized water, mixed with alkythiol capping ligands dissolved in organic solvent (*e.g.* toluene) with assistance of phase transfer agents (*e.g.* tetra-octylammonium bromide, TOAB), and reduced with aqueous $NaBH_4$ solution. In 1995, a one-phase method was proposed, in which methanol acts as the solvent for all of chemicials.[59]

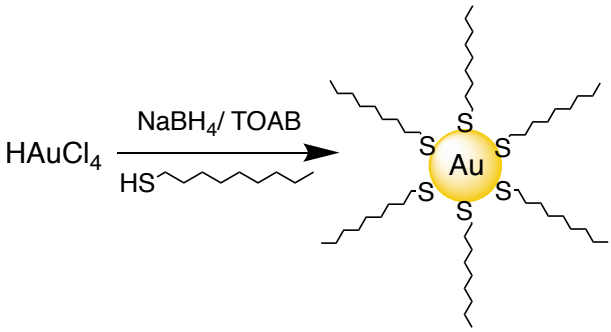

Figure 1.3 Scheme of the Au NCs synthesis.[58]

Significant efforts have been made to synthesize gold nanoclusters with precise number of atoms and to determine their metal core atom-packing structures as well as binding ligands arrangements.[26-34]

To date, Au NCs have been produced with atom numbers of 20, 24, 25, 36, 38, 44, 55, 64, 144.[54, 60-67] The gold nanoclusters passivated by thiolate Au_{25}, Au_{38}, Au_{144} can be produced by direct synthesis without post-synthetic size separation and are considered to be the most stable clusters.[54] These numbers are called “magic numbers” because of their extraordinary stable properties. The electronic states or the crystal structures are proposed to explain this phenomenon, however, deeper understanding is still

needed.[68]

Phosphine and phosphine/thiolate are also used to stabilize nanoclusters. In 1969, McPartlin[69] first synthesized $Au_{11}(PPh_3)(SCN)_3$. Mingo *et al*. predicted the centered icosahedral Au_{13} cluster,[70] which was later successfully synthesized in 1981.[71-73] Pettibone *et al*. obtained even smaller clusters of $[Au_9L^6_4Cl]^{2+}$((L^6 = 1,6-bis (diphenylphosphino) hexane).[74]

1.2.2 Importance of capping ligands

Capping ligands determine and stabilize the NP size and help to solubilize them in a solvent. Colloidal nanoparticles can be designed to disperse in either a polar (*e.g.* water-based) or in a non-polar organic solvent (*e.g.* toluene), while amphiphilically capped nanoparticles can be dispersed in both kind of solvents.

Ligands play an important role in NP colloidal stability and the process of nanocluster growth. Ligands bind to the NP surface and prevent their aggregation by electrostatic repulsive force or steric hindrance.[75]

Two types of ligands are normally used in Au NCs synthesis:

(i) Molecules with functional groups

Ligand molecules consist of an inert molecular chain (*e.g.* hydrocarbon chain or polyethylene glycol (PEG)) and have functional groups that terminate the molecules. PEG is one of the commonly used ligands, it is a linear polymer of various length

consisting of repeated units of $–[CH_2\text{-}CH_2\text{-}O]_n$-; PEG is soluble in a number of polar and non-polar solvents, and is used as an inert, biocompatible polymer.[76-78] In water, PEG is heavily hydrated and forms random coils. PEG-modified nanoparticles or drugs possess increased water solubility, high stability in solutions with high salt concentrations and in biologically-relevant environments, and reduced immunogenicity. They have an increased half-life in the blood stream due to weaker binding to antibodies, proteins and cells.[79-80]

Monofunctional PEG molecules, *e.g.* ended with methyl group, yield stable and inert particles. Bifunctional PEG molecules are used to introduce new functional groups on the NP surface. Recently, Qin *et al.*[81] produced a PEG stabilized Au NP linked to magnesium pyrophosphate crystals, for applications as a DNA detection probe.

(ii) Bio-molecules

Nanoparticles conjugates with biomolecules bring together the unique properties and functionality of both materials: tunable fluorescence or magnetic properties of the inorganic particles, and the ability of biomolecules for highly specific binding via molecular recognition.[82, 83] To date, various biomolecules have been used as capping ligands, such as lipids,[84] peptides,[85] sugars[86] proteins,[87] enzymes,[88] and DNA,[89] providing aqueous stability and solubility for Au NP, and functionalizing them for specific targeting.

1.2.3 Optical and morphological properties

Size-dependent quantization effects occur if a metal particle is small enough. Au NPs with core diameter above 2 nm show a local surface plasmon resonance effect which can be detected by UV-vis absorption at a wavelength of 520 nm. An oscillation of the conduction electrons forms as a result of plasmons on the nanoparticles' surface. In UV-Vis spectroscopy, an indication of polydispersity of the sample could be assessed from the width of the peak. Also, it has been proposed by Haiss[90] that size can be calculated directly from the visible absorption peak of UV-Vis, assuming that gold nanoparticles are spherical and have diameter of 5 to 100 nm. Furthermore, the determination of nanoparticle concentrations are allowed based on the analytical relations between the extinction efficiency and diameters.

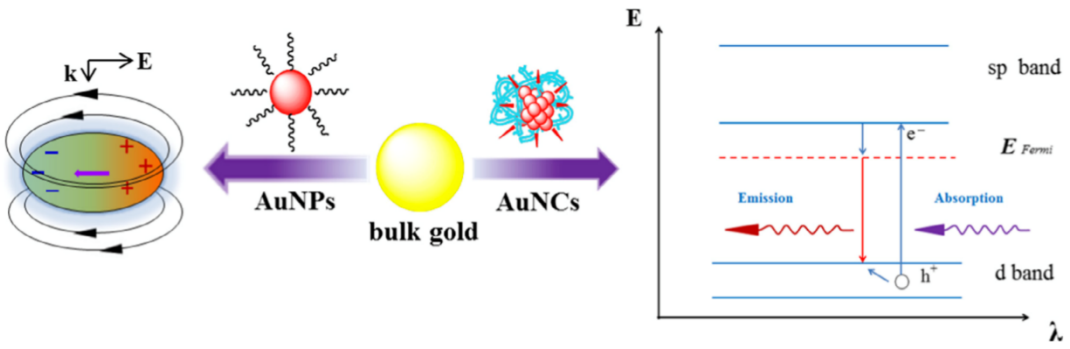

Figure 1.4 Surface localized plasmons and energy diagram of photoluminescence in gold nanoclusters.[91]

For nanoparticles with a core diameter of less than 2 nm, such as metal nanoclusters, no continuum of density of states is available and discrete electronic states are formed.

Au NCs have been observed to exhibit discrete electronic energy levels and the size regime (< 2 nm) is comparable to the Fermi level to the conduction electrons, so the surface plasmon band disappears and size-dependent fluorescence can be observed.[92] For example, the UV-vis spectra of monodisperse clusters of AuNCs are shown in Figure 1.5.[54] An smooth profile with surface plasmon band at 2.3 eV is expected for AuNP with size over 2 nm. However, spectra shown in Figure 1.5 are observed with various humps and sharp structures. This indicates that the HOMO-LUMO gap varies with different magic cluster number.[52] These unique profiles are regarded as fingerprints of the magic Au:SR clusters.

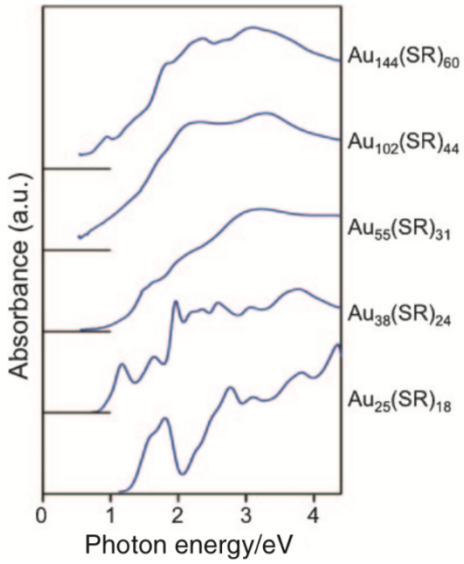

Figure 1.5 optical spectra of a series of magic Au:SR clusters.[93]

In general, for NP with d >2 nm, absorption peak is observed at the wavelength of ~ 520 nm and is attributed to surface plasmon resonance of NPs. However, this peak is not observed in the absorption spectra of monodispersed AuNCs with d < 2 nm . The

optical properties of AuNCs, absorption and emission, are highly depend on the size of the nanoparticles, shape, oxidation states and surface ligands. The absorption can be tuned in the range from 280 nm to 670 nm, and the fluorescence wavelengths can be in the range from visible to NIR region (400 nm to 800 nm).[94, 95].

For polydisperse Au NCs (d < 2 nm), the absorption were reported to be featureless in the visible range, increasing form the visible to the UV. Matthew *et al.* [96] produced a mixture of Au NCs (d < 2nm) including Au_{25}, Au_{38} Au_{68} Au_{102} and $Au_{144,}$ and observed smooth profile without any distinct absorption band (Figure 1.6).

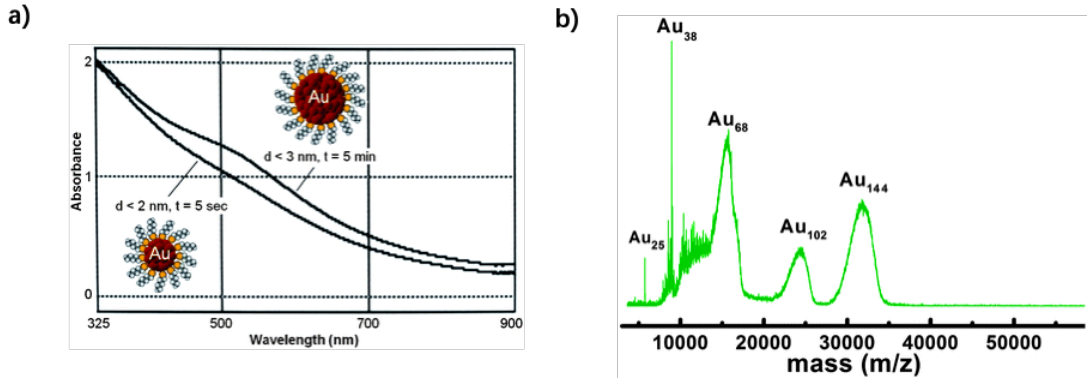

Figure 1.6 a) UV/Vis absorption spectra of hexanethiolate-coated AuNCs in hexane. **b)** Matrix Assisted Laser Desorption/Ionization- Time-of-Flight **(**MALDI-TOF) mass spectrum of magic numbered AuNCs.[96]

The densities of state and the energies of the particles depend on the size of the particles.[97] The fluorescence of Au NCs is originated from energy transition between HOMO (Highest Occupied Molecular Orbital) and LUMO (Lowest Unoccupied Molecular Orbital) states and can be tuned by the NC size in the range from 0.1 eV to 2.0 eV.[98] Their distinct optical properties are mainly attributed to the ultra-small sizes

and corresponding discrete electronic structure.[99] For polymer-stabilized Au NCs with diameter range from 1.1 nm to 1.7 nm, the fluorescence was observed with a quantum yield of ~ 3 %.[100] An alternative explanation was proposed by Apell *et al*., who suggested that the fluorescence properties of Au NCs arise from the charge recombination processes involving *d*-band orbitals.[101] The absorbed photons promote the electrons to an empty *sp* band above the Fermi level from the narrow *d* band. Ultra-small Au NCs show fluorescent properties that not only depend on their size but are also affected by type of ligands used. Huang *et al.*[102] investigated a 1.8 nm triopronin-Au NC and reported optical emission occurring at 700-800 nm, due to inter-band transitions between the filled 5 d^{10} band and 6$(sp)^1$conduction band.

It was proposed that the capping ligands also play an important role in enhancing the fluorescence in the thiol-protected Au NCs due to the electron transfer from a thiol to a surface gold atom *via* the Au-S bond.

For example, purine (-S-)-Au NCs exhibit green fluorescence at 520 nm.[103] Moreover, by replacing purine ligands with DHLA or BSA,[83, 104] red fluorescence at ~ 650 nm was achieved. Complementary opportunities arise from attachment of fluorophores to Au NCs. It was demonstrated that emissions of fluorophores close to the nanoclusters is quenched,[105] due to resonant energy transfer. Therefore, fluorescence spectroscopy can be used to explore the stability of the ligand shell. The properties of solvent affect ligand release, for example, 2 nm Au NCs were found to be prone to ligand shell insatiability for that cationic stabilized Au NCs are more labile compared to anionic

ones.[106]

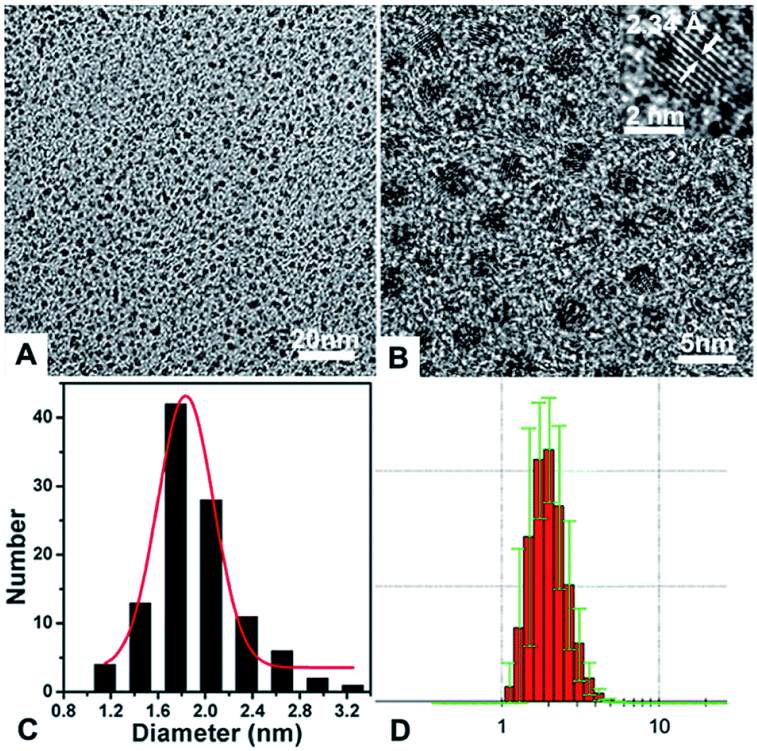

Figure 1.7 TEM **(A)** and HR-TEM images **(B)** of AuNCs. Histogram of the size distribution of AuNCs from HR-TEM **(C)** and from DLS results **(D)**.[107]

The Au NC morphology was extensively studied by high-resolution transmission electron microscopy (HRTEM) and dynamic light scattering techniques. As shown in Figure 1.7, the observed water-soluble Au NCs (capped by glutathione and citrate-GS/C) are spherical with diameter of ~ 1.8 nm, in a narrow size distribution. Analysis of the NCs morphology revealed high crystallinity and crystal lattice planes separation of 2.34 Å, corresponding to (111) plane of the face centered cubic Au.[107]

Exploring the NC surface is of key importance for understanding a NC's optical and magnetic properties. For analysis of the surfaces, X-ray photoelectron spectroscopy

(XPS) has been used to analyze the ligand shell of Au NCs. Tamura *et al.* investigated 1.7 nm sized Au NCs, capped with 2,2'-bis(diphenylphosphino)-1,1'-binaphthyl (BINAP), and confirmed the oxidation state of 0 for the gold atoms.[108] Boyen *et al.* determined an unexpectedly high oxidation resistance for Au_{55} clusters compared to smaller and larger Au NPs, relating this stability to the closed-shell structure of the Au_{55} clusters.[109]

1.2.4 Magnetic properties of Au NCs

Recently, multiple studies have emerged reporting magnetic behavior of nanoscale materials. This magnetism was observed in metal oxide nanoparticles (*e.g.* Fe_3O_4)[110] and nanocrystalline films, as well as in typically diamagnetic metal nanostructures (Au, Cu, Ag, Pt).[111]

The magnetic properties of the *d*-elements are a result of the electronic configuration of the *d* orbitals, where the number of unpaired electrons defines net magnetic moment. Single gold atoms (*e.g.* in gaseous state or absorbed on a support) are paramagnetic because of the unpaired 6s electron, while bulk gold is diamagnetic because the paramagnetism of the conduction electrons is counteracted by the orbital and ionic core diamagnetism.[112] Despite its gas-phase atomic electronic configuration of [Xenon]$4f^{14}5d^{10}6(sp)^1$, the band structure of gold and its calculated density of states predict an equal number of spin-up and spin-down electrons, hence diamagnetic property.[112] This predicted diamagnetism is in agreement with the experimentally observed negative value of magnetic susceptibility and diamagnetism of bulk gold.

Moreover, recently, Jin *et al.*[113] reported a reversible switching of paramagnetism in $Au_{25}(SR)_{18}$ at T = 5- 300 K, where R is phenylethyl, density functional theory (DFT) was used to assign the observed magnetism to the unpaired spin residing in the Kohn-Sham HOMO state of $Au_{25}(SR)_{18}$. Alfonso *et al.*[114] confirmed paramagnetism of $[Au_{25}(SR)_{18}]^0$ by ^1H and ^{13}C NMR studies and suggested that the paramagnetic behavior of $Au_{25}(SR)_{18}$ was arising from the Fermi-contact term confirmed by DFT calculations of chemical shifts. However, this results were contradicted by their follow up report of diamagnetic behaviour of $[Au_{25}(SR)_{18}]^+$,[115] where DFT-calculations of the evolution of the frontier orbitals had been used to supplement their conclusion that positive charge state (+1) must be considered diamagnetic due to a significant splitting of the HOMO energy level.

A large number of investigations of magnetism in gold nanoparticles were performed using SQUID magnetometers, however the results remain inconclusive, due to the complexity of the structure and need for corrections for various contributions (*e.g.* ligands).[116]

To gain further insights into this complex problem, X-ray magnetic circular dichroism (XMCD) was used to detect of the magnetic moments of an element through sensitivity to the difference between the up and down-spin densities around the Fermi level.[117] Yamamoto *et al.*[118] explored magnetization in 1.9 nm Au NP capped with polyallyl amine hydrochloride. The evidence of intrinsic spin polarization in gold nanoclusters was demonstrated with magnetic moments of ~ 0.13μB.

Various theories have been put forward to explain the magnetic properties of Au (and other metallic) nanoparticles.[112] The current leading theories, suggest that magnetism could result from:

(i) the predominant effect of surfaces at the nanoscale;

(ii) the strong modification to gold from strongly capping molecules, like thiols;

(iii) the strong spin-orbit coupling of gold.

Of particular interest is interaction of metal ions with ligands. As suggested by Li *et al.*,[119] the magnetic properties of capped Au NPs originate from the strong chemical affinity of Au atoms to the capping molecules. Strong interaction between thiols and gold induces a noticeable charge redistribution. The observation of magnetic moments in thiol-capped Au NPs is also associated with the *5d* localized holes created through the covalent Au-S bonding between the surface Au atoms and S atoms of the capping thiol.[111] The strong affinity between them can induce a noticeable charge transfer from the surface of Au atoms to the S atoms. As a result, the electrons of the surface Au atoms will be redistributed to induce hybridization between the *5d* and *6s* orbitals, such that the energy of *5d* electrons is closer to the Fermi level. Consequently, unoccupied *d* states are created in the surface Au atoms, leading to the observation of magnetism.

Ayuela *et al.*[120], used first-principle calculations to show that in the S-Au bond, an electron is transferred to the Au cluster. This extra electron is mainly *sp* and at an electronic shell below the NC surface, hence subsurface gold atoms hold unpaired

electrons leading to the magnetic moments in Au NC.

1.3 Cytotoxicity and cellular uptake of gold nanoparticles

1.3.1 Cytotoxicity study of nanoparticles

An understanding of the interaction between nanoparticles and biological systems is of significant interest. The prototypical nanoparticles are produced by chemical synthesis, and are coated with polymers, drugs, fluorophores, peptides, proteins, or oligonucleotides and eventually administered into cell cultures or animal models.[121] Nanoparticles were suitable used as drug carriers, however, there is a growing number of concerns over the potential risks of nanomaterials to human health and safety.[122] Biophysical responses to the uptake of nanomaterials can include conformational changes in biomolecules including DNA and proteins, and changes to the cellular membrane and the cytoskeleton. Changes to the latter two can induce changes in cell elasticity, morphology, motility, adhesion and invasion.[121] Several factors influence nanoparticle-cell interactions at the nano-bio interface, such as size, shape, charge of the nanoparticles, the ligand density, receptor expression levels, the internalization mechanism, the cell properties including phenotype and location.

As shown in Figure 1.8, nanoparticles can interact with the cell surface membrane in multiple scenarios.[123] The ligand-coated nanoparticles can bind to receptors on the membrane and induce a signalling cascade without entering the cell. Also, the ligand-coated nanoparticles can be internalized and exocytosed by the cell, without ever

leaving the vesicle, and then exit from the cell. Another pathway is internalization of nanoparticles that can escape the vesicle and interact with various organelles. They bind to membrane receptors, enter the cell, and target subcellular structures. The nonspecific interaction with the cell membrane could also be followed by internalization.

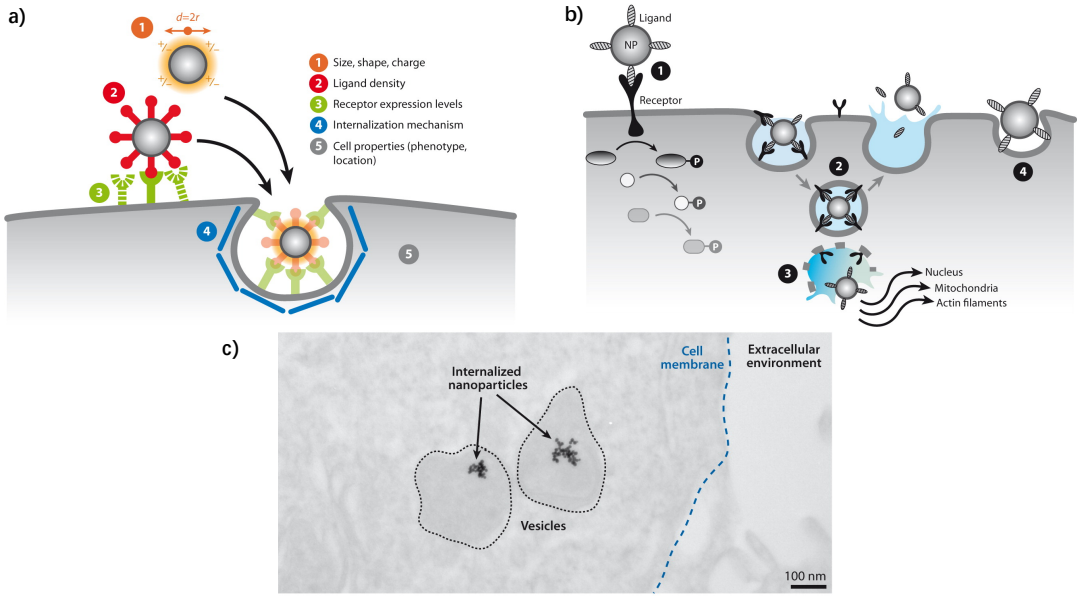

Figure 1.8 a) Schematic representation of factors that can influence nanoparticle-cell interactions at the nano-bio interface. **b)** Ligand-coated nanoparticles interacting with cells. **c)** Multiple transferrin-coated 15-nm gold nanoparticles are internalized by HeLa cells into intracellular vesicle.[123]

1.3.2 Detection of intracellular uptake of gold nanoparticles

With an increasing interest in gold nanoparticles, it is important to understand the interaction of gold nanoparticles with the cellular environment. As the NPs enter the biological environment, a so-called 'protein-corona' is formed by absorption of

dissolved biomolecules. The interaction of NP with cells are determined by this biomolecular layer.[124] Generally, mechanisms of two active and one passivate are proposed for the NPs internalization by cells. In activate methods, NPs are encapsulated in vesicles and transported into cells *via* endocytosis: pinocytosis (drinking by cells) or phagocytosis (eating by cells).[125] Most cells are able to conduct pinocytosis of NPs up to several hundred nanometers. Surface exposed functional groups on NPs can be recognized by cell surface receptors and activate the cell's uptake machinery. Specialized cells, such as macrophages, neutrophils, and monocytes are capable of phagocytosis of micro-sized particles by totally engulfing with their plasma membrane.[126] For cell types that completely lack the endocytosis machinery such as red blood cells, NPs are internalized by passive penetration.[127] Cellular uptake studies are performed to explore and qualify these interactions. Several methods were proposed to detect the intracellular behavior of nanoparticles, such as confocal laser scanning microscopy, transmission electron microscopy and fluorescence microscopy.

1.3.2.1 Photoluminescence microscopy

Photoluminescence is regarded as a distinct property of gold nanoclusters, which arises from the transition between the HOMO and LUMO energy state. Au NCs display longer emission lifetimes (from hundreds of nanoseconds to microseconds) compared to other plasmonic nanoparticles.[128,129] The long lifetime enables to minimize the autofluorescence interference in biological samples through time-resolved luminescence techniques.[130]

To date Au NP were successfully used for early-tumor diagnostics and pharmacokinetics tracking, where accurate *in vivo* localization of functionalized gold-nanoparticles was achieved.[131] Au NCs were recently used in sensing for detection of heavy metal ions, small biomolecules or proteins.[94]

Confocal laser scanning microscopy (CLSM) is used for imaging of cell or tissue samples and operates by laser scanning on an optical platform. The images are obtained at higher resolution with depth selectivity.[132] The key advantage of CLSM is its ability for optical sectioning in which the images are reconstructed based on the point-by-point scanning, and the 3-D structure of the superficial interior can be reconstructed. Overall, the quality of the images is greatly enhanced due to the unique sectioning method of the laser, and the information from the out-of-focus field is not superimposed on the image in focus. Also, most of the traditional imaging techniques have the disadvantages of tissue distortion, due to tissue fixation and sectioning and exposure to the light beam. The CLSM enables imaging of the intact and/or viable sample, hence enabling visualization of actual process.[133]

Fluorescence confocal microscopy and its derivatives (*e.g.,* multiphoton laser scanning microscopy (MP-LSM)), are still an irreplaceable tool for non-invasive visualization of live cell uptake of nanoparticles in real time.[76,134]

Fluorescence image of Au NCs' cellular uptake can be acquired using purine-stabilized Au NCs (with hydrodynamic diameter of 2.6 ± 0.7 nm) targeting cell nuclei. Images were recorded at 510 nm. As shown in Figure 1.9, The AuNCs targeted nuclei with

green emission are differentiated with the deep red plasma membrane dyes stained compartments of cells.[103]

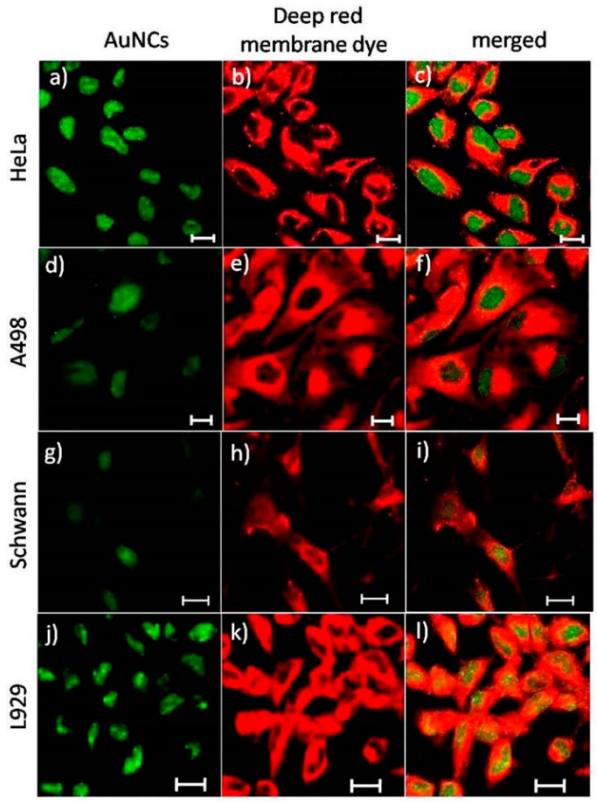

Figure 1.9 Confocal scanning microscopy images of four different cell lines following exposure to AuNCs (λ_{em} = 510 nm). Cell cytoplasm was stained with red dye ((λ_{em} = 633 nm). **(a–c)** Merged fluorescence images are shown in (**c, f, i** and **l**) (scale bar corresponds to 10 μm). Figure is reproduced from reference [103].[103]

The other way is to attach fluorescence label to the gold core,[135] but the short distance between the fluorescent label and the gold core could lead to energy transfer and may inhibit or reduce photon emission. It has also been demonstrated that a ligand can be removed during or after cell uptake, either by ligand exchange or by proteolysis.[136]

We have shown that the fluorescence of Au NCs can give a direct visual demonstration of cellular uptake. However, it is challenging to access the nanoclusters quantity that been absorbed.

1.3.2.2 Transmission electron microscopy

Previously, TEM was used only for detecting electron-dense particles *e.g.* metallic nanoparticles rather than soft matter with low electron density. However, advanced TEM approaches such as cryo-microscopy emerged in recent years enabling TEM visualization of both 'hard' and 'soft' particles.[133] Furthermore, very high resolution (0.1 nm, size of atom) aberration-corrected TEM instruments have been developed to image detailed atomic structures of nanoparticles.[137]

Nowadays, TEM is a widely-used microscopy technique for the intracellular detection of metal nanoparticles; their high electron density enables direct visualization. In conventional TEM (in contrast to HRTEM), nanoparticles larger than 5 nm can easily be imaged inside cells,[138] and imaging of single nanoparticles in cellular compartments and organelles is possible. Nevertheless, it requires time-consuming sample processing, such as cell fixation and resin embedding and hence lacks important statistical information.

A detailed TEM study of cellular uptake and intracellular distributions of a 16 nm PEG modified gold nanoparticles by human fibroblast cells (HeLa cells) was presented by Nativo *et al.*[139] They demonstrated that the endosomal route of cellular uptake can be

bypassed to a significant extent by controlling the uptake mechanism either via the delivery of the nanoparticles by liposomes or by surface modification of the nanoparticles with so called cell penetrating peptides (CPPs). Successful nuclear targeting is confirmed using surface modification with a mixture of CPPs and a peptide acting as nuclear localization signal (NLS).

As shown in Figure 1.10, PEG-modified Au NPs are taken up by cells in the presence of liposomes by different routes, and are localized in vesicular intermediate, endosomes, and cytosols. Interestingly, the transfer process of Au NPs from plasma membrane to endosome, and from endosome to cytosol can be observed in TEM images.

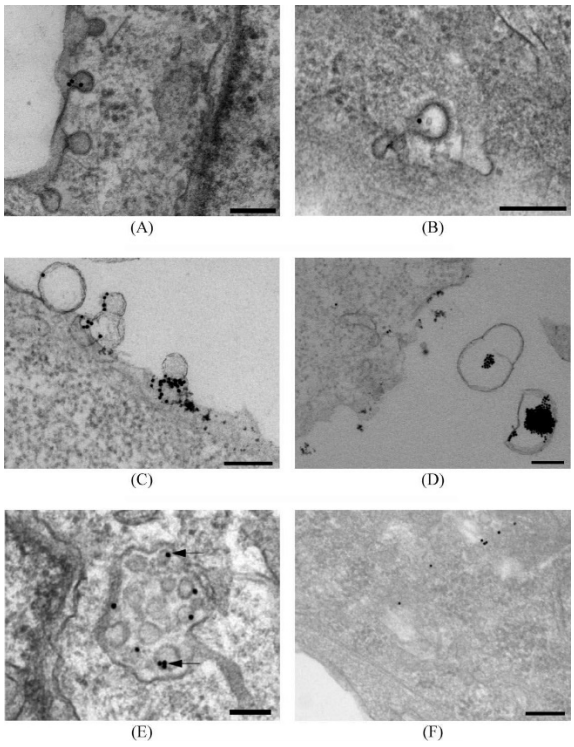

Figure 1.10 Uptake of PEG-modified gold nanoparticles in the presence of liposomes. Observed uptake mechanisms without apparent direct involvement of the liposomes include **(a)** caveolae and **(b)** clathrin-mediated endocytosis. Particle delivery by liposomes and subsequent uptake are shown in **(c)** and **(d)**. Perhaps reflecting the wealth of different uptake mechanisms available under these conditions, nanoparticles are found in the endosome **(e)** or free in the cytosol **(f).** Note that some nanoparticles in the endosome are surrounded by an additional membrane (arrows), which indicates that they have been taken up by the endosome from the cytosol. Scale bars are 200 nm.[139]

1.3.2.3 Inductively coupled plasma – Mass spectrometry (ICP – MS)

Inductively coupled plasma – Mass spectrometry (ICP-MS) is used to qualitatively assess cellular uptake of nanoparticles. ICP-MS is a mass spectrometric method which uses a hot plasma ion source with a temperature up to 8000 °C. Most elements of the periodic table are highly ionized. Biomolecule samples will be fully decomposed and atomized.[140] It has excellent limits of detection (18 parts per trillion for gold) and can be applied to quantify the cellular uptake by digesting the cells with strong acid.[141] While ICP-MS is an excellent tool for quantitative analysis, it is destructive, and cannot differentiate between nanoparticles absorbed on the surface of the cell and those internalized into cells. Treatment of cells with heparin sulfate before analyzing the cells can be used to desorb surface-absorbed nanoparticles, assuming that heparin sulfate polymer has a higher binding affinity to the cellular surface to displace surface-bound gold nanoparticles.[142] Another approach is to selectively etch the gold nanoparticles on the surface of the cells, as was demonstrated by Cho,[143] using solution of I_2 and KI. ICP-MS analysis combined with I_2/KI etching was used to quantify the number of gold nanoparticles both 'on' and 'in' the cells.

Kim *et al.* used ICP-MS to quantify the intracellular nanoparticles, AuNP-NH_2 and AuNP-NH_2-cucurbit [7] uril (CB[7]). The analysis of the result showed that the total amount of the nanoparticles taken up by the cells was nearly identical (Figure 1.11). Quantification of the amount of gold present in cells was also probed. Samples were analysed by ICP-MS to determine the amount of gold in breast cancer cell after 3 h

incubation with 0.5 μM of AuNP-NH_2 and AuNP-NH_2-CB[7]. Cellular uptake experiments with each gold nanoparticle were repeated 3 times, and each replicate was measured 5 times by ICP-MS. Error bars represent the standard deviations of these measurements.[144]

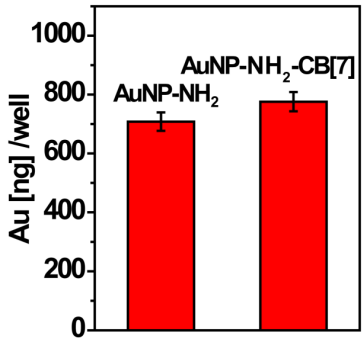

Figure 1.11 Cellular uptake of the gold nanoparticles.[144]

The bioscience community is working on development of standard imaging approach to accomplish all measurements for nano-bio interaction.[146] Nowadays, combined ways were used to analyze the cellular uptake. The number of citrate-coated gold nanoparticles in vesicles after absorption in mammalian cells has been assessed by TEM.[147] In this study, TEM results have been further validated by inductively coupled plasma atomic emission spectroscopy (ICP-AES). This technique allows the quantification of the number of gold atoms, thereby offering a more precise assessment of the number of gold spheres, still similar to TEM estimation. As for ICP-AES, inductively coupled plasma mass spectrometry (ICP-MS) provides an elemental analysis and helps estimate the number of nanoparticles in the sample.

1.4 Development of Au NCs for biomedical applications

1.4.1 Folic acid as targeting ligand

Folic acid (Figure1.12) is a natural B-vitamin that has become a useful ligand for targeted cancer therapies, It binds to a tumor-associated antigen known as the folate receptor (FR, $k_d = 10^{-9}$).

Folate that is naturally found in most vegetables plays an important role in various cellular reactions including the bio-synthesis of purines and pyrimidines and other methylation reactions involving DNA, proteins, and lipids.[148]

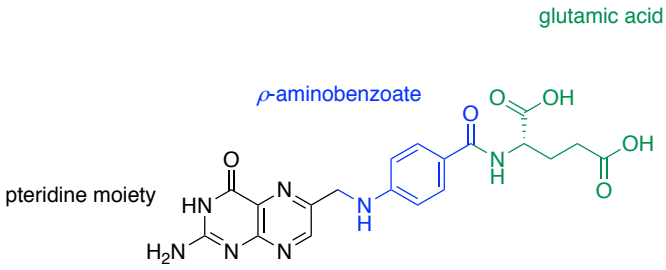

Figure 1.12 The structure of the Folic acid.

Folate leakage could lead to DNA hyper-methylation and gene expression, and also to chromosome damage, both key factors for carcinogenesis.[149] In other words, when cancer is established, there is increasing evidence that folate can enhance its progression in some carcinomas (colon and rectum, breast and prostate).[150]

Folate receptors are a group of highly heterogeneous proteins, which mediate accumulation of folate into cells and regulate folate homeostasis and cellular

proliferation.[151-152] There are two main ways for cells to collect folate. One way is via the reduced folate carrier (RFC), a bidirectional transporter with low affinity for folate and classical anti-folates, but very high capacity for transport. RFC is ubiquitously expressed.[153] The other way is via the folate receptor (FR), glycosyl-phosphatidylinositol (GPI)-anchored cell surface glycoprotein of 38-40 kDa, preferentially linked to oxidized folate.[154] It enhances folate through endocytosis, showing very high affinity but low capacity. Since the macromolecule remains intact in the endosome, it can fully exert its function inside the cell.[155] After endocytosis, FR is recycled, returning to the cell surface to bind to new folate (Figure 1.13). The recycling rate of FR α is reported in the range from 5.7 h to 20 h.[156] Longer exposure times were chosen to maximize the internalization of NPs by cells.

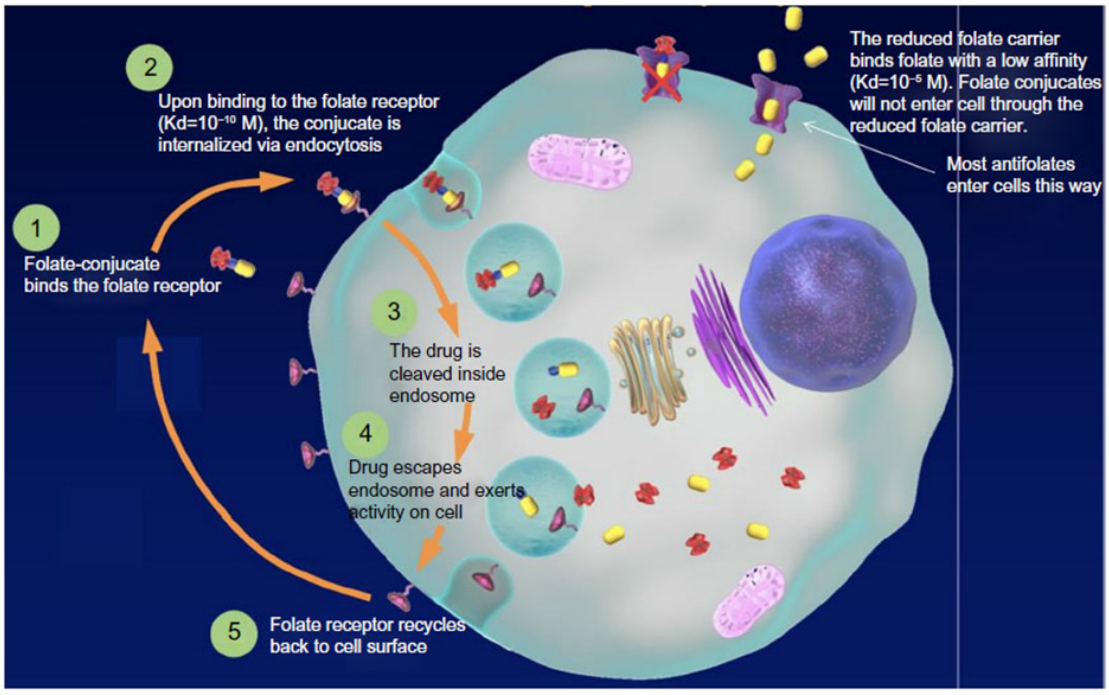

Figure 1.13 The two folate receptors, reduced folate carrier (RFC), and Folate Receptor alpha. Scheme of mechanism of vintafolide.[157]

There are three isoforms of folate receptors: Alpha (FRα), Beta (FRβ), Gamma (FRγ). FRA is the most widely researched.[151] It has a very limited tissue distribution. In normal tissue, FRA is mainly expressed on the apical surface of a subset of polarized epithelia cells including parotid, kidney, lung, thyroid and breast [158] which is far away from the blood stream.[159] While FRA overexpression is described in carcinomas of the ovary and endometrium, non-small cell lung adenocarcinoma, clear cell renal carcinoma, colorectal carcinoma, and breast carcinoma.[151] The limited tissue distribution of FRA and its specific expression on certain malignancies make its and attractive target for directed therapies. FRB is mostly found in the spleen, placenta, and white blood cells and has different stereo-specificities and affinities for folate

coenzymes and anti-folates.[160] FRG is found principally in bone marrow.[161]

He *et al.*[162] synthesized a core-shell-corona particles which are FA-modified PEG-poly(lactic-co-glycolic acid) (PLGA) amphilic copolymers that encapsulated cisplatin (CDDP) and paclitaxel (PTX). Excellent compatibility of the FA-capped NPs was demonstrated by the absence of endogenous, exogenous or conventional coagulation pathways as well as activation the complement system. Two cell lines were used to test the drug's effects, A549 (FR-negative) and M109 (FR-positive). Even both were strongly inhibited under the combined drugs, the M109 exhibited better anticancer effects than A549.

Lei *et al.*[163] did research on turn-on fluorescent nano-probe (FA-PEI-carbon dots) for FR-positive cancer cells *in vivo* and *in vitro*. These fluorescent nano-probes' ability to recognize FR-positive cancer cells was confirmed with confocal fluorescence microscopy images by comparing compound's cellular uptake of FR positive cells HeLa, HepG2 and FR-negative cell line MCF-7.

Chen *et al.*[164] resolved the crystal structural basis for molecular recognition of folic acid by folate receptors at 2.8 Å resolution. As shown in the Figure 1.14, FR α has a globular structure stabilized by eight disulphide bonds and contains a deep open folate binding pocket comprised of resides that are conserved in all receptor subtypes.

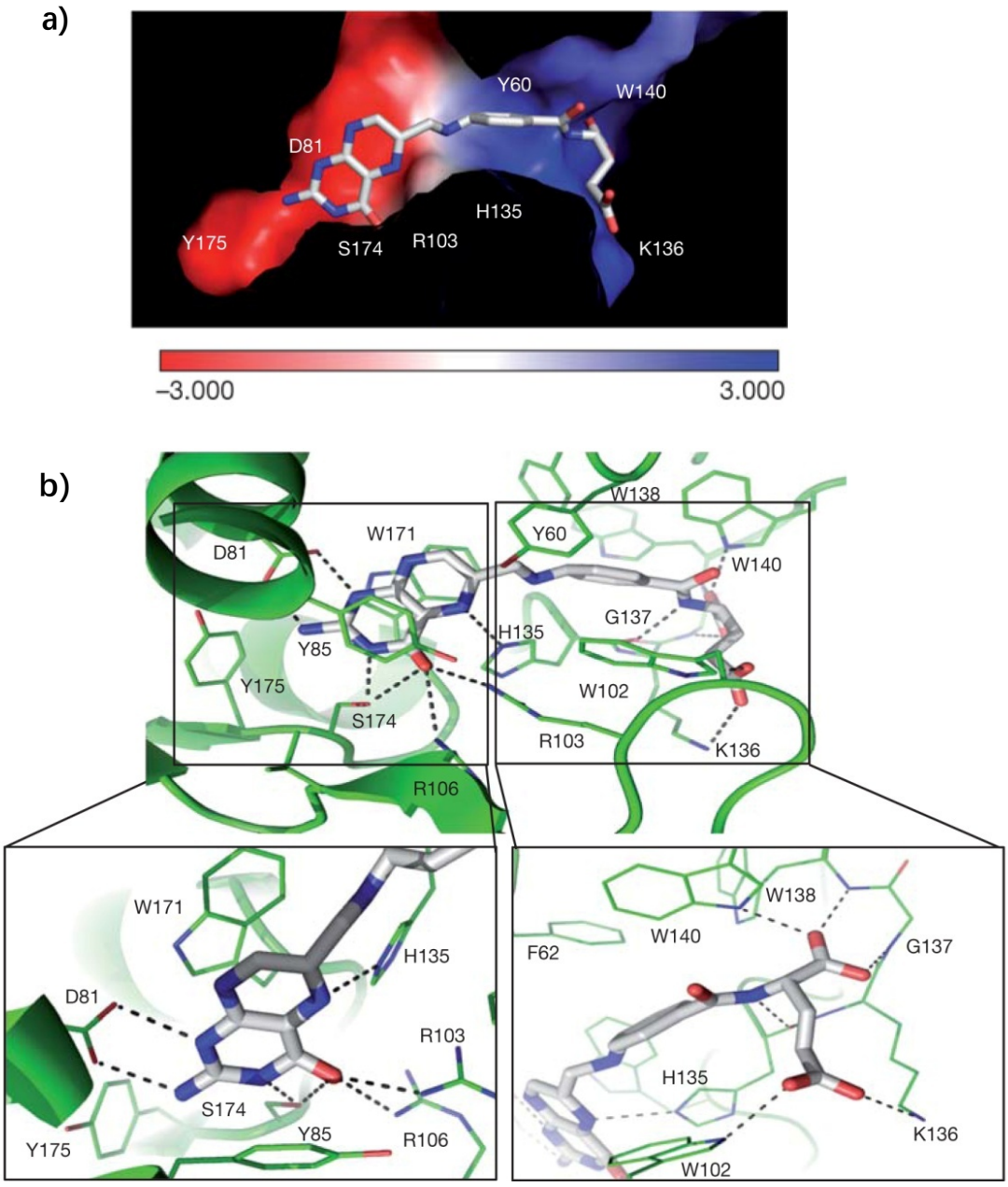

Figure 1.14 Structural and biochemical analysis of FRα -folic acid interactions **a)** The internal charge distribution surface of the binding pocket A colour-code bar (bottom) shows an electrostatic scale from −3 to +3 eV. **b)** Folic acid-binding network with close-ups of the folic acid head and tail groups. Residues that line with the biding pocket are shown in green and folic acid is shown in grey. Hydrogen bonds are indicated by dashed lines.[164]

Structural and mutational analyses provided rationale for the absolute requirement of the *pterin* group for anchoring folate in the binding pocket of the receptor and for the availability of the glutamate group for conjugation with drugs and imaging reagents, without adversely affecting the interaction between receptor and ligand.[164] The key part of folic acid conjugated with folate receptor was the pterin group. For modification of folic acid on the glutamate part either α– or γ– carboxylic acid groups can be activated. However, the recognition by the folate receptor is not expected to be affected.

1.4.2 Magnetic resonance imaging

Magnetic resonance imaging (MRI) is a diagnostic tool for medical imaging and it provides excellent soft tissues contrast resolution, sensitive to temperature changes. [165] According to different relaxation pathways, MRI images can be classified as T_1 (longitudinal relaxation time) or T_2 (transverse relaxation time)-weighted images. MRI contrast agents can help to resolve images and allow better interpretation.[166] Commonly, paramagnetic complexes, such as Gd-DTPA (gadolinium diethylene triamine pentaacetic acid), are used as T_1 contrast agents and magnetic nanoparticles are selected as T_2 contrast agents.

The mechanism of T_2 contrast is as follows: Under an applied magnetic field (B_0), a magnetic dipole moment is induced in superparamagnetic nanoparticles. When water molecules diffuse into the periphery (outer sphere) of the induced dipole moments, the magnetic relaxation process of the hydrogen atoms in water are perturbed and the spin-

spin relaxation time (T_2) is shortened. Such changes result in darkening of the corresponding area in T_2 -weighted MR images (Figure 1.15). The degree of the T_2 contrast effect is typically represented by the spin – spin R_2 relaxivity ($R_2 = 1/T_2$), where higher values of R_2 result in a greater contrast effect. The relaxivity coefficient R_2, which is obtained as the gradient of the plot of R_2 versus the molarity of magnetic atoms, is a standardized contrast enhancement indicator.

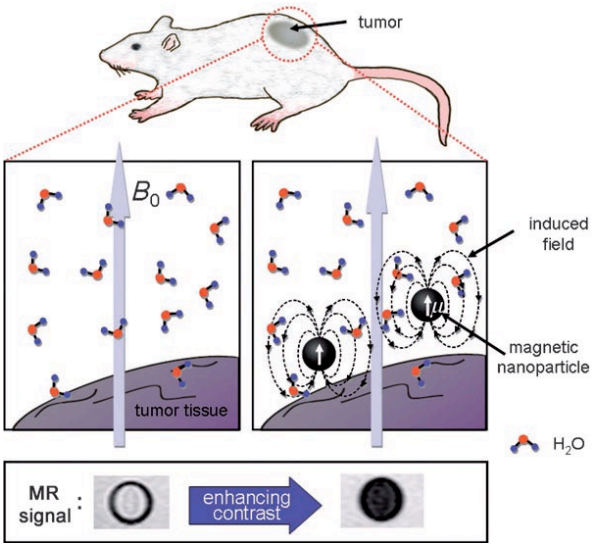

Figure 1.15 Scheme of magnetic resonance contrast induced by magnetic nanoparticles. Under and external field (*B0*), magnetic NPs are magnetized with a magnetic moment of *m* and generate an induced magnetic field, which perturbs the nuclear spin relaxation processes of the hydrogen atoms. This perturbation leads to MR contrast enhancement which appears as a darkening of the corresponding section of the image. [167]

In a previous study, iron oxide magnetic NPs (MNPs) were shown to provide a strong contrast in T_2-weighted images.[168] Metal alloy MNPs such as FeCo and FePt can also

serve as MRI contrast agents.[167] A significant challenge associated with the application of these NPs *in vivo* is nonspecific uptake by the reticuloendothelial system (RES),[169] including the liver, spleen, and lymph nodes.[169-170] Hence there is a need for the next generation of NP-based MRI contrast agents, which incorporate novel nano-crystalline cores, stable coating materials, and functional ligands to improve specific delivery/ targeting.[171] Au NPs with diameter of 2 - 2.5 nm capped by dithiolated ligand (DTDTPA) was conjugated with gadolinium chelates. The conjugates were proved be an attractive MRI contrasts.[172]

1.4.3 Thermal therapy

Temperature is one of the most important parameters in determining the dynamics and viability of biological systems.[173, 174] In humans, any temperature increase significantly above the normal body temperature (~ 37 °C) is indicative of disease and can lead to irreversible damage and even to fatal organ failure.[175] Nevertheless, contrary to general thinking, controlled temperature increments could have positive effects in patients with an ongoing disease.[176] The beneficial effects of thermal therapy in the treatment of cancer were first observed in the 19th century.[177] It was shown that the administration of living bacteria to cancer patients could cause a partial tumor regression,[178] and successful treatment of uterine cervix cancer can be achieved with circulating heated water treatment.[178] However, the heating methods and temperature measuring technologies were not sufficiently advanced at that time, so the success and reproducibility of such treatments were reduced. Consequently, the clinical application

of these therapies was not accomplished.

In recent years, several scientific reports demonstrated substantial improvements in cancer treatment outcomes by using thermal treatments.[179] A significant effort has been made to develop novel techniques for controlled and localized heating to understand the mechanisms of temperature induced cell death.[180] It is widely assumed that the efficacy of a thermal treatment is given by two main factors: the magnitude of the temperature increment and the duration of the treatment.[181, 182] To achieve efficient treatment, it is necessary to induce a well-localized heating, so that a significant temperature increase is achieved in the tumors only area.[183]

For the purpose of cancer treatment, hyperthermia (HT) is currently attracting much attention from the scientific community.[178,184] Compared to traditional techniques such as surgery, chemotherapy and radiation therapy, the HT therapies are potentially more specific and less invasive.

Nanotechnology is currently proposed as a promising technique for remotely induced and localized heating. This application relies on the development and bio-incorporation of heating nanoparticles (HNPs).[185-186] which have long circulation times in the bold-stream, are targeted and able to produce localized heating in response to external trigger.

1.4.3.1 Nanoparticles for magneto-thermal therapy

Currently, promising results were achieved with HNPs in which heating is induced by

the application of oscillating magnetic fields (magnetic heating nanoparticles, M-HNPs).[165] Since MR imaging is sensitive to temperature, the image-guided thermal therapy is developed and uses real-time temperature mapping to provide better treatment outcome. The HNPs thermal dose required to induce cell death ranges from 25 to 240 minutes at 43 °C.[187]

Therefore, the role of MRI is to visualize and quantify the deposition of heat energy in the treated and surrounding tissue with adequate spatial and temporal resolution. Consequently, the success of MR image-guided thermal therapy depends on the accuracy with which temperature can be estimated. Quesson *et al.*[188] summarized the thermometry methods: the NPs are introduced into the tumour site and activated by oscillating magnetic field to generate heat.[189,190] The proof of concept of HT treatments based on M-HNPs was provided in 1957 by Gilchrist *et al.* who demonstrated tissue heating by a 1.2 MHz magnetic field based on the presence of Fe_2O_3 magnetic nanoparticles.[191] In 2001, Jordan *et al.* reported the first clinical study of magnetic hyperthermia,[192] demonstrating successful and safe treatment of brain tumors by aminosilane-coated superparamagnetic iron oxide nanoparticles. M-HNPs are currently considered as a multi-functional platform for cancer therapy, since they can be used for simultaneous tumor heating and imaging.[190]

1.4.3.2 Nanoparticles for photo-thermal therapies

An alternative route for activation of NP is provided by illumination with laser radiation that has attracted much attention for the last few years.[193]

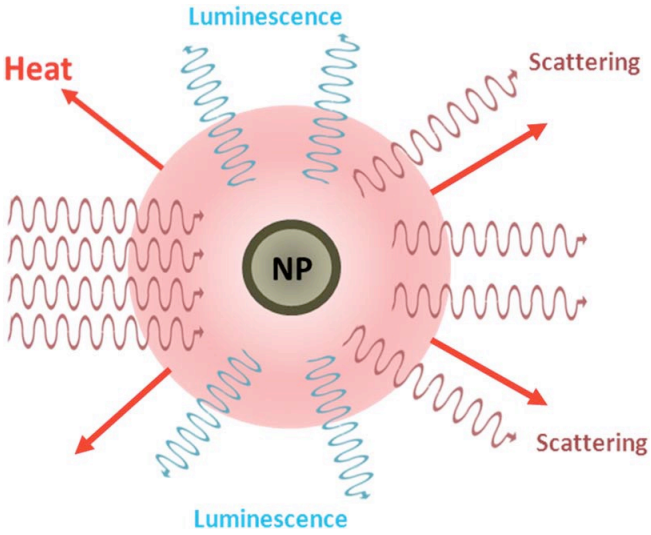

Figure 1.16 Schematic representation of the different processes activated when a light beam interacts with a nanoparticle. The presence of scattering, luminescence and heat generation are included.[182]

When a nanoparticle is illuminated by a light beam, some of the incident photons are scattered by the nanoparticle while others are absorbed. The absorbed energy is released as heat or as luminescence (Figure 1.16).[182]

Further reduction of non-desired light absorption by healthy tissues can be achieved by using specific laser wavelengths lying in the so-called biological windows.[194,195] Biological windows are defined as the spectral ranges where tissues become partially transparent due to simultaneous reduction in both absorption and scattering. [182]

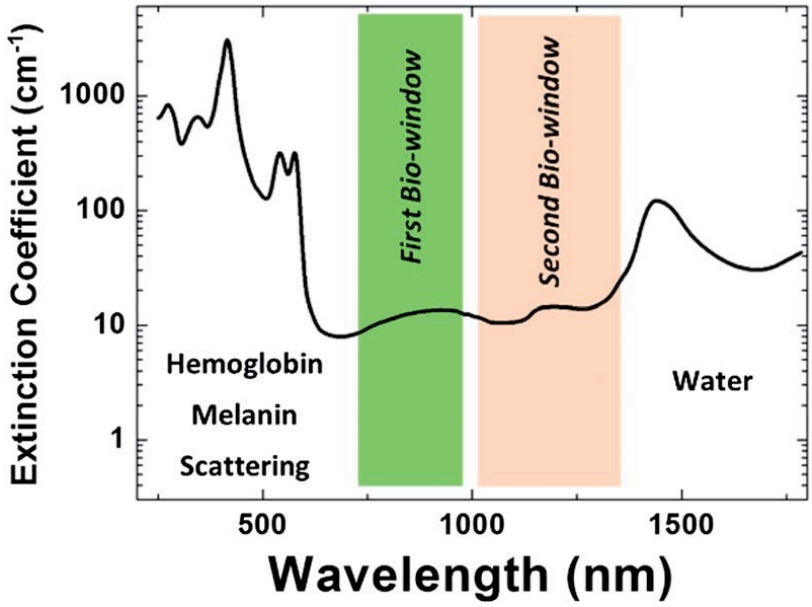

Figure 1.17 Extinction coefficient of a representative tissue.[182]

To achieve nanoparticle-based selective and efficient photo-thermal therapies, the NPs to be used must fulfil a number of requirements:

i. Large absorption cross section for optical wavelengths within any of the two biological windows. This would ensure an efficient absorption of optical radiation and, in combination with a large light-to-heat conversion efficiency, would make thermal therapy possible with low-power laser sources.[196]

ii. Low toxicity. Toxicity of L-HNPs should only be activated in the presence of optical radiation. L-HNPs should be non-toxic to both healthy and cancer cells. This is required to achieve a selective treatment with minimum side effects.[197]

iii. Surface functionalization. This would also allow for highly selective treatments since tumor targeting would become possible.[198]

iv. Good solubility in biologically relevant solvents. This would ensure long circulation times (half-lives) in the bloodstream and, consequently, easy access to cancer tumours even at low circulation flows.[199]

Based on these criteria, gold nanostructures such as nanocages, nanostars, nanoshells and nanorods have been investigated. Among them gold nanorods (NRs) are the most widely researched photo thermal therapy (PTT) agents since nanorods have a short and long axis, hence two absorption peaks matching with the transverse and longitudinal SPR. Recently, Zhang *et.al.*[200] prepared Au NRs with a 40 nm length, 10 nm diameter and corresponding transverse and longitudinal absorption peaks of 520 nm and 900 nm. A successful targeted damage of HER2-positive breast cancers has been demonstrated with NIR laser excitation. Better efficacy was obtained compared to traditional therapy.[200]

The effect of NP size and shape on their distribution in solid tumours has been studied. Perrault *et al.* proved that larger size Au NPs were not able to penetrate deep into tumors.

Though PTT was shown to have potentials in cancer treatment, effective heating of some tissues was prevented by various physical and technical limitations. For example, for magnetic hyperthermia, the generators with field amplitudes up to a few ten of kAm^{-1} are needed in the frequency range of 50 KHz to 1 MHz,[190] which presents various technical challenges.[201] Lasers are limited to treatment of superficial tumors as the energy source of PTT, as well as increased non-specific damage to adjacent

tissues.

Inductive heating can be introduced to PTT process: combined with alternating magnetic field, a flow of current is generated within MNPs, the amount of current is proportional to the value of magnetic field and the size of the objects. Hence, the temperature will be improved with increasing resistance.

Zeev *et al.*[202] utilized a dual method of heating which combined laser irradiation with low frequency and amplitude alternating magnetic field to produce magnetic NPs oscillation. This leads to more rapid and efficient cell death, demonstrating that this manipulated MNP(Fe_3O_4) technique can be a superior agent for PTT. This technique can be specifically used on target cells or other live tissues, providing a concentrated assembly for improved cell death capability.

Au NPs are able to convert electromagnetic radiation into heat due to electron excitation and relaxation, providing their potential for thermal ablation of tumor cells.[203] Mendes *et al.* produced Au NPs with diameter of 14 nm and demonstrated an efficient light-to-heat conversion at 530 nm. A ΔT = 12 °C was obtained of cell with Au NPs than without under 60 s 3.44 $W \cdot cm^{-2}$ laser irradiation. Besides, PTT in the visible can reduced breast cancer cell viability by 60 %.[204]

In this chapter, we have introduced the synthesis, properties and applications of gold nanoclusters. Its outstanding optical, magnetic, easy-modification, low toxicity properties make Au NCs as a worthy candidate for cancer treatment.

1.5 Thesis outline

This thesis is composed of seven charters which describe different aspects of the research.

Chapter 2 sets the aims for this project.

Chapter 3 introduces the analytical techniques used, including their principles, models and parameters used in measurements. The methodology used for nanocluster synthesis is provided in detail. The description of *in vitro* assays and cellular uptake studies is also included here.

Chapter 4 presents the fabrication of capping ligands, thioctic acid conjugated poly (ethylene glycol). The properties of water-soluble gold nanoclusters as well as the assessment of their stability are discussed.

Chapter 5 describes the development of folic acid targeted ligands, the production of folic acid conjugated gold nanoclusters and the evaluation of their properties and stability.

Chapter 6 shows the *in vitro* studies of both targeted and non-targeted Au NCs. The cytotoxicity of Au NCs is assessed by cell viability assay (MTT assay). The cellular uptake are analyzed by ICP-MS.

Finally, in Chapter 7, all the results and the conclusions of this projects are summarized and future works is suggested.

Chapter 2

Aims and objectives

The aim of this project is to develop novel targeted Au NCs for imaging and treatment based on magnetic water-soluble gold nanoclusters conjugated with folic acid.

Particular objectives are:

1) Develop the methodology for colloidal synthesis of Au NCs starting from gold (III) chloride hydrate, with kinetic and thermodynamic control of growth of monodisperse particles with diameter below 2 nm.

2) Explore various routes for conjugation of folic acid for targeting of FA receptor overexpressing cancer cells.

3) Study optical, morphological and magnetic properties of synthesized NC.

4) Explore biocompatibility, cell uptake and targeting efficiency of Au NCs and FA conjugates.

Chapter 3

Experimental methods

Commercial reagent grade solvents from Fisher Scientific® were used for all reactions. All anhydrous solvents were purchased from Fisher Scientific® or Sigma Aldrich®. All reagents were purchased from Sigma Aldrich® or Fisher Scientific® and used without further purification.

Milli Q water (resistance 18.2 MΩ•cm) was purified with a Barnstead NANOpure DIwater™ system. All glassware used for AuNC synthesis was thoroughly cleaned with *aqua regia* (37 % HCl: 70 % HNO_3=3:1 v/v), rinsed with copious amounts of nanopure water, and then dried in an oven (T = 50 °C) prior to use.

3.1 Optical and morphological characterization

In this project, UV/Vis absorption spectra (190-900 nm) were recorded using a Cary 100 UV/Vis spectrophotometer (Varian, Palo Alto, USA). High resolution transmission electron microscope (HR-TEM) was performed on a JEOL-2100 TEM equipped with a thermally assisted field-emission gun, which was operated at an accelerating voltage of 200 kV. The TEM samples were prepared by drop casting colloidal solution of Au NCs onto a graphene oxide coated copper grid and allowed to dry. Dynamic light scattering data were obtained from Nano-ZS instruments (Malvern Zetasizer, UK). Inductively coupled plasma mass spectrometry (ICP-MS), using a

Thermo-Fisher Scientific X-series II with a hexapole collision cell charged with 7 % hydrogen in helium. Data were recorded and analysed using PlasmaLab software 2.5.4, (Thermo-Fisher Scientific). The details of each characterization method is introduced in the following chapter.

3.1.1 UV-Vis spectroscopy

UV/Vis spectroscopy is an absorption technique used to record intensity of absorbed light in the wavelength range from ultra-violet to near-infrared (200 – 900 nm). As shown in Figure 3.1, upon absorption of light, electrons are transferred from the ground state to higher energy excited state. Absorption profile can be measured by UV/Vis spectroscopy, and can be used to estimate the concentration of the sample using Beer-Lamber Law:

$$A = \varepsilon bc = \log\left(\frac{I_0}{I_1}\right), \tag{3.1}$$

where A is the absorbance, ε is the molar attenuation coefficient, b is the path-length, c is the molar concentration, I_0 is the incident light intensity, I is the transmitted light intensity.

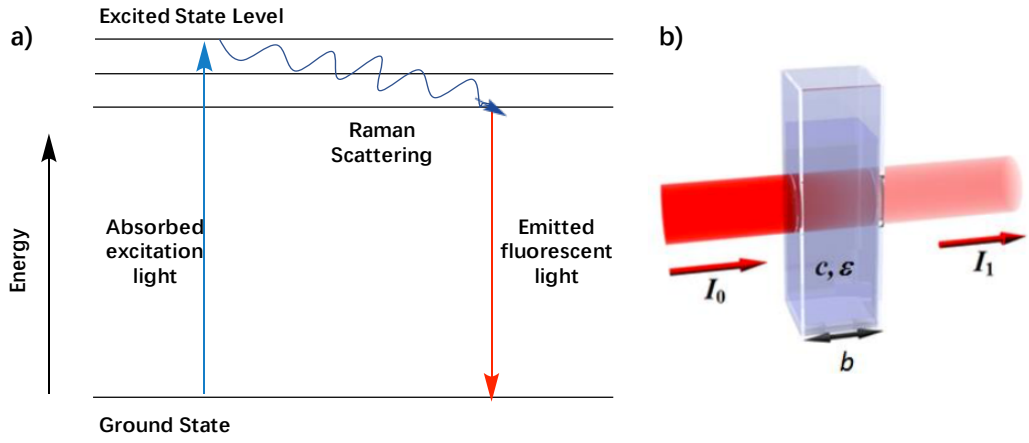

Figure 3.1 a) Jablonski diagram illustrating electron transfer to excited state upon absorption of photon; Raman scattering and fluorescence emission processes are shown in the sketch, **b)** An arrangement of cuvette with liquid sample for absorption measurements.

The main components of a UV/Vis spectrophotometer are illustrated in the Figure 3.2.

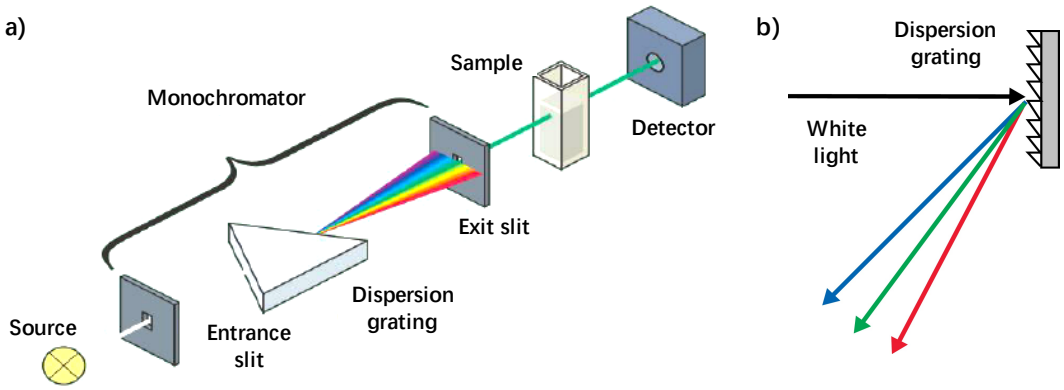

Figure 3.2 a) Sketch of UV/Vis spectroscopy **b)** Morphology and process of homographic gratings.

A white light source is used for excitation. To account for difference in light intensity

at different wavelength, the measurements are performed with a reference sample, i.e. cuvette with solvents. Two white light sources are commonly used in UV-Vis spectrophotometers: the deuterium arc lamp, constant light intensity in the UV region; the tungsten-halogen lamp (good intensity over part of the UV and the visible range). In some spectrometers, both types of lamps are used to generate a single broadband source.

Dispersion gratings are used to select monochromatic light for excitation. An exit slit, positioned after the grating allows selection of specific wavelength of light from a continuous source. Generally, holographic gratings are used in UV-Vis spectrometers. Light falling on the gratings is reflected at different angles, depending on the wavelength. Holographic gratings can generate a linear angular dispersion with wavelength and are temperature intensive. (Figure 3.2 b)

Intensity of light transmitted (not absorbed) through the sample is detected by photomultiplier tube. It combines signal conversion with several stages of amplification within the body of the tube.

Sample holders (Cuvettes) are optically transparent. Glass or plastics cuvette are used in the visible - NIR region. Below 310 nm quartz or silica cuvettes are used.

In this project, UV/Vis absorption spectra (190 - 900 nm) were recorded using a double beam, dual chopper and single dispersion Cary 100 UV/Vis spectrophotometer (Varian, Palo Alto, USA, Figure 3.3). It consists of tungsten-halogen light source with quartz

window, deuterium arc ultraviolet source, Czerny-Turner 0.278 m monochromator and high performance R928 photomultiplier tube.

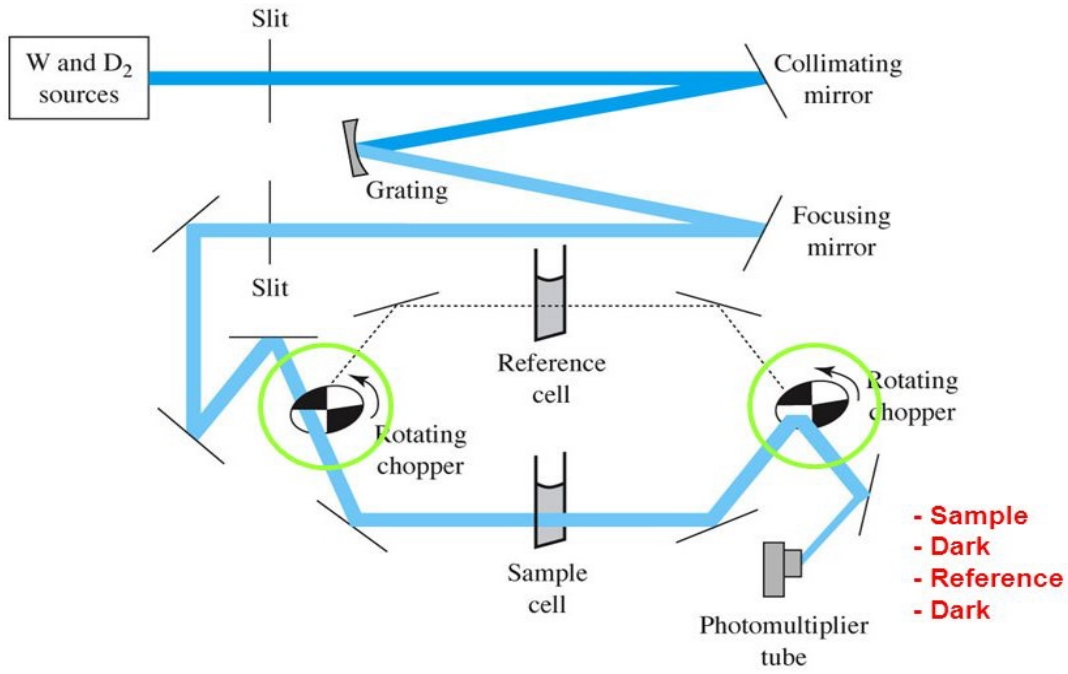

Figure 3.3 Schematic diagram of Varian Cary 100.

Quartz cuvettes (1 mL) or disposable plastic cuvettes (400 μL) was used. Solvent used was analyzed and reference spectrum recorded. Then analyte solution (au concentration around 0.5 mM) was transferred to cuvette and spectrum was recorded starting from 800 nm to 200 nm at a scan rate of 600 nm/min. Light source changes at 350 nm. Absorption spectrum of each sample was recorded 3 times plotted as average.

3.1.2 Transmission electron microscopy

Transmission electron microscopy (TEM) uses high energy electrons beams (accelerating voltage up to 300 kV) to resolve the sample morphology (*e.g.* crystal

structure). The electrons from the beam are scattered by the atoms, and the transmitted electrons are projected to generate images (Figure 3.4).

De Broglie's formula (Equation 3.2) describes the properties of electromagnetic radiation and Abbe's equation (Equation 3.3) links the wavelength of radiation to the resolution limit of a microscope.

$$\lambda = \frac{h}{mv} , \tag{3.2}$$

where *h* is Plank's constant; *m* is mass of the electron, *v* is electron velocity.

$$r = \frac{0.61\lambda}{n \sin a} , \tag{3.3}$$

where *r* is resolution; λ is wavelength; *n* is refractive index of the medium; a denotes half of the angular aperture of the light source.

Larger accelerating voltages provide increased electrons speed and lead to the greater resolution quality of the images.

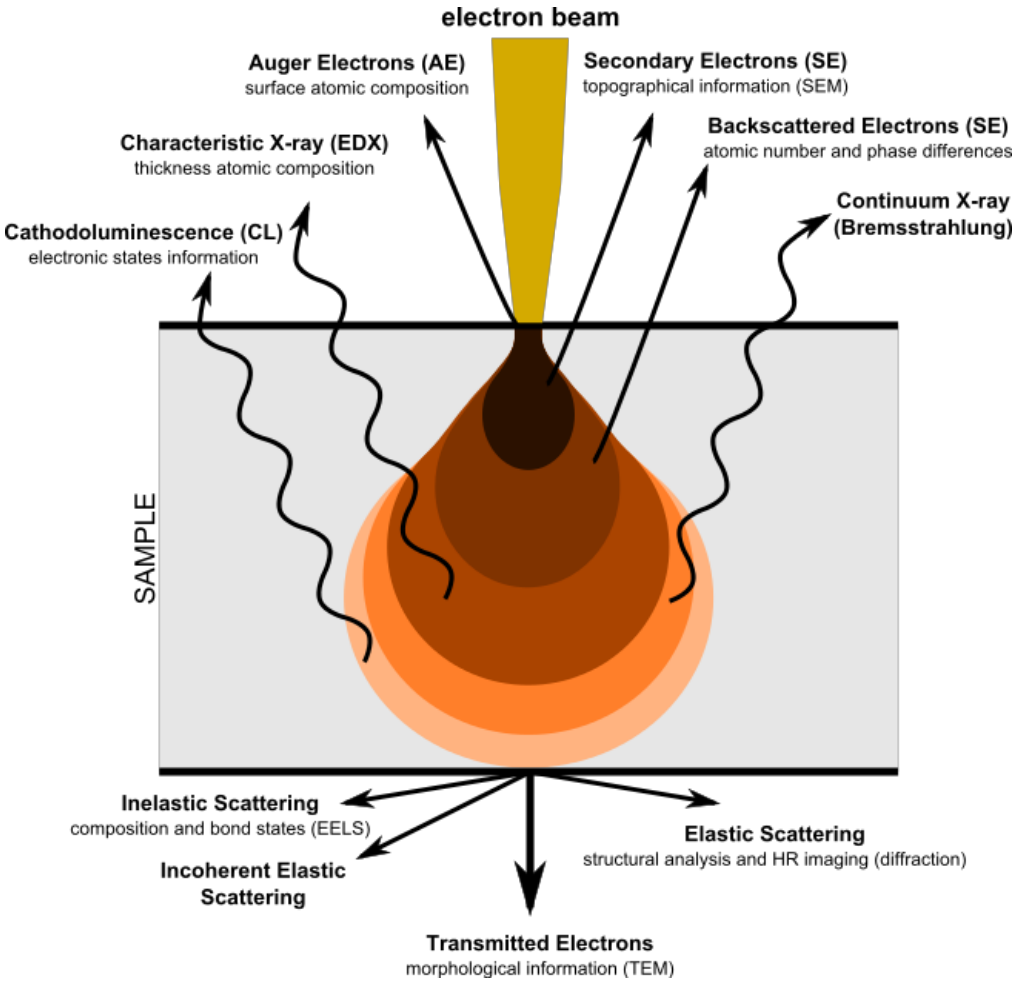

Figure 3.4 Diagram illustrating the interaction between electron beam with samples.[205]

Transmission electrons microspores consist of an electron source, electromagnetic lens, sample holder and imaging system.

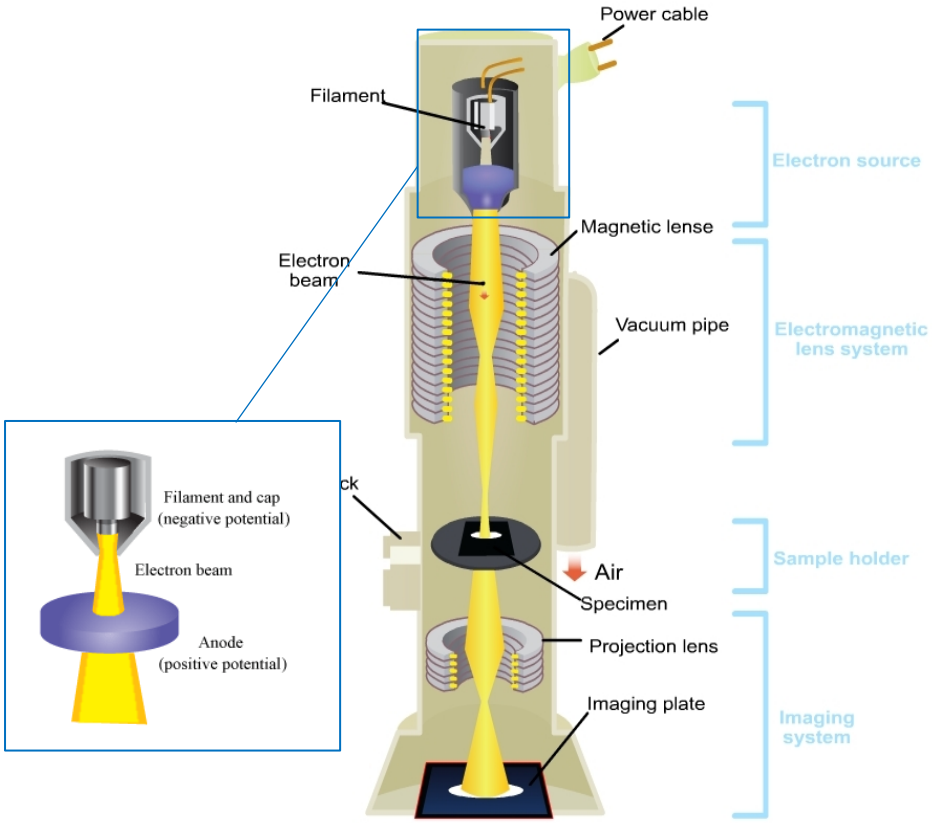

Figure 3.5 Structure of a TEM and (inset) electron source structure (Reproduced from Atomic World established by the Department of Physics, the Chinese University of Hong-Kong).[206]

The electron beam is generated by a device composed of a cathode (tungsten filament) and anode (usually carbon). Electrons are emitted by heating the tungsten filament (cathode) and confined to a loosely focused beam after passing through a negative potential cap (Figure 3.5). The beam is then accelerated towards the sample by the positive anode. The loose electron beam is focused using electromagnetic lens and a metal aperture. Only electrons with a well-defined energy pass through.

The imaging system consists of a screen and two electromagnetic lenses. Electrons are

refocused after passing through the sample by one electromagnetic lens. The image is enlarged and projected onto the phosphorescent screen by another lens to form an image.

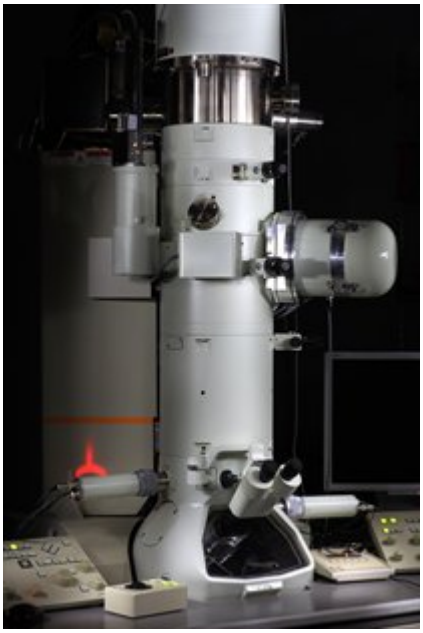

Figure 3.6 Photograph of Jeol-2100F FEG-TEM system.

In this study JEOL-2100F FEG-TEM (Figure 3.6) system was used. It is equipped with a thermally assisted field emission electron gun (FEG), which provides a high brightness and high stability electron source for use at 100 kV and 200 kV; two detectors; bright field STEM detector and high angle annular dark field (HAADF) STEM detector. A point resolution of 0.19 nm can be achieved and allows the ultrahigh resolution imaging of materials.

The Oxford Instruments 80 mm X-Max system was used for energy dispersive x-ray spectroscopy (EDS).

For TEM studies, Au NC solutions (~ 400 µL, 2 mM) were drop-cast onto graphene oxide coated grids and left to dry. The grids were placed onto a probe holder. Images were recorded by Dr. Michael Fay (nmRC).

3.1.3 Dynamic light scattering

Dynamic light scattering (DLS) is used to assess the hydrodynamic size of the nanoparticles. In this technique, a laser beam is used to illuminate the analyte. The intensity of the scattered light is detected by a photon detector positioned at a known scattering angle. The size of the NP is calculated from scattering intensity assuming Brownian motion.

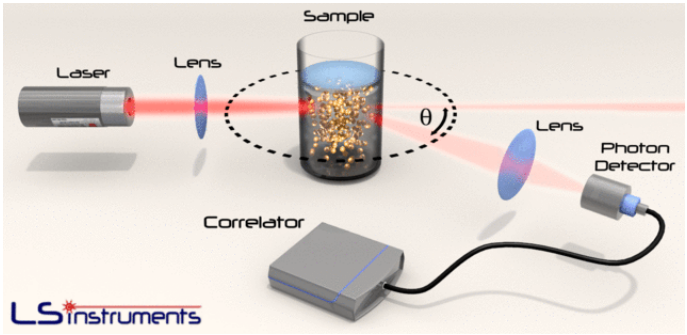

Figure 3.7 Working principle of dynamic light scattering (reproduced from LS instruments website).

Brownian motion of the particles is analyzed using the Stokes-Einstein Equation:

$$D = \frac{k_B T}{6\pi\eta R}, \tag{3.4}$$

where D is the diffusion constant. k_B is the Boltzmann constant, T is the temperature and η is the viscosity and R is the hydrodynamic radius.

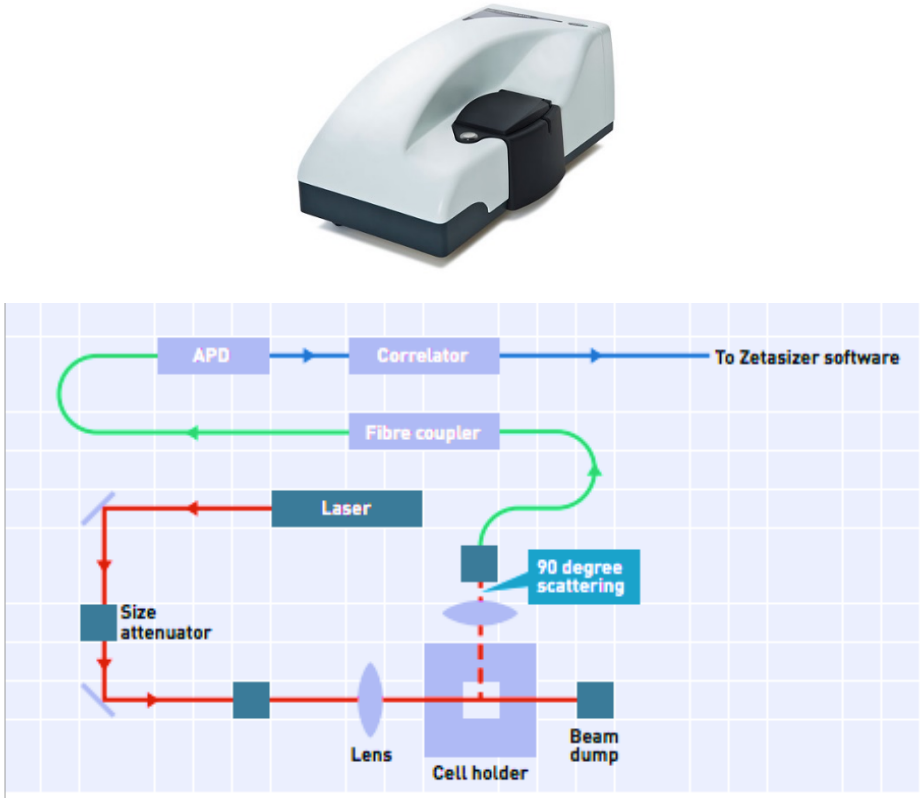

Figure 3.8 Photograph and sketch of Zetasizer Nano ZS (reproduced from Zetasizer website).

The Zetasizer Nano ZS (Malvern, UK) was used for DLS analysis. It is equipped with a Me-Ne laser (4 mW, 633 nm). The signal can be measured between 25 ns to 8000 s, and at measurements angles in the range from 13° to 173°.

For DLS, AuNC solutions were filtered using a 22 μm filter (Sartorius). Each sample was placed into a disposable plastic cuvette (1cm × 1 cm × 3.5 cm) with a volume of 1.2 mL (concentration: ~ 0.1 mM) and was measured and analyzed using Malvern software.

3.1.4 Inductively coupled plasma – mass spectrometry

Inductively coupled plasma – mass spectrometry (ICP-MS) is composed of two main parts: inductively coupled plasma torch and mass spectrometry.

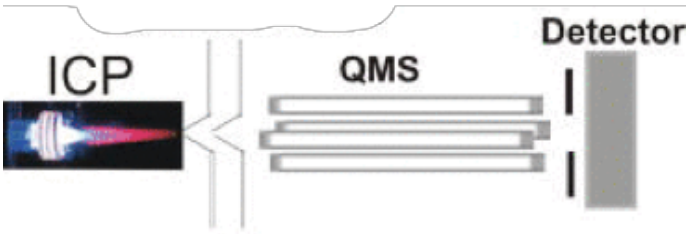

Figure 3.9 Scheme structure of ICP-MS (QMS: quadrupole mass spectroscopy).

The sample is nebulized and converted into plasma, which is then analyzed by the quadrupole mass spectroscopy. The general structure of ICP-MS is shown in Figure 3.9.

The sample introduced into the ICP as liquid form, it goes through different steps. As shown in Figure 3.10a, the first process is nebulization, where the sample is converted to a mist of finely divided droplet called an aerosol. Then in the spray chamber, separation of aerosol occurs as large droplets split to fine droplets that are carried to the plasma.

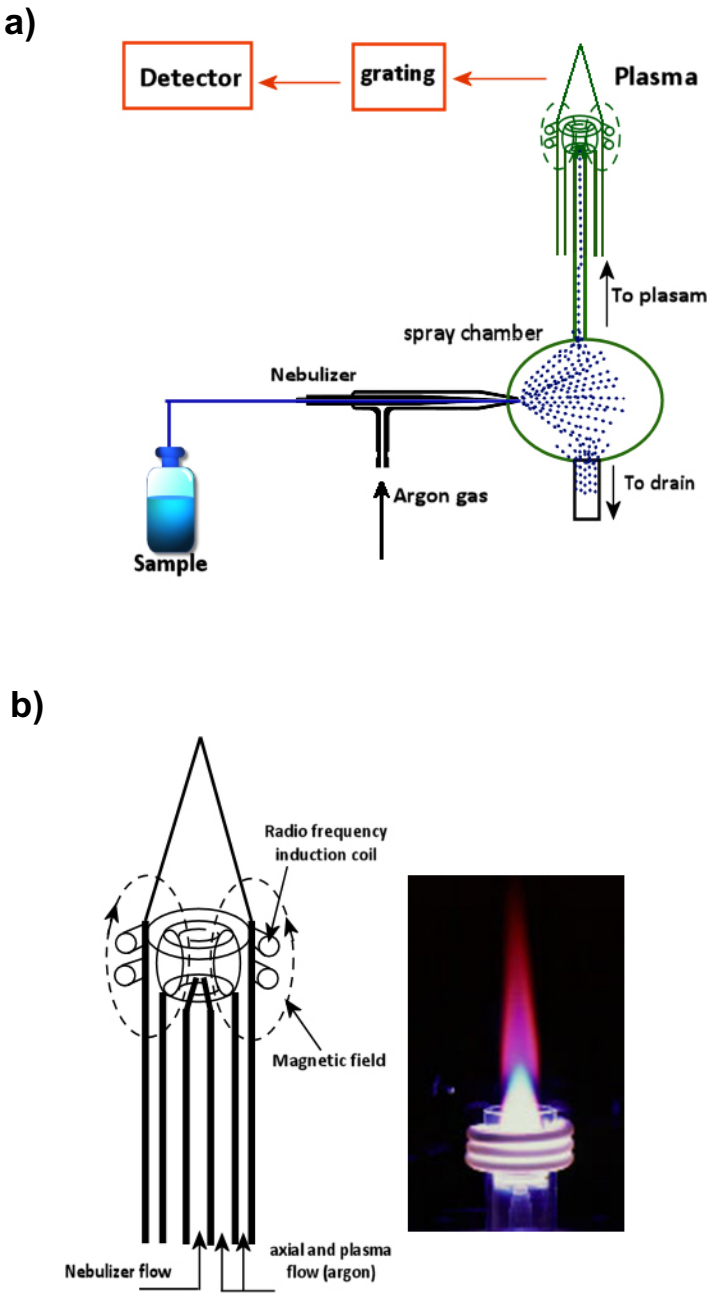

Figure 3.10 a) Configuration and arrangements sketch of ICP-MS; **b)** schematic diagram of typical ICP (reproduction form Labseries).[207]

A typical inductively coupled plasma source is called a torch. It consists of three concentric quartz tubes through which streams of argon gas flow. A water-cooled

induction coil powered by a radio-frequency generator; a Tesla coil to ionize the flowing argon; an induction coil to produce fluctuation magnetic field and interact with previous ions and their associated electrons (Figure 3.10b).

Figure 3.11 Photograph of Thermo Fisher Scientific X-series 2 ICP-MS.

In this project, we used a Thermo-Fisher Scientific X-series ^{II} ICP-MS with a hexapole collision cell charged with 7 % hydrogen in helium. Data were recorded and analyzed using PlasmaLab software 2.5.4 from Thermo-Fisher Scientific.

All samples were prepared at 5 mL volume, and met the following criteria:

(i) Less than 2 % dissolved solids;

(ii) An acid concentration of no more than 2% (v/v) (nitric or hydrochloric);

(iii) Analystes broadly in the correct weight range.

3.1.5 Nuclear magnetic resonance spectroscopy

Nuclear magnetic resonance spectroscopy (NMR) is one of the most powerful tools

available to chemists and biochemists for elucidating the structure of chemical species. NMR is a non-destructive technique that allows determination of the structure of molecule by measuring the interaction of nuclear spins with a static magnetic field and a second oscillating magnetic field. The basis behind is that certain atomic nuclei have the properties of spin and magnetic moment. Exposure to a magnetic field leads to splitting of their energy levels and then generates structural information. As shown in Figure 3.12, an external magnetic field, splits the energy levels (Zeeman splitting) to higher energy for spin state opposite to field direction and lower energy for spin state aligned with B_0. The energy transfer takes place at wavelength that corresponds to radio frequencies. When the spin returns to its ground state level, energy is emitted at the frequency, corresponding to energy level separation.

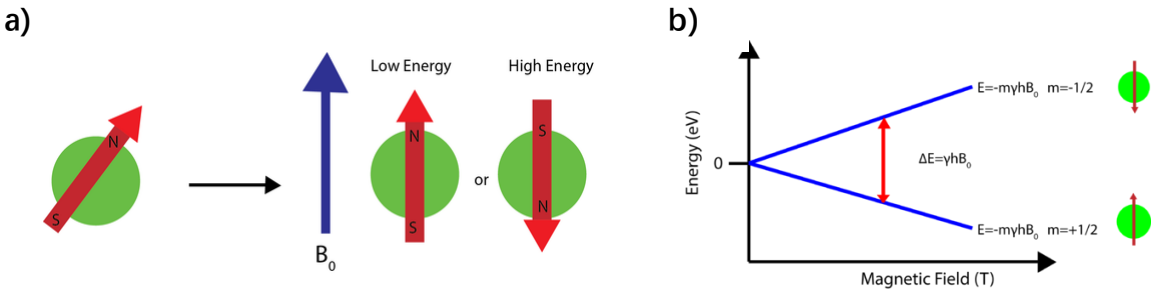

Figure 3.12 Nuclear energy level under external magnetic field.

The precise resonant frequency of the energy transition is affected by electron shielding, which depends on the chemical environment. Reversely, information about the nucleus' chemical environment can be derived from its resonant frequency, also called Larmor frequency. The more electronegative the nucleus is, the higher the

resonance frequency will be. The Larmor frequency can be estimated:

$$\nu = \frac{\gamma B_O}{2\pi}, \tag{3.5}$$

where ν is Larmor frequency, γ is the gyromagnetic ratio, B_0 is the external magnetic field. Also, factors like anisotropy and bond strain affect the frequency values. Tetramethysilane (TMS) is commonly used as proton reference frequency, then chemical shift can be expressed as:

$$\delta = \frac{v - v_o}{v_o} \tag{3.6}$$

where ν is Larmor frequency, v_o is the resonant frequency of TMS, its chemical shift is set to zero on NMR spectra.

NMR also enables assessment of spin-spin coupling, which results in splitting of the signal into two or more lines. The coupling constant (*J*) is measured as an absolute frequency (Hertz) and describes the interaction between a pair of protons. The nature of splitting indicates the number of chemically bond nuclei near the observed nucleus.

Two types of relaxation processes can be observed in NMR: spin-lattice, or (longitudinal) relaxation and spin-spin (transverse) relaxation. Spin-lattice relaxation is observed as first-order decay with characteristic relaxation time, T_1. The value of T_1 depends on gyromagnetic ratio of the absorbing nuclei and on mobility of the lattice.

Spin-spin relaxation is a measure of mutual exchange of spins by two precessing nuclei in close proximity to each other. A nucleus in the lower spin state is excited, and the

other nucleus relaxes to the lower energy state. No net change in the relative spin-state population is observed, but the average lifetime of an excited nucleus is shortened. This process leads to NMR line broadening and is described by a transverse, or spin-spin, relaxation time T_2.

In the NMR studies, chemical shifts are measured, and can be used to estimate spin-spin coupling constant, relaxation time and concentration of the sample. The spectra are acquired in the instrument shown in Figure 3.13, which illustrates a simplified diagram of an NMR. It includes superconducting magnet, sample probe, amplifier, console and computer. The magnet produces the B_0 field necessary for the NMR experiments. The sample probe is equipped with radiofrequency (RF) coil and are used for loading of the sample. RF coils create the B_1 field (perpendicular to the B_0 field) which rotates the net magnetization in a pulse sequence. The console is acting both as a RF transmitter and receiver. The computer is used to set the measurement sequences and to record the data.

For proton NMR measurements, the NMR tubes containing samples is loaded into the probe, the magnet causes the protons to spin and the probe sends RF pulses to excite them and collects the free induction decay as they relax back to equilibrium. The signals are amplified on transmission and receipt. The FIDs are Fourier transformed from time to frequency domains to product NMR spectra of intensity versus chemical sift using computer.

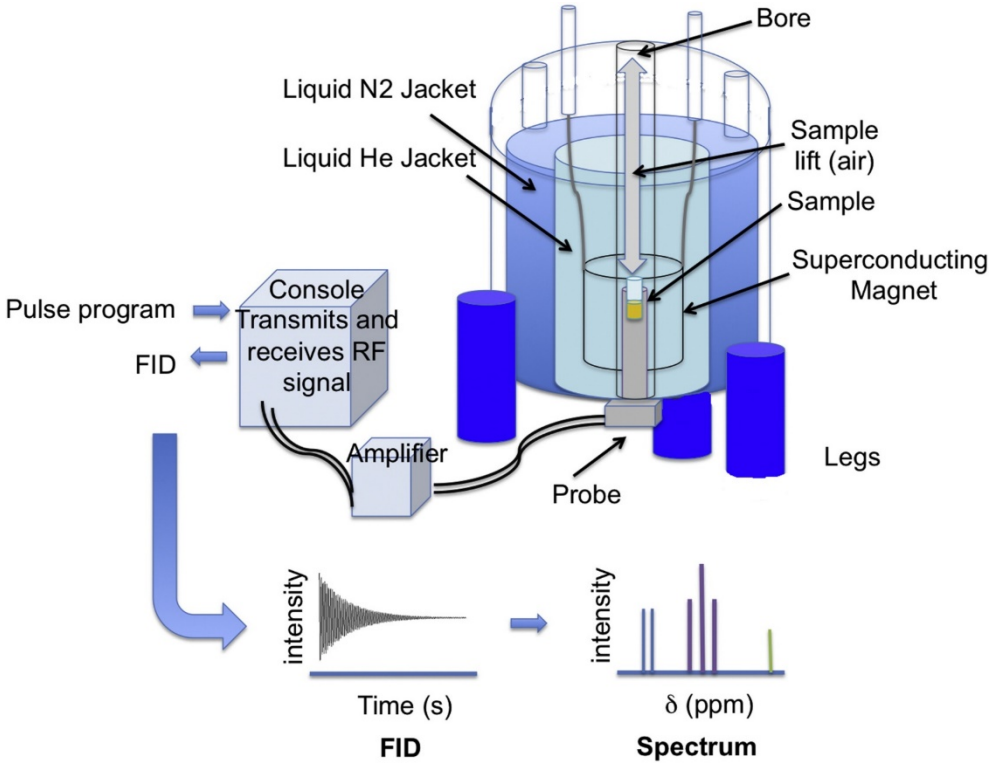

Figure 3.13 Simplified diagram of a Fourier transform NMR spectrometer (the NMR spectra was transferred from free induction decay (FID) signal).[208]

In this project, ^{1}H NMR and ^{13}C NMR spectra were recorded on Bruker™ AV 300, AV400, AV3400, AV3400HD, NMR500 or NMR600 spectrometers at room temperature.

- Bruker DPX300, equipped with a 60 positions auto-sampler, a 5 mm dual $^{1}H/^{13}C$ probe with *z* gradients, automated gradient shimming capability.
- Bruker DPX400, equipped with a 60 positions auto-sampler and a 5 mm autotune broadband probe with *z* gradients, automated gradient shimming capability.
- Bruker AV400, equipped with a 60 position autosampler and a 5 mm autotune broadband probe with *z* gradients, automated gradient shimming capability.

- Bruker AV(III)400, equipped with 60 position autosampler, 5 mm autotune inverse probe with *z* gradients, automated gradient shimming capability.
- Bruker AV(III)500, equipped 60 position autosampler, with a 5 mm dual $^{1}H/^{13}C$ cryoprobe with *z* gradients, automated gradient shimming capability.

To prepare samples for NMR, the solvents were used with no resonances of their own in the spectral region of interest, such as $CDCl_3$, CD_3OD, acetone-d_6, and DMSO-d_6 and D_2O.

Standard 5 mm NMR tubes (507-PP-7-5, Wilmad) were used for holding 10 ~ 20 mg per NMR tube samples dissolved in deuterated solvents (600 μL).

Chemical shifts, δ, given in parts per million (ppm) and *J* values in Hertz (Hz). Multiplets were designated by the following notations: s, singlet; d, doublet; t, triplet; q, quartet; quin quintuplet; sex, sextet; m, multiplet.

3.2 Synthesis of Au NCs

3.2.1 Synthesis of PEG-based ligands

3.2.1.1 Synthesis of TA-PEG550-OCH₃

Thioctic acid conjugated poly-ethylene-glycol (PEG) was synthesized starting from PEG (**1)** (Scheme 3.1). Generally, the hydroxyl group was replaced by a methanesufonyl (**2)** and then displaced with an azide group (**3)** by S_N2 reaction. The amine was formed using an Staudinger reduction reaction. The amine obtained then was coupled with the carboxyl group of thioctic acid (**4)**. Details of each reaction are described below.

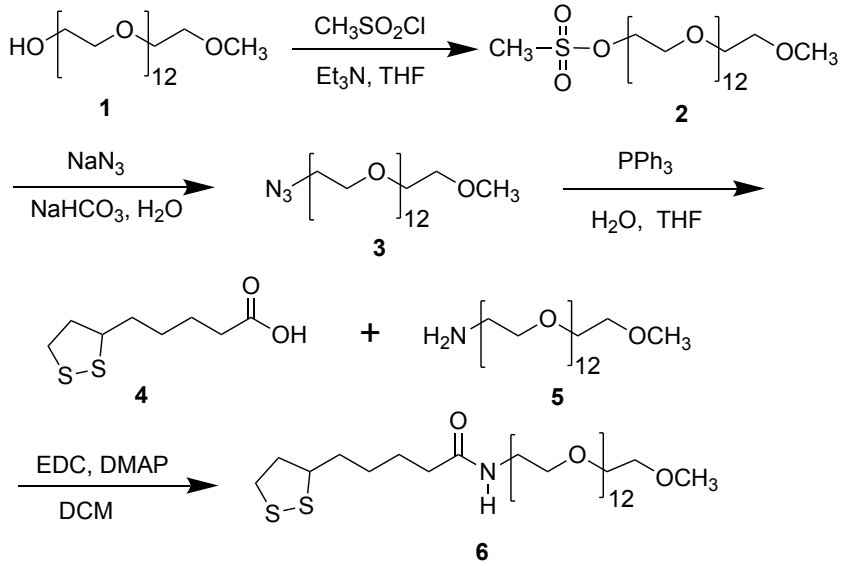

Scheme 3.1 Synthesis of TA-PEG550-OCH_3.

To synthesize N_3-PEG550-OCH_3 **(3)**, PEG methyl ether (MW ~ 550 Da, 4.4 g, 8.0 mmol) and methanesulfonyl chloride (1.2 g, 10.40 mmol) were dissolved in

tetrahydrofuran (THF, 10 mL). The solution was then cooled to 0 °C in an ice bath. Triethylamine (1.62 ml, 12.00 mmol) was added dropwise to the reaction using an dropping funnel and stirred for 48 hrs at room temperature. Excess amounts of solid $NaHCO_3$ was used to adjust the reaction pH to ~ 8, and sodium azide (0.83 g, 12.80 mmol) was added to the solution. The content was heated to 67 °C to distill THF and refluxed overnight at 100 °C. The reaction mixture was cooled to room temperature and then extracted with ethyl acetate (3 × 50 mL : 50 mL per time for 3 times) followed by extraction in chloroform (5 × 50 mL). The combined organic layers were dried over anhydrous sodium sulfate, filtered and the organic solvent removed *in vacuo* at room temperature to yield a waxy liquid. TLC was carried out using a 10:1 (v/v) dichloromethane (DCM): Methanol eluent for the product resulting with an R_f of 0.5. ^{1}H NMR (300 MHz, in $CDCl_3$): δ 3.62-3.71 (m), 3.53-3.57 (m, 2H), 3.39 (t, 2H, J = 5.2 Hz), 3.38 (s, 3H).

N_3-PEG550-OCH_3 was then used to synthesize NH_2-PEG550-OCH_3 **(5)**. N_3-PEG550-OCH_3 (4.18 g, 7.27 mmol) and triphenylphosphine (2.65 g, 10.10 mmol) were dissolved in tetrahydrofuran (48.5 mL) and stirred gently for 1 h. Water (1.2 mL) was added and the solution was further stirred overnight. The THF was removed *in vacuo,* and 48.5 ml of 1 M HCl solution was added into the remaining layers. The reaction mixture was extracted with ethyl acetate (6 × 50 mL). The aqueous layers were basified (to pH ~ 8) with solid $NaHCO_3$ and saturated with solid NaCl. The reaction

mixture was then extracted with DCM (6 × 50mL). The combined organic layer was dried over sodium sulfate anhydrous, filtered and the solvent was removed *in vacuo* to yield a waxy liquid at room temperature. 1H NMR (300 MHz, in $CDCl_3$): δ 3.62-3.71 (m), 3.53-3.57 (m, 2H), 3.51 (t, 2H, J = 5.2 Hz), 3.38 (s, 3H), 2.87 (t, 2H, J = 5.2 Hz).

NH_2-PEG550-OCH_3 (2.0 g, 3.63 mmol), 4-(*N, N*-dimethylamino) pyridine (98 mg, 0.81 mmol), *N*-(3-Dimethylaminopropyl)-*N'*-ethylcarbodiimide hydrochloride (766.8 mg, 4 mmol) were dissolved in DCM (13.5 mL) and cooled to 0 ºC. Thioctic acid (0.825 g, 4 mmol) dissolved in DCM (4.5 mL) was added and the resulting solution was stirred overnight. The solvent was removed *in vacuo* and H_2O (30 mL) was added to the residue. The reaction solution was washed with diethyl ether (4 × 50 mL). The aqueous layer was saturated with excess amounts of solid $NaHCO_3$. The reaction mixture was extracted by DCM (4 × 50 mL). The combined organic layers were dried over anhydrous sodium sulfate, filtered and the solvent was removed *in vacuo*. The crude product was purified by column chromatographed on silica gel using 10: 1 (v/v) DCM: Methanol as eluent to yield a yellow waxy liquid at room temperature (~58% yield). TLC of the product was carried out using a 10: 1 (v/v) DCM: Methanol eluent resulting with an R_f of 0.5. 1H NMR (300 MHz, in $CDCl_3$): δ 6.29 (br s, 1H) 3.62-3.71 (m), 3.53-3.57 (m, 4H), 3.46 (t, 2H, J = 5.2 Hz), 3.38 (br s, 3H), 3.08-3.22 (m, 2H), 2.42-2.52 (m, 1H), 2.19 (t, 2H, J = 7.2 Hz), 1.86-1.96 (m, 1H), 1.59-1.78 (m, 4H), 1.40-1.55 (m, 2H).

3.2.1.2 Synthesis of TA -PEG400-NH₂

As depicted in Scheme 3.2, thioctic acid conjugated PEG teminated with amine was synthesized using a similar method to that of $–OCH_3$ terminated ligands. One additional step was used to displace azide with amine, then to carboxylic acid. Details of this procedure are described below.

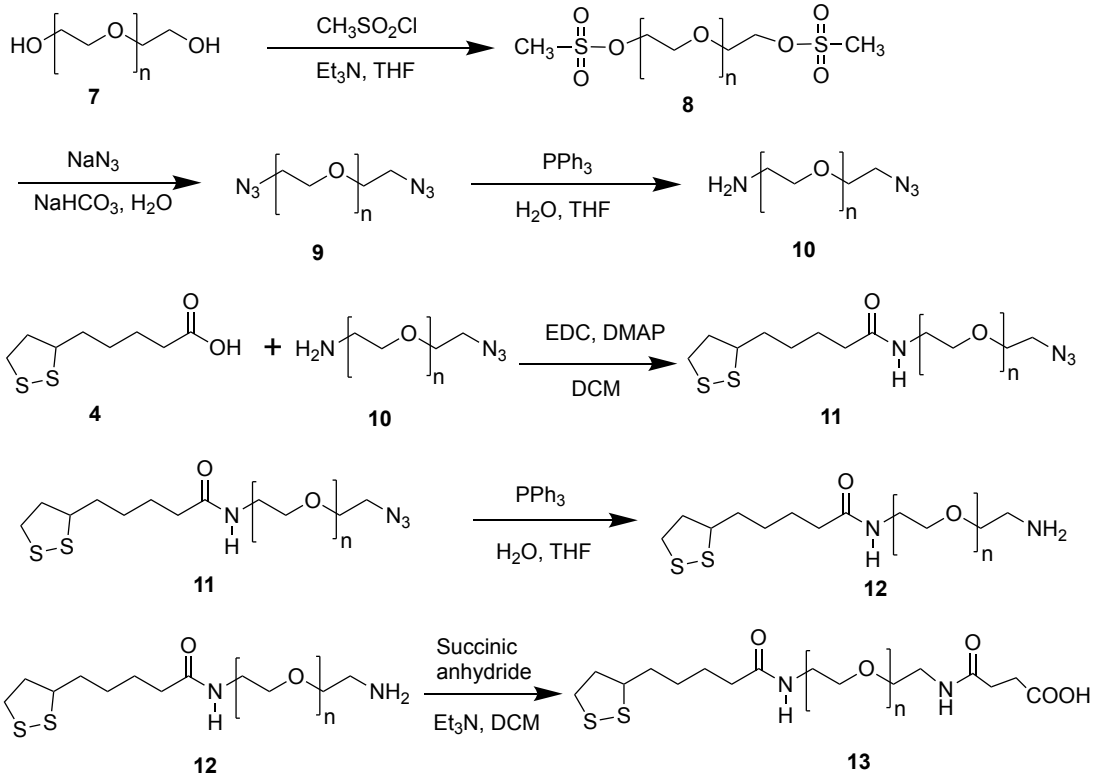

Scheme 3.2 Synthesis of TA-PEG400-NH_2.

To synthesize N_3-PEG400-N_3 **(9)**, PEG (MW ~ 400 Da, 5.0 g, ~25 mmol) and methane sulfonyl chloride (5.8 mL, 75 mmol,) were dissolved in THF (15 mL). The solution was cooled to 0 °C in an ice bath and triethylamine (7.6 mL, 55 mmol) was added dropwise to the reaction over 5 mins and stirred for 18 hours at room temperature. H_2O (30 mL) and sodium bicarbonate (1.78 g, 21 mmol) were added and the pH was

adjusted to ~ 8. Sodium azide (4.4 g, 68 mmol, 2.72 eq.) was added to the mixture. THF was distilled off and the residual solution was heated to 67 °C under stirring for 18 hours. The reaction mixture was cooled to room temperature and extracted with chloroform (5 × 50 mL). The combined organic phases were dried over anhydrous sodium sulfate, filtered and the solvent removed *in vacuo* to yield a waxy liquid (4.25 g, 76%). ^{1}H NMR (400 MHz, in $CDCl_3$): δ 3.62-3.75 (m), 3.41 (t, 4H, J = 5.0 Hz).

Synthesis of NH_2-PEG400-N_3 **(10)** were performed by mixing N_3-PEG400-N_3 (4.25 g, 7.7 mmol) and ethyl acetate (140 mL) in a 2-neck round bottom flask equipped with magnetic stirring bar. Solutin of 56 mL 1M HCl was added and stirred gently. Triphenylphosphine (6.90 g, 26.3 mmol) was dissolved in ethyl acetate (93 mL), and added dropwise at 0 °C over 30 min and stirred for 18 hours. The aqueous layer was then washed with ethyl acetate (2 × 50 mL) and stirred with KOH (10.58 g, 0.49 mol, 5 eq. *vs.* HCl) at 0 °C and the reaction solution was extracted with ethyl acetate (5 × 50 mL). The combined organic layers were dried over anhydrous sodium sulfate, filtered and the solvent was removed *in vacuo* to yield a waxy liquid (2.11g, 65% yield), which was used in the next step. TLC of the product was carried out using a 10: 1 (v/v) DCM: methanol eluent R_f ~ 0.1. ^{1}H NMR (400 MHz, in $CDCl_3$): δ 3.61-3.89 (m), 3.53 (t, 2H, J = 5.0 Hz), 3.40 (t, 2H, J = 5.0 Hz), 2.88 (t, 2H, J = 5.2 Hz).

To synthesize TA-PEG400-N_3 **(11)**, NH_2-PEG400-N_3 (2.10 g, 5 mmol), 4-(*N,N*-dimethylamino)pyridine (0.12 g, 1.03 mmol), EDC hydrochloride (1.02 g, 5.3 mmol, 1.03 eq.) were dissolved in DCM (30 mL) and cooled to 0 °C in ice. Lipoic acid (1.03

g, 5 mmol, 1 eq.) in DCM (18 mL) was added dropwise and the resulting solution was stirred at room temperature for 18 h. Then the reaction solution was washed with HCl (1 M, 50 mL) and with saturated $NaHCO_3$ (50 mL), dried over anhydrous sodium sulfate, filtered and the solvent was removed *in vacuo* to yield a yellow waxy liquid at room temperature (2.31 g, 71% yield). TLC of the product was carried out using a 10 : 1 (v/v) DCM: Methanol eluent resulting in $R_f \sim 0.6$. ^{1}H NMR (400 MHz, in $CDCl_3$): δ 6.29 (br s, 1H) 3.62-3.8 (m), 3.55-3.60 (m, 4H), 3.47 (t, 2H, J = 5.2 Hz), 3.41 (t, 2H, J = 5.4 Hz), 3.09-3.23 (m, 2H), 2.49 (m, 1H), 2.21 (t, 2H, J = 7.4 Hz), 1.93 (m, 1H), 1.71 (m, 4H), 1.49 (m, 2H).

Synthesis of TA-PEG400-NH_2 **(12)** were performed by dissolving TA-PEG400-N_3 (2.2 g, ~3.5 mmol) in dry THF (40 mL) under nitrogen atmosphere. Triphenylphosphine (1.38 g, 5.3 mmol) was added in one portion and stirred at room temperature for 30 min. Distilled water (0.63 mL, 35 mmol) was added to the reaction and stirred gently for 18 h. The solvent was removed under reduced pressure and ethyl acetate (30 mL) was added into the residue. A volume of 80 mL 1M HCl was added to the suspension and the aqueous layer was washed with ethyl acetate (4 × 50mL), basified Na_2CO_3 to pH ~ 9 and extracted with chloroform (5 × 50 mL). The combined organic layers were dried over anhydrous sodium sulfate, filtered and the solvent was removed *in vacuo* to yield a yellow waxy liquid at room temperature (1.55 g, ~73% yield). TLC was carried out using a 10:1 (v/v) DCM: Methanol eluent with the designed product having an $R_f \sim 0.1$. ^{1}H NMR (400 MHz, in $CDCl_3$): 3.5-3.73 (m), 3.44-3.5 (m, 4H),

3.09-3.24 (m, 2H), 2.87-3.0 (m, 2H), 2.63-2.76 (m, 2H)2.42-2.54 (m, 1H), 2.18-2.30 (m, 2H), 1.88-1.98 (m, 1H), 1.60-1.79 (m, 4H), 1.40-1.56 (m, 2H).

TA-PEG400-NH_2 (0.75 g, 1.24 mmol) and succinic anhydride (0.25 g, 2.50 mmol, 2 eq.) were dissolved in dry DCM (10 mL) under nitrogen atmosphere. Triethylamine (0.45 mL, 3.20 mmol, 2.6 eq.) was added in one portion and the reaction mixture was stirred at room temperature for 18 h. HCl (100 mL 1M) was the added to the solution and the aqueous layer was extracted with DCM (4 × 100 mL). The combined organic layers were dried over anhydrous sodium sulfate, filtered and the solvent was removed *in vacuo* to yield a yellow waxy liquid at room temperature (0.74 g, 93% yield). TLC was carried out using a 10:1 (v/v) DCM: Methanol giving an $R_f \sim 0.25$. ^{1}H NMR (400 MHz, in $CDCl_3$): 6.90–7.30 (br s, 1H), 6.20–6.70 (m, 1H), 3.60–3.74 (m), 3.52–3.60 (m, 5H), 3.44 (m, 4H), 3.07–3.22 (m, 2H), 2.66 (m, 2H), 2.55 (m, 2H), 2.41–2.51 (m, 1H), 2.21 (m, 2H), 1.83–1.96 (m, 1H), 1.57–1.76 (m, 4H), 1.38–1.53 (m, 2H).

3.2.1.3 Synthesis of TA/DHLA-PEG200-NH_2

Thioctic acid conjugated PEG amine with average molecular weight of 200 was synthesized using the same method as was described in Chapter 3.1.1.2 for 400 MW PEG. One additional step was required to reduce -S-S- to two thiols (Scheme 3.3). Detail are listed below.

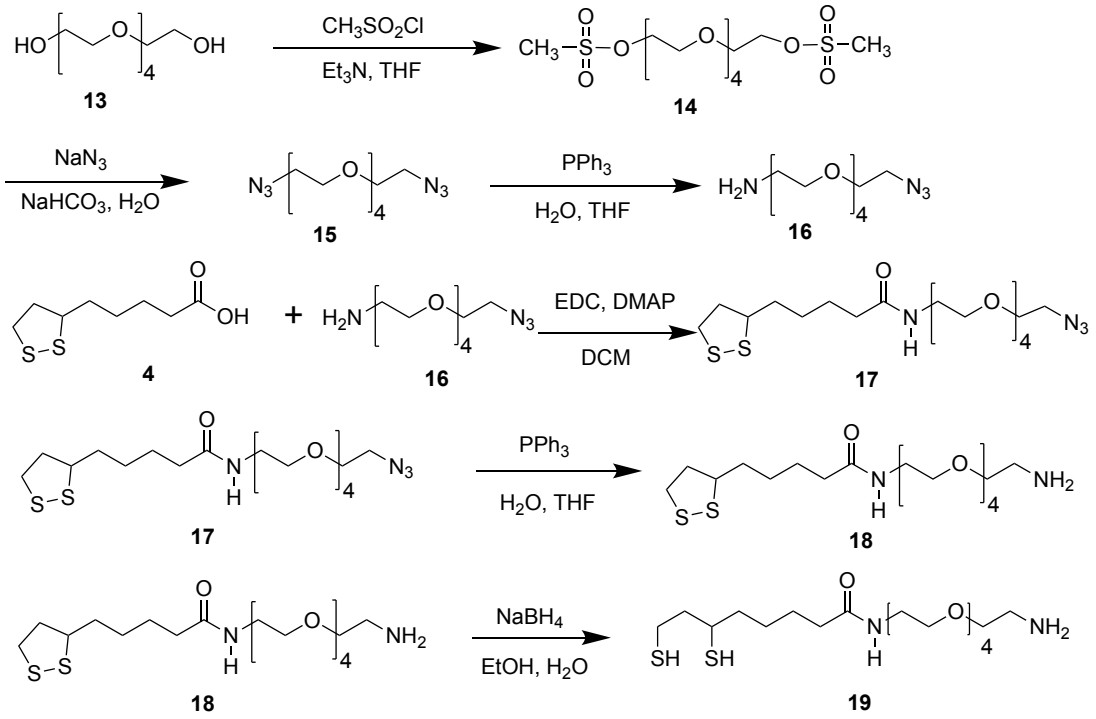

Scheme 3.3 Synthesis of TA/DHLA-PEG200-NH_2.

The first step, synthesis of N_3-PEG200-N_3 **(15)**, was performed by dissolving PEG methyl ether (MW ~ 200 Da, 5.0 g, 25 mmol) and methanesulfonyl chloride (4.5 mL, 57.4 mmol) in THF (30 mL). The solution was cooled to 0 °C in ice bath and triethylamine (8.6 mL, 61.5 mmol) was added dropwise to the reaction using a dropping addition funnel and stirred overnight. H_2O (30 mL) was added into the mixture. $NaHCO_3$ (1.78 g, 21 mmol) was used to adjust the solution pH to ~ 8. Sodium azide (4.43 g, 68.13 mmol) was added. The content was heated to 67 °C to distill off THF and refluxed overnight. The reaction was cooled to room temperature and extracted with chloroform (5 × 50 mL). The combined organic layers were dried over sodium sulfate anhydrous, filtered and the solvent removed *in vacuo* to yield a waxy liquid at room temperature. The crude product was purified by column

chromatography on silica gel with 20: 1 (v/v) DCM: Methanol as eluent to yield a yellow waxy liquid at room temperature (~90% yield). TLC of the product was carried out using a 10: 1 (v/v) DCM: Methanol eluent resulting in R_f ~ 0.75. 1H NMR (400 MHz, in $CDCl_3$): δ 3.62-3.75 (m), 3.41 (t, 4H, J = 5.0 Hz).

N_3-PEG200-N_3 was then used to synthesis NH_2-PEG200-N_3 **(16)**. N_3-PEG200-N_3 (6.0 g, 24 mmol) was dissolved in ethyl acetate (140 mL) in a 2-neck round bottom flask equipped with magnetic stirring bar. HCl (56 mL 1 M) solution was added and stirring gently. Triphenylphosphine (6.9 g, 26.3 mmol) was dissolved in ethyl acetate (93 mL) and added dropwise using a dropping funnel in an ice bath below 5 °C and further stirred overnight. The suspension was transferred into a separating funnel, and the aqueous layer was washed with ethyl acetate (2×50 mL). The aqueous layer was basified with KOH (0.49 mol) at 0 °C. The remaining solution was extracted with ethyl acetate (5×50 mL). The combined organic layers were dried over sodium sulfate anhydrous, filtered and the solvent was removed *in vacuo* to yield a waxy liquid (~80%) at room temperature. TLC was carried out using a 10: 1 (v/v) DCM: Methanol giving an R_f ~ 0.1. ^{1}H NMR (400 MHz, in $CDCl_3$): δ 3.61-3.89 (m), 3.53 (t, 2H, J = 5.0 Hz), 3.40 (t, 2H, J = 5.0 Hz), 2.88 (t, 2H, J = 5.2 Hz).

The synthesis of TA-PEG200-N_3 **(17)** was achieved by dissolving NH_2-PEG200-N_3 (4.0 g, ~ 17.8 mmol), 4-(*N, N*-dimethylamino) pyridine (0.46 g, 3.57 mmol), *N*-(3-dimethylaminopropyl)-*N'*-ethylcarbodiimide hydrochloride (3.45 g, 18.00 mmol) in DCM (100 mL) and cooled to 0 °C in ice bath. Thioctic acid (3.67 g, 17.80 mmol)

dissolved in DCM (62.5 mL) was added using an addition funnel and stirred overnight. The solvent was removed *in vacuo* and deionized water (120 mL) was added to the residue. The aqueous layer was washed with hexane (4×50 mL) and then saturated with solid $NaHCO_3$. The remaining solution was extracted by DCM (4×100 mL). The combined organic layers were dried over sodium sulfate anhydrous, filtered and the solvent was removed *in vacuo* to yield a yellow waxy liquid at room temperature (~ 49 % yield). TLC was carried out using a 10: 1 (v/v) DCM: Methanol eluent resulting in $R_f \sim 0.6$. ^{1}H NMR (400 MHz, in $CDCl_3$): δ 6.29 (br s, 1H) 3.62-3.8 (m), 3.55-3.60 (m, 4H), 3.47 (t, 2H, J = 5.2 Hz), 3.41 (t, 2H, J = 5.4 Hz), 3.09-3.23 (m, 2H), 2.49 (m, 1H), 2.21 (t, 2H, J = 7.4 Hz), 1.93 (m, 1H), 1.71 (m, 4H), 1.49 (m, 2H).

To synthesize TA-PEG200-NH_2 **(18)**, TA-PEG200-N_3 (2.20 g, ~5.29 mmol) was dissolved in dry THF (50 mL) in a 2-neck round bottom flask equipped with magnetic stirring bar. Triphenylphosphine (2.08 g, 7.93 mmol) was added and further stirred at room temperature for 30 mins. Water (0.96 mL, 5.29 mmol) were added to the reaction and stirred gently for 48 h. The solvent was removed *in vacuo* and ethyl acetate (100 mL) was added into the residue. HCl (100 mL, 1 M) was added. The aqueous layer was washed with ethyl acetate (4×50 mL) and basified with solid Na_2CO_3 (to pH ~ 9). The reaction mixture was extracted by chloroform (4×100 mL). The combined organic layers were dried over anhydrous sodium sulfate, filtered and the solvent was removed *in vacuo* to yield a yellow waxy liquid at room temperature (~54% yield). TLC was carried out using a 10: 1 (v/v) DCM: Methanol eluent resulting in $R_f \sim 0.1$.

^{1}H NMR (400 MHz, in $CDCl_3$): 3.5-3.73 (m), 3.44-3.5 (m, 4H), 3.09-3.24 (m, 2H), 2.87-3.0 (m, 2H), 2.63-2.76 (m, 2H), 2.42-2.54 (m, 1H), 2.18-2.30 (m, 2H), 1.88-1.98 (m, 1H), 1.60-1.79 (m, 4H), 1.40-1.56 (m, 2H).

The last step, synthesis of DHLA-PEG200-NH_2 **(19)**, was performed by mixing TA-PEG200-N_3 (0.43 g, ~ 1 mmol), ethanol (7 mL) together under 0 ° C. $NaBH_4$ dissolved in water (3 mL) (0.15g, 4 mmol) was added and further stirred for 4 h. The solvent was removed *in vacuo* and brine (30 mL) was added into the residue. The reaction mixture was extracted by DCM (4×50 mL). The combined organic layers were over sodium sulfate anhydrous, filtered and the solvent was removed *in vacuo* to yield a yellow waxy liquid at room temperature (~ 55 % yield). 1H NMR (400 MHz, in $CDCl_3$): 3.62–3.72 (m), 3.51–3.61 (m, 4H), 3.43–3.50 (m, 2H), 2.93 (m, 1H), 2.88 (t, 2H, J = 5.2 Hz), 2.63–2.80 (m, 2H), 2.21 (t, 2H, *J* = 7.4 Hz), 1.87–1.98 (m, 1H), 1.40–1.81 (m, 7H).

3.2.2 Synthesis of targeting ligands

Folic acid was chosen as targeting ligand. The procedure was developed and used to conjugate with PEG ligands, described in Chapter 3.1.1.

3.2.2.1 Synthesis of TA-PEG-NH_2-maleimide.

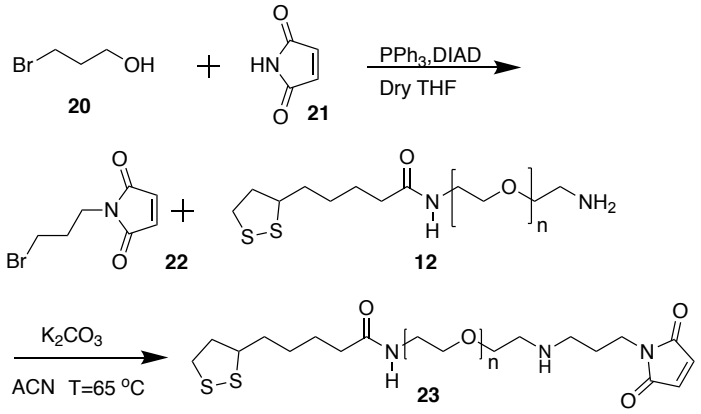

Scheme 3.4 Synthesis route of TA-PEG-NH_2-maleimide.

To synthesize $BrCH_2CH_2CH_2$-maleimide **(22)**, a 3-neck 100 ml round-bottom flask containing triphenylphosphine (1.67 g, 6.4 mmol) and a magnetic stirring bar. Dry THF (40 mL) was added and the solution was degassed with N_2 for 10 mins. The flask was cooled to - 78 °C. Diisopropyl azodicarboxylate (DIAD, 1.25 mL, 6.4 mmol) and 3-bromo-1-propanol (0.58 mL, 6.4 mmol) were added dropwise to the mixture and stirred for 5 mins. Maleimide (0.75 g, 7.68 mmol) was added to the reaction. After all maleimide had dissolved, the dry ice was removed, and the reaction was stirred overnight at room temperature under argon atmosphere. Concentrated the reaction to 5 ml after all maleimide has been reacted. The crude product was purified by column

chromatography on silica gel using 1: 2 (v/v) EtOAc: Hexane as eluent to yield a white powder at room temperature (~27% yield). ^{1}H NMR (400 MHz, in $CDCl_3$): δ 6.70 (s, 2H), 3.68 (t, J = 6.6 Hz, 2H), 3.36 (t, 2H, J = 6.6 Hz), 2.08- 2.30 (m, 2H).

The TA-PEG-NH_2 was used to synthesize TA-PEG-$NHCH_2CH_2CH_2$-maleimide **(23)**. TA-PEG-NH_2 (258 mg, 0.55 mmol), anhydrous K_2CO_3 (83 mg, 0.6 mmol) and $BrCH_2CH_2CH_2$-maleimide (108 mg, 0.5 mmol) were dissolved in CH_3CN (3 mL). The yellow solution was stirred at 65 °C for 18 h. The solvent was evaporated *in vacuo*, then water (5 mL) was added to the residue, and the mixture solution was extracted with DCM (3×5 mL). The combined organic phases were washed with saturated aqueous NaCl (10 mL), dried over sodium sulfate, and filtered. The solvent was evaporated *in vacuo*. The residue was purified by the silica gel chromatography using a mixture of petroleum/acetone (2:1, v/v) as eluent to obtain the oily products. ^{1}H NMR (400 MHz, in $CDCl_3$): 3.5-3.73 (m), 3.44-3.5 (m, 4H), 3.09-3.24 (m, 2H), 2.87-3.0 (m, 2H), 2.63-2.76 (m, 2H), 2.42-2.54 (m, 1H), 2.18-2.30 (m, 2H), 1.88-1.98 (m, 1H), 1.60-1.79 (m, 4H), 1.40-1.56 (m, 2H).

3.2.2.2 Synthesis of TA-PEG-COOH-maleimide

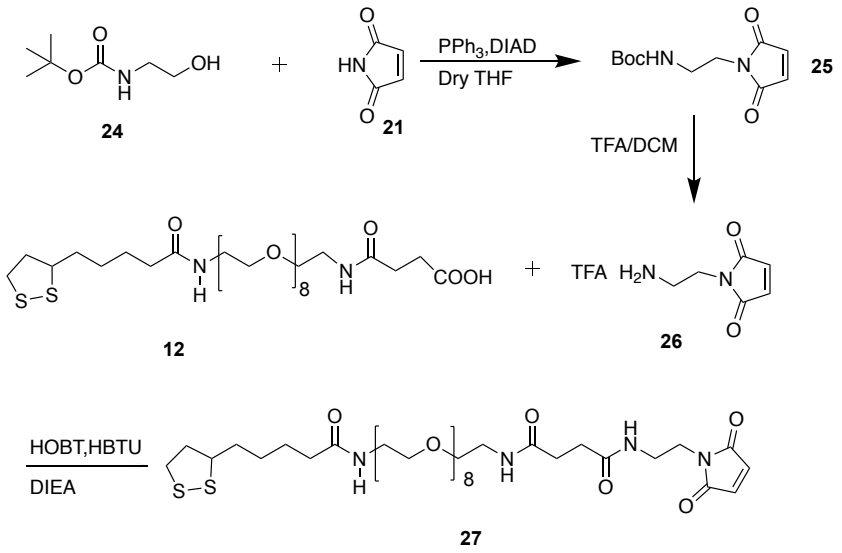

Scheme 3.5 Synthesis route of TA-PEG-COOH-maleimide.

To produce Boc-NHCH$_2$CH$_2$-maleimide **(25)**, a 3-neck 100 mL round-bottom flask was charged with triphenylphosphine (1.67 g, 6.4 mmol) and a stirring bar, to which was added dry THF (40 mL) and been degassed with N_2 for 10 min. The reaction mixture was then cooled to - 78 °C. DIAD (1.25 mL, 6.4 mmol) was added dropwise to the mixture and *N*-Boc-ethanolamine (1.03 g, ~ 0.99 mL, 6.4 mmol) was added dropwise to the reaction and stirring for 5 mins. Maleimide (0.75 g, 7.68 mmol) was then added to the reaction mixture. After all the maleimide had dissolved, the reaction mixture was allowed to warm to RT. Further stirring overnight at room temperature under argon. The crude product was chromatographed on silica gel with 1: 2 (v/v) EtOAc: Petro (with 5% Et_2O) as eluent to yield a white powder at room temperature (~24.5 % yield). ^{1}H NMR (400 MHz, in $CDCl_3$): δ 6.70 (s), 3.66 (m, 2H), 3.33 (q, 2H, J = 5.9 Hz), 1.40 (s, 9H).

Then synthesis of $NH_2CH_2CH_2$-maleimide **(26)** was performed, Boc-$NHCH_2CH_2$-maleimide (0.34 g, 1.42 mmol) was loaded in a 50-mL round bottom flask, Trifluoroacetic acid (4.75 mL), triisopropylsilane (0.125 mL) and H_2O (0.125 mL) were added sequentially to the reaction mixture and stirred for 4 h. The TFA was evaporated *in vacuo*, followed by addition of 20 ml Et_2O to the pink residue. Precipitate was filtered. The product was obtained as a white powder after drying in vacuum. ^{1}H NMR (400 MHz, Methanol-d_4) δ 6.92 (s, 2H), 3.83 (dd, J = *5.2, 6.3* Hz, 2H), 3.17 (dd, J = *5.2, 6.3* Hz, 2H)

The next step was to performing synthesis of TA-PEG-$CONHCH_2CH_2$-maleimide **(27)**, $NH_2CH_2CH_2$-maleimide (50.4 mg, 0.09 mmol) and TA-PEG-COOH (15.00 mg, 0.11 mmol) were dissolved in dimethylformamide (DMF, 1.5 mL), 1-Hydroxybenzotriazole (HoBt, 8.5 mg, 0.11 mmol), *O*-(benzotriazol-1-yl)-*N, N, N′, N′*-tetramethyluronium hexafluorophosphate (HBTU, 20 mg, 0.1 mmol), *N,N*-diisopropylethylamine (DIPEA, 12.9 μL, 0.15 mmol) were added to the reaction sequentially and the reaction mixture was stirred overnight. H_2O (15 mL) was added to the reaction, and the product was extracted with DCM (2×10 mL). The organic layer was washed with 1M HCl (2×10 mL) solution and then brine (2×10 mL). Residual solvents were evaporated and a yellow powder product was obtained. ^{1}H NMR (400 MHz, in $CDCl_3$): 7.01 (s, 2H), 6.20–6.70 (m, 1H), 3.60–3.74 (m), 3.52–3.60 (m, 5H), 3.44 (m, 4H), 3.07–3.22 (m, 2H), 2.66 (m, 2H), 2.55 (m, 2H), 2.41–2.51 (m, 1H), 2.21 (m, 2H), 1.83–1.96 (m, 1H), 1.57–1.76 (m, 4H), 1.38–1.53 (m, 2H).

3.2.2.3 Michael addition of FA-SH to maleimide linkers

The coupling of folic acid with cystamine (FA-SH) **(28)** was performed by dissolving folic acid (1.00 g, 2.26 mmol) in dry DMF (20 mL) in the dark. *N*-Hydroxysuccinimide (0.26 g, 2.26mmol) and *N, N*′-dicyclohexylcarbodiimide (EDC, 0.31 g, 1.52 mmol) was added and stirred for 20 h. The resulting precipitate was removed by filtration. The solvents were evaporated *in vacuo* to yield FA-NHS. FA-NHS (0.12 g, 0.23 mmol) was dissolved in pyridine (10 mL), cystamine hydrochloride (0.026 g, 0.23 mmol) was added to the reaction and stirred for another 20 h in the dark. The reaction mixture was concentrated *in vacuo* to yield product FA-SH in yellow powder. Negative Mass Spectrum show the compound peaks at 499^{1-} (expecting was 500). ^{1}H NMR (400 MHz, DMSO-d_6) δ 10.53 (s, 1H), 8.70 – 8.62 (m, 5H), 8.03 – 7.94 (m, 3H), 7.69 – 7.61 (m, 3H), 7.55 (ddd, *J = 1.5, 4.4, 7.7* Hz, 4H), 6.95 (s, 1H), 6.64 (d, *J = 8.7* Hz, 3H), 4.49 (s, 2H), 2.59 (s, 5H), 1.23 (s, 2H).

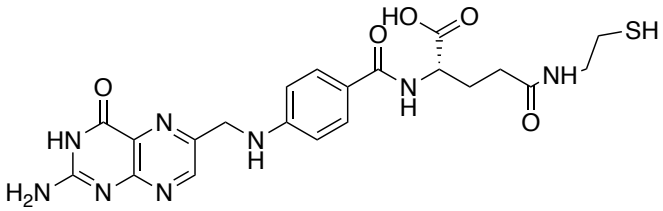

28

Scheme 3.6 Chemical structure of FA-SH.

Then the FA-SH obtained was attached to maleimide **(29)**. Acetonitrile: H_2O in ratio 1:1 (2 mL) was prepared as reaction solvents and the mixture adjusted pH was adjusted to 8, TA-PEG-CONHCH$_2$CH$_2$-maleimide (10 mg, 0.014 mmol) and FA-SH (7.43 mg,

0.015 mmol) were sequentially added to the reaction and stirred overnight. Mass spectrometry revealed the desired peak in our compound and NMR results confirmed the formation of desired products in solutions. ^{1}H NMR (400 MHz, 90% H_2O + 10% D_2O) δ 8.62 – 8.52 (m, 1H), 8.48 – 8.36 (m, 0H), 7.72 – 7.59 (m, 2H), 7.59 – 7.49 (m, 1H), 6.88 – 6.75 (m, 2H), 6.70 – 6.58 (m, 1H), 4.83 (s, 2H), 4.59 (s, 1H), 4.43 – 4.24 (m, 3H), 3.71 – 3.60 (m, 6H), 3.61 (s, 11H), 3.53 (s, 1H), 3.41 – 3.29 (m, 1H), 3.29 – 3.19 (m, 1H), 2.50 – 2.15 (m, 7H), 2.05 (td, *J* = 7.0, 9.2 Hz, 0H), 1.99 (s, 7H), 1.52 (s, 2H), 1.28 (s, 4H).

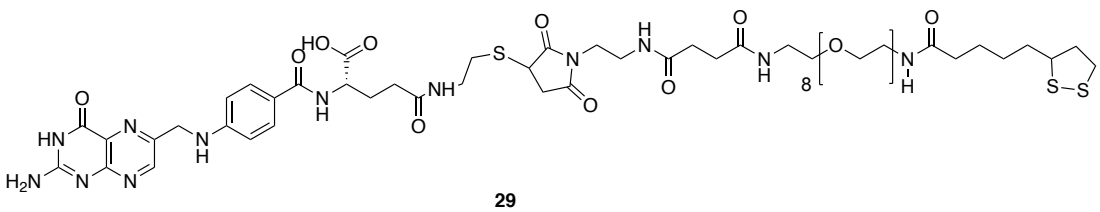

29

Scheme 3.7 Chemical structure of FA-SH-maleimide-PEG-TA.

3.2.2.3 Conjugation of FA to TA-PEG based ligands

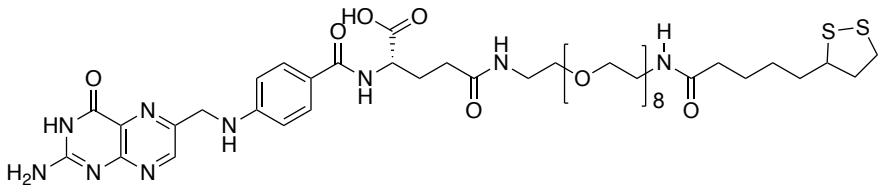

30

Scheme 3.8 Chemical structure of FA-PEG-TA.

Folic acid (0.16 g, 0.36 mmol) was dissolved in DMSO (10 mL). *N*-(3-Dimethylaminopropyl)-*N′*-ethylcarbodiimide hydrochloride (0.104 g, 0.544 mmol) and *N*-hydroxysuccinimide (64 mg, 0.544 mmol) were added to the reaction and stirred

for 20 h in the dark (covered with aluminium foil). TA-PEG200-NH_2 (0.4197 g, 1.08 mmol) was added to the mixture and further stirred overnight. A light-yellow precipitate was obtained and filtered after adding of acetone (50 mL). The dried solid precipitate was dissolved in EtOAc (40 mL). The organic layer was washed with brine (5×50 mL) and dried over an anhydrous Na_2SO_4. All solvents were evaporated and the final product (yellow oily solid) was obtained by drying the residues under vacuum. ^{1}H NMR (500 MHz, DMSO-d_6) δ 8.60 (d, J = 3.1 Hz, 1H), 7.81 (s, 2H), 7.61 (ddd, J = 2.3, 4.6, 8.9 Hz, 2H), 6.89 (s, 1H), 6.60 (dd, J = 2.5, 8.9 Hz, 2H), 4.44 (d, J = 6.1 Hz, 2H), 3.50 – 3.41 (m, 6H),, 3.20 – 3.02 (m, 6H), 3.01 – 2.90 (m, 2H), 2.76 (s, 2H), 2.43 – 2.32 (m, 1H), 2.17 – 2.05 (m, 1H), 2.02 (t, J = 7.1 Hz, 2H), 1.88 (s, 2H), 1.95 – 1.76 (m, 2H), 1.65 – 1.46 (m, 1H), 1.31 – 1.24 (m, 2H).

3.2.3 Synthesis of Au NCs

3.2.3.1 Organic soluble Au NCs

Chloroauric acid was used as a precursor that been transferred into toluene by TOAB (phase transfer agents), NCs were capped with thiolate ligands and $NaBH_4$ was used as the reducing agent. The ratio of Au to ligands was 1:3. (as shown in Scheme 3.9). Details are given below:

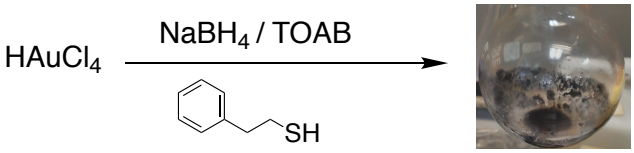

Scheme 3.9 Scheme of organic-soluble Au NCs synthesis and photo of synthesized Au_{25}.

To synthesize *2*-phenylethanethiol capped Au nanoparticles, chloroauric acid (158 mg, 0.4 mmol) was dissolved in deionized water (5mL). Tetraoctylamminoium bromide (TOAB, 256 mg, 0.47 mmol) dissolved in toluene (10 mL) was added and the biphsic mixture was stirred vigorously for 15 min to mix the two phases. The phases were separated, and aqueous phase was discarded. The organic layer was cooled to 0 ^{o}C under nitrogen and 2-phenylethanethiol (0.17 mL, 1.2 mmol) added and stirred gently for 1h. Sodium borohydride aqueous solution (7.00 mL, 4 mmol, 0.57 mM) was added and vigorously stirred overnight under nitrogen to obtain crude Au NCs. The two layers were separated and aqueous phase removed. The organic layer was concentrated *in vacuo* and the black powders obtained were dissolved in ethanol (20 mL) to remove

impurities. The Au NCs were collected after removing the supernatant.

3.2.3.2 Synthesis of dodecanethiol capped Au nanoparticles

The synthesis of dodecanethiol capped Au nanoparticles was achieved by dissolving chloroauric acid (33 µL, 1M, 0.033 mmol) in deionised water (5 mL). TOAB (0.036 g, 0.066 mmol) was dissolved in toluene (10 mL) and added to the mixture under vigorously stirring to mix the two phases for 10 min at room temperature. Dodecanethiol(1.65 mL, 0.02 M, 0.033 mmol) in toluene was added and the solution stirred vigorously for 10 min. Sodium borohydride aqueous solution (0.5 mL, 0.66 M, 0.33 mmol,) was added dropwise and vigorously stirred overnight. The two layers were separated and aqueous phase removed. The organic layer was washed with H_2O (3×20 mL), dried over anhydrous sodium sulphate, and concentrated *in vacuo* and the product was dissolved in ethanol (50 mL) to remove impurities. After 24 hrs storage at - 20 °C, the Au NPs were collected by filtering the solution through a 0.45 µm pore size PTFE membrane. The solid product was washed with ethanol and acetone and dried under vacuum to obtain the Au NPs.

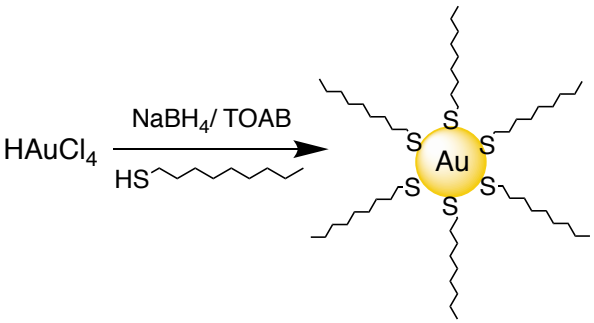

Scheme 3.10 Scheme of synthesis of Au NPs capped with dodecanthiol.

3.2.3.3 Synthesis of water-soluble Au NCs

Generally, chloroauric acid was used as a source of gold, mixed with ligands under an alkaline environment (pH ~ 11) in deionized water, reduced by $NaBH_4$. The ratio of gold to ligands was 1:3. Following centrifugation/filtration using a Millipore unit, a concentrated brown solution was produced (as shown in Scheme 3.11). Details are given below:

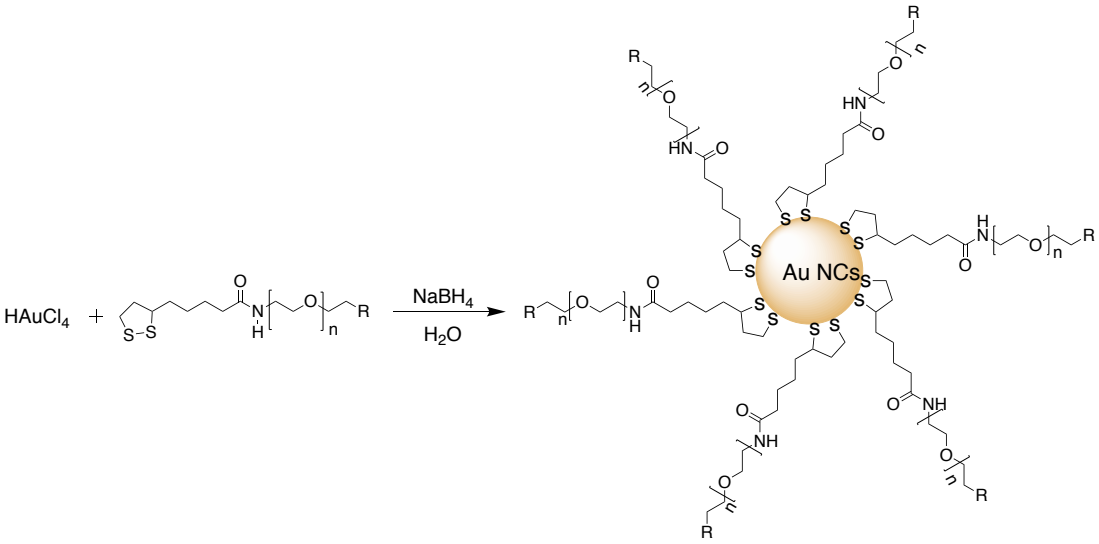

Scheme 3.11 Scheme of Au NCs synthesis with PEG based ligands

Firstly, Au NCs capped with DHLA-*O*-mPEG500 were synthesized. DHLA-*O*-mPEG500 (30 μmol) was dissolved in deionized water (20 mL) which contained sodium hydroxide (50 μl, 2 M). Chloroauric acid (10 μL, 1 M) was added and stirred gently for 5 min. Sodium borohydride aqueous solution (400 μL, 50 mM) was added dropwise and moderately stirred overnight at room temperate to obtain crude Au NCs. The solution obtained was purified by centrifugation at 4000*g* and filtrated with a

molecular weight cut-off of 10 kDa membrane. The procedure was repeated 3 times. The resulting solutions were stored at 4 °C.

Then, the synthesis of Au NCs capped with TA-NH-mPEG550 was carried out, TA-NH-mPEG500 (30 μmol) was dissolved in deionised water (20 mL) which contained sodium hydroxide (50 μL, 2 M). Then chloroauric acid (10 μl, 1 M) was added and the reaction stirred gently at ~ 300 rpm for 5 min. Sodium borohydride solution (400 μL, 50 mM) was added dropwise and stirred at ~ 600 rpm overnight at room temperate to obtain crude Au NCs. The obtained solution was purified 3 time with a molecular weight cut-off of 10 kDa centrifugation/filtration unit. The resulting solutions were stored at 4 °C until further use.

Au NCs capped with DHLA-NH-PEG400-NH_2 were also synthesized. DHLA-NH-PEG400-NH_2 (30 μmol) was dissolved in deionized water (20 mL) which contained sodium hydroxide (50 μL, 2 M). Chloroauric acid (10 μL, 1 M) was added and the solution stirred gently for 5 min. Sodium borohydride solution (400 μL, 50 mM) was added dropwise and moderately stirred overnight at room temperate to obtain crude Au NCs. The obtained solution was purified 3 times *via* centrifugation/filtration with a molecular weight cut-off of 10 kDa membrane filtration device. The resulting solutions were stored at 4 °C until required.

To produce NCs with shorter ligands, the DHLA-NH-PEG200-NH_2 (30 μmol) was dissolved in deionized water (20 ml) which containing sodium hydroxide (50 μL, 2 M). Chloroauric acid (10 μL, 1 M) was added and stirred gently for 5 min. Sodium

borohydride solution (400 μL, 50 mM) was added dropwise and moderately stirred overnight at room temperate to obtain crude Au NCs. The solution obtained was purified 3 times *via* centrifugation/filtration with a molecular weight cut off membrane filter of 10 kDa. The resulting colloidal solutions were stored at 4 °C until further use.

3.1.3.7 Synthesis of Au NCs capped with TA-NH-PEG200-NH-FA

TA-NH-PEG200-NH-FA (30 μmol) was dissolved in deionized water (20 ml) which contained sodium hydroxide (50 μL, 2 M). Chloroauric acid (10 μL, 1 M) was added and the solution was stirred gently for 5 min. Sodium borohydride solution (400 μL, 50 mM) was added dropwise and moderately stirred overnight at room temperate to obtain crude Au NCs. The obtained solution was purified 3 cycles of centrifugation/filtration with a molecular weight cut-off of 10 kDa membrane filtration device. The resulting solutions were stored at 4 °C until required.

3.3 *In vitro* studies

3.3.1 Tissue culture

Human derived cell lines were acquired from The American Type Culture Collection (ATCC) and used in this study, including HCT-116, human colon cancer cell line; MCF-7, human breast cancer cell line; MDA-MB-231, another human breast cancer cell line; A549, human lung cancer cell line.

MDA-MB-231 was chosen as the folate receptor (FR) positive cell line, and A549 was

chosen as FR negative. HCT-116, MCF-7 were also used.

All cell lines were maintained at 37 °C under a humidified atmosphere of 5% CO_2 / 95% air in RPMI nutrient medium supplemented with 10 % (v/v) fetal bovine serum.

3.3.2 Cell proliferation assay

The (3-(4,5-dimethylthiazol-2-yl)-2,5-diphenyltetrazolium bromide (MTT) assay[209] is one of the cell assays used for measuring the mitochondrial activity and estimating viability of cells. Normally, cell-based assays are used for screening collections of compounds to determine if the test molecules have effects on cell proliferation or show direct cytotoxic effects that eventually lead to cell death.

MTT is positively charged and readily penetrates viable eukaryotic cells. Viable cells with active metabolism convert MTT into a purple colored formazan product with an absorbance maximum at 550 nm. When cells die, they lose the ability to convert MTT into (*E,Z*)-5-(4,5-dimethylthiazol-2-yl)-2,5-diphenylformazan (formazan), thus formation of formazan serves as a marker of the viability of cells. The exact cellular mechanism of MTT reduction into formazan is not well understood, but likely involves reaction with NADH or similar reducing molecules that transfer electrons to MTT.[209]

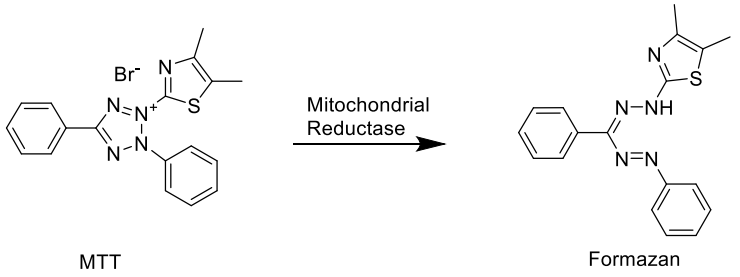

Scheme 3.12 Transformation of MTT to formazan.

For MTT assays, all studied cells were seeded into a 96-well flat bottom plate at a density of 3000 cells/well. Cells were allowed 24 hours to adhere prior to treatment. Au NCs were used at final concentrations ranging from 10 nM to 100 μM. One-column of wells was treated with medium only as a control. For each treatment concentration, 6 wells of each column were used. Following 72 h of exposure to Au NCs, medium with treatment agent was aspirated and 50 μL of 2 mg/mL of MTT was added. The plate was incubated for 2.5 hours at 37 °C and 5 % CO_2, allowing for the formation of purple crystals. The media was carefully removed, and the crystals were dissolved in dimethyl sulfoxide (150 μL per well). Absorbance values at 550 nm were recorded using an EnVision® Multilabel Plate Reader (PerkinElmer) and cell viability was estimated as a percentage of absorbance compared to untreated control cells.

3.3.3 Cellular uptake detection

Celluar uptake of Au NPs was assessed using ICP-MS, The Au NP solutions were studied to determine the exact treatment concentration of Au NP and to compare to that uptaken by the cells. The cells studied were seeded into a 6-well plate at ~10^5 cells per well and incubated for 24 hours. The medium was aspirated, and treatment agent

added (2 mL/well). Cells were exposed to Au NCs for 24 hours and washed with PBS (3×2 mL) to remove extracellular Au NCs. Then 16 M HNO_3 (142 μL) was added to digest cells for 30 mins. The solution was diluted with deionized water to 5 ml to make ICP-MS samples.

The concentrations of corresponding treated Au NC solutions were also probed by ICP-MS. The samples are made up to a minimum volume of 5 mL with 2 % w/v nitric acid concentration in the final solution. The detailed results will be discussed in Chapter 6.

Chapter 4

Development of water-soluble PEG-capped gold nanoclusters

Gold nanoparticles with a diameter less than 3 nm are defined as gold nanoclusters (Au NCs). They do not show the surface plasmon resonance (SPR) effect observed in Au nanoparticles (NPs), which corresponds to absorption peak around 520 nm along UV/Vis spectra. However, due to their ultra-small size, they do exhibit unique physical and chemical properties arising from strong quantum size effects.[210]

4.1 Synthesis of Au NPs in organic solvents

Jin's group at Carnegie Mellon University have performed comprehensive studies on the thiol protected gold nanoclusters which are soluble in organic solvents.[95] Atomically precise nanoclusters were produced in a controlled manner, with magic number clusters of gold atoms, *i.e.* 25, 64, 144. The diameter of these clusters is below 2 nm.[54, 66, 211]

The sizes of gold nanoparticles can be controlled and tuned by modifying the synthesis parameters, such as, the choice of reductants,[212, 213] ratio of gold to ligands,[214] pH of the reaction,[215] and aging time. [216]

To grow ultra-small gold nanoparticles with diameter less than 2 nm, we followed a one pot protocol for synthesis of Au NC (Au_{25}) in an organic solvent.[17] In this method, chloroauric acid was used as a precursor. It was solubilized in toluene by a phase transfer agent tetraoctylamminoium bromide (TOAB). The 2-phenylethanethiol

(HSC_2H_4Ph) was used as the capping ligand and $NaBH_4$ was used as the reducing agent. The used Au to ligands molar ratio was 1:3. During the synthesis, particle aggregation was observed, and a black precipitate formed (see Figure 4.1).

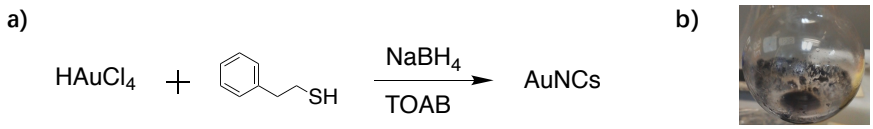

Figure 4.1 a) Synthesis scheme of 2-phenylethanethiol capping Au NCs and **b)** photograph of synthesized precipitated Au_{25}.

We proposed that precipitation occurred due to unsuccessful NC surface passivation by the short chain ligand. Hence, we decided to replace it with a longer chain capping molecule, dodecanethiol, as a stabilizing agent.[217] The procedure was repeated as follows, chloroauric acid was mixed with TOAB and dodecanthiol and was then reduced by $NaBH_4$ at room temperature (Figure 4.2). The molar ratio of Au to ligands in this case was 1:1. The resulting mixture was filtered through a 0.2 μm PTFE membrane and a brown precipitate was collected. An aging time of 20 h was used. We note, that to produce Au NPs, the cleanliness of glassware was critical, no particles were formed unless the glassware was thoroughly pre-cleaned with *aqua regia*.

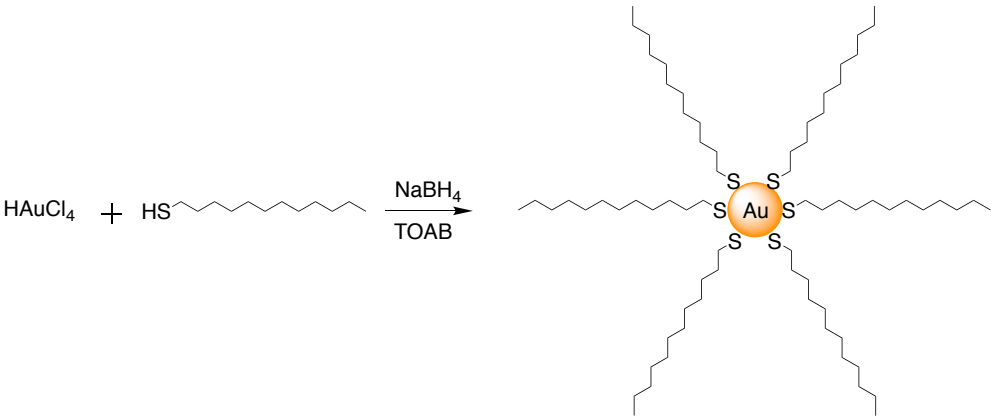

Figure 4.2 Synthesis scheme of dodecanthiol-Au NCs.

In order to assess the properties of the NC formed, we used TEM imaging and UV/Vis spectroscopy. For the TEM studies, the produced brown Au NPs were dispersed in *iso*-propane and deposited on graphene oxide copper grids. Images were acquired on a JEOL-2100F microscope operated by Dr M. Fay (Nano and Microscale Research Centre (nmRC), Nottingham). From the analysis of TEM and HR-TEM images (Figure 4.3), it was found that nanoparticles are spherical in shape with an average diameter of $d_{AuNP} = 2.2 \pm 0.4$ nm.

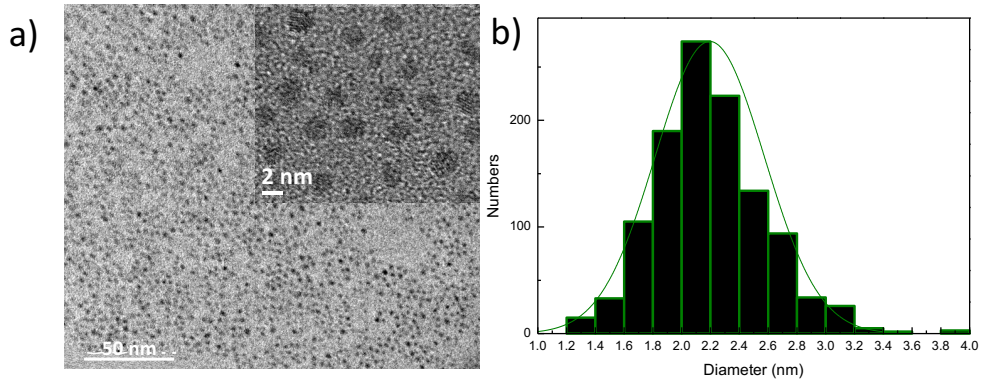

Figure 4.3 a) Representative TEM and (inset) HR-TEM images of Au NP. **b)**

Histogram of size distribution of dodecanthiol capped Au NCs.

Studies of the absorption of the NC solutions in *iso*-propane (Figure 4.4) revealed a main no distinct peak along the profile. The absorbance profile observed at $\lambda < 400$ nm is characteristic for *d-sp* transition in gold.[218] For nanoparticles with diameter $d >$ 3 nm, resonance peak is observed at 520 nm.[219-222] The TEM studies show that our Au NCs have average d = 2.2 ± 0.4 nm. Hence no peak is observed at ~ 520 nm.

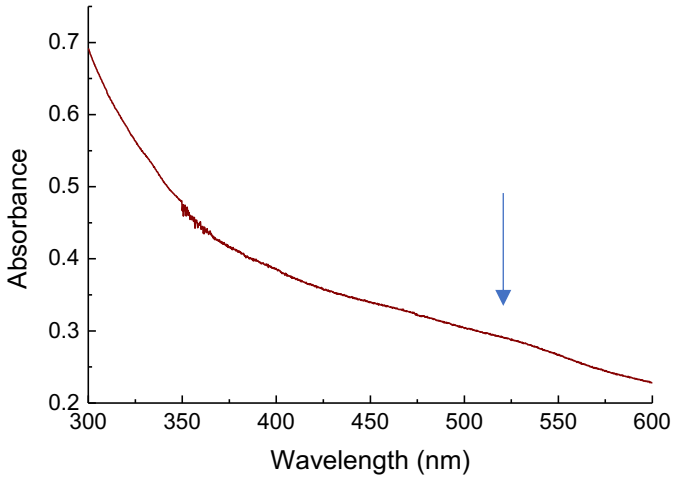

Figure 4.4 Representative absorption spectrum of dodecanthiol capped Au NCs with diameter $d_{AuNP} = 2.2 \pm 0.4$ nm.

In this study, we have demonstrated that the Au NCs with diameter around 2 nm was successfully obtained, however, its applications in bio-system are largely restricted due to their insolubility in water. Water-soluble Au NCs are required to fulfill the project objectives.

4.2 Synthesis of PEG based ligands

For biological applications, solubility and stability of compounds under physiological

solvents is paramount. Several methods have been reported, which address this goal, *e.g.* ligand exchange,[61] or further modification of ligands.[222] However, ligand exchanges is time-consuming because at least a two-step reaction procedure is required, the yield of the reaction requires improvement, as the gold-thiol bond is relatively strong making ligand replacement challenging.[223]

To overcome the drawbacks of the ligand exchange method, direct synthesis of Au NPs with water-soluble thiol-ligands would be beneficial. DHLA–PEG molecules were identified as promising candidates for use as surface capping agents. This ligand has been successfully used to produce stable aqueous solutions of metal NP's and quantum dots.[224] The DHLA-PEG capping ligand is composed of dihydrolipoic acid (DHLA) whose function is to anchor onto the nanoparticle surface and a PEG (polyethylene glycol) chain linked to the DHLA *via* its terminal amine (Figure 4.5). DHLA-PEG can be terminated with different functional groups (*e.g.* carboxylic acid, -OMe and amino groups) to enable further attachment of targeting molecules.

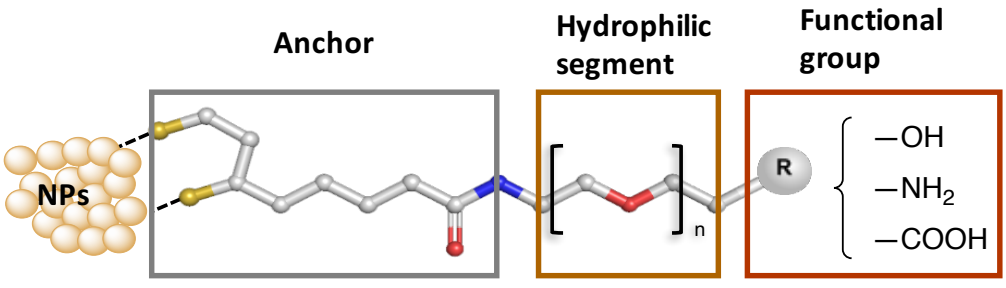

Figure 4.5 Schematic representation of a modular design of PEG-based hydrophilic ligands.

DHLA has two thiol groups which provide strong anchoring to the surface of Au NPs. Au NPs made with DHLA have been reported to be stable and biocompatible. Strong ligand binding ensures resistance to ligand exchange when Au NPs are placed in high concentrations of other thiols-containing molecules such as intracellular glutathione (GSH),[225-227] which can be present up to 125 μM for 72 hrs.

PEG is used to achieve the aqueous solubility and enhance the retention time of Au NPs by protecting them against various degrading system active inside a tissue or cell.[228] It has been demonstrated, that PEG efficiently improve the solubility, stability and dispersion of conjugated drugs, lead to an improved antitumor efficiency *in vivo* by increasing the cellular uptake of drugs by hiding the nanoparticles from immune system.[227] The surface modification of NPs with PEG of different chain length or molecular weight and incorporation of different targeting moieties is emerging as a more promising and technologically advanced drug delivery system in anti-cancer therapy.[216]

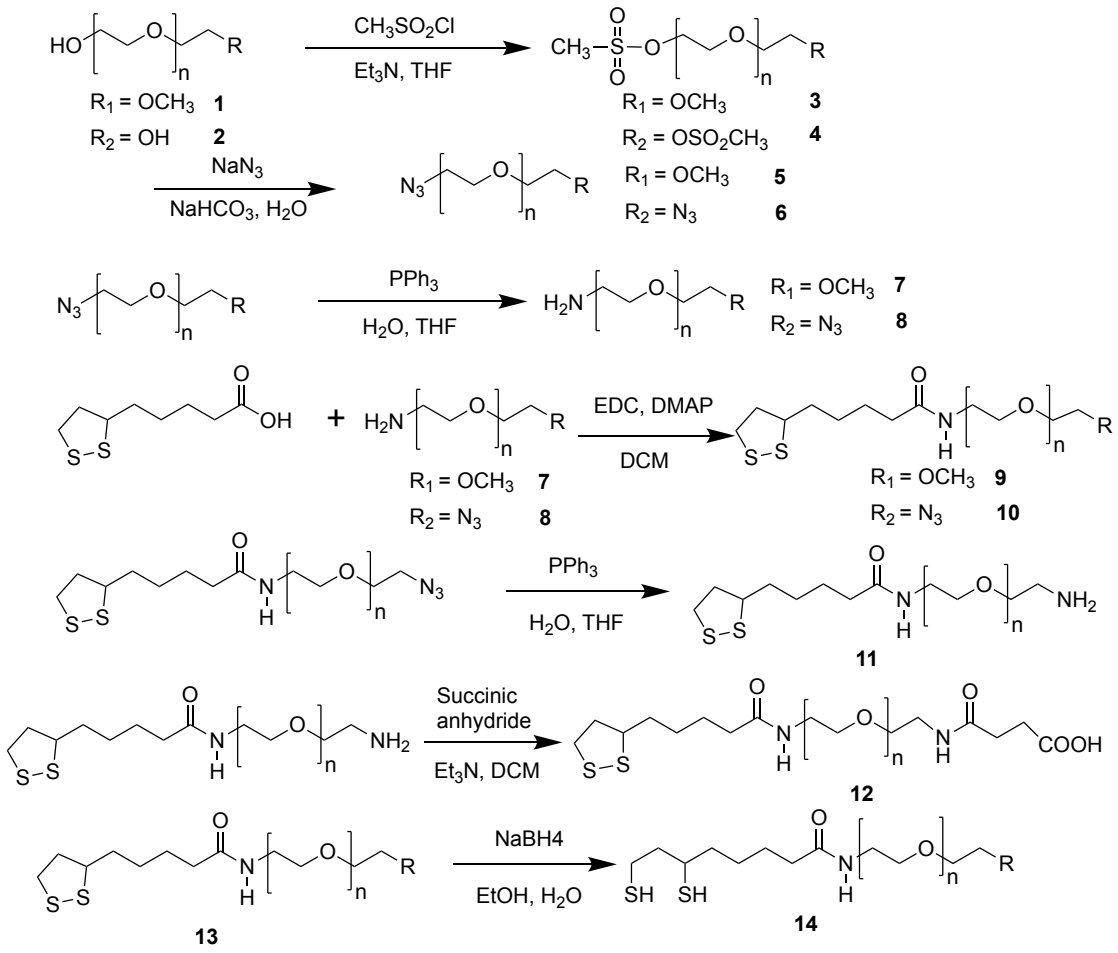

Scheme 4.1 Reaction scheme of series PEG based ligands.

Ligands that connect thioctic acid and PEG with the amide group were synthesized (Chapter 3.2.1). One-pot functional group interconversion of the alcoholic moieties into azides was used. Followed by regioselective Staudinger reaction, yielding **(7)/ (8)**. This azido-amine is coupled with TA to form **(9)/ (10)**. Staudinger reduction of **(10)** leads to **(11)**. Intermediate **(10)** can be further reacted with succinic anhydride, and yields the ligand terminated with COOH **(12)**. TA-PEG **(13)** which, upon disulfide reduction, gives the DHLA-PEG ligand (**14).** All solutions were purged by nitrogen before the final reduction step. [3] The PEG starting material can be easily changed for a different chain length from PEG200 to PEG550. All products were analyzed by TLC

and NMR.

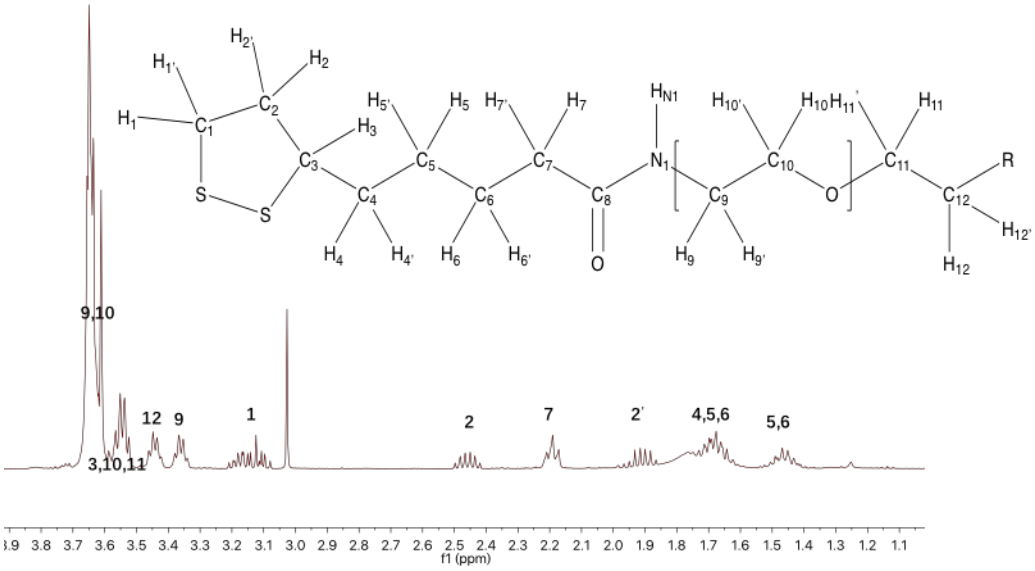

Figure 4.6 ^{1}H NMR spectrum of TA-PEG-MPEG (Inset shows a structure of thioctic acid with numbered hydrogens and carbons).

All ligands synthesized were analysed by NMR to confirm their structures. A representative ^{1}H NMR spectrum is shown in Figure 4.6 for TA-PEG-NH_2. The peaks of ^{1}H NMR are labeled with corresponding numbers of hydrogen as on the molecular structure. These studies also confirmed successful attachment of functional groups (–OCH_3, -COOH) (Figure 4.7). The presence of - OCH_3 group was confirmed by the single peak at ~ 3.4 ppm (with ♦ labelling on the first spectrum of Figure 4.8). The presence of - COOH group was confirmed by the two multiple peaks at ~2.65 ppm and ~ 2.55 ppm (labelled ✦) characteristic of two –CH_2- groups between –CONH- and –COOH. We also successfully fabricated ligands with different lengths

by adjusting the poly (ethylene glycol) molecular weight of 200, 400 and 550, supported by mass spectrometry.

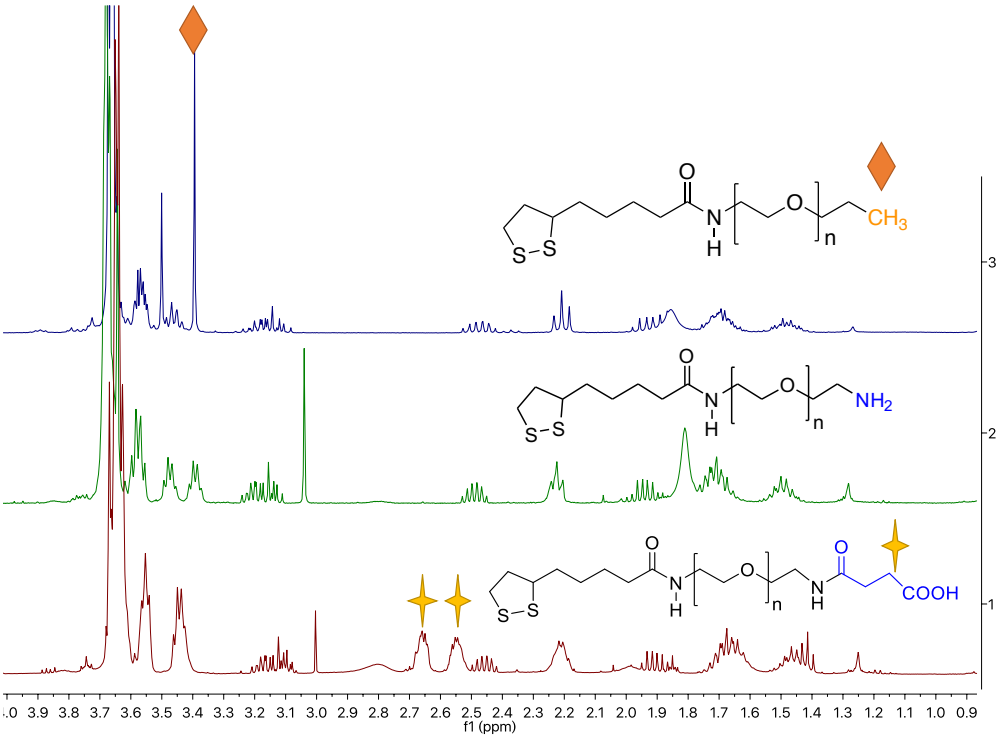

Figure 4.7 ^{1}H NMR spectra of PEG based ligands terminated with –OCH_3, -NH_2 and –COOH. (Inset show the structures of TA-PEG with corresponding functional groups).

We have successfully synthesized PEG-based ligands. All ligands were kept at 4 °C until further use, such as the synthesis of Au NCs. The -S-S- part of these ligands are ready for surface attachment of NPs at a reduced state.[17, 22, 28, 30, 54, 60-67, 69, 70, 107, 229]

4.3 PEG capped gold nanoclusters

In this part, we first presented Au NCs capped with DHLA-*O*-MPEG and with then DHLA-NH-PEG based ligands terminated with –OCH_3, -NH_2 and –COOH. The

synthesis parameters have been optimized to obtain smaller nanoclusters and properties of Au NCs capped with various ligands will be compared.

4.3.1 Au NPs capped by DHLA-*O*-mPEG

Our first water soluble Au NPs were prepared using DHLA-O-mPEG400 ligands, using the procedure described in Chapter 3.2.3.1. Briefly, chloroauric acid was used as a source of gold and was mixed with ligands under alkaline environment (pH ~ 11) in deionized water and reduced by $NaBH_4$. The ratio of gold to ligands was 1:3. Molar ratio of Au : $NaBH_4$ = 1 : 2. Following centrifugation/filtration using a Millipore unit, a concentrated brown solution was produced (Figure 4.8).

The formed colloidal solutions were found to be stable for a period of over 3 years if stored at 4 °C by UV/Vis. As shown in Figure 4.9, the Au NCs reveals an more intensified absorption profile than the ligand only solution.

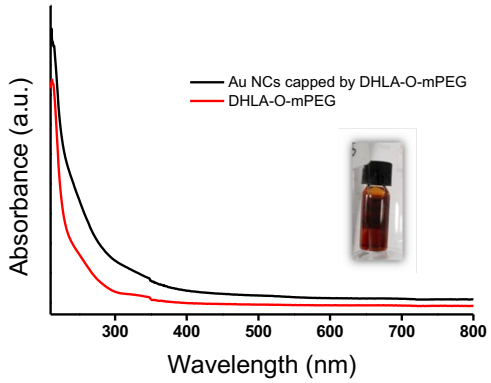

Figure 4.8 Representative UV/Vis spectra of DHLA-*O*-mPEG capped gold nanoparticles (black line) and of ligands only (red line).

As mentioned before, according to Mie theory, gold nanoparticles with $d > 3$ nm are expected to show absorption peak around 520 nm, which is not present in Au NPs with $d < 2$ nm [60, 65, 107] However, the analysis of published work (Figure 4.9) show some inconsistencies between the NP size and the position of absorption locations. [30, 33, 35, 100, 107, 216, 230-242] Some reports demonstrate that gold nanoparticles with diameter smaller than 2 nm also have higher absorption around 520 nm.[243] Hence, UV/vis is not sufficient for confident confirmation of Au NC sizes and further morphological characterization is required.

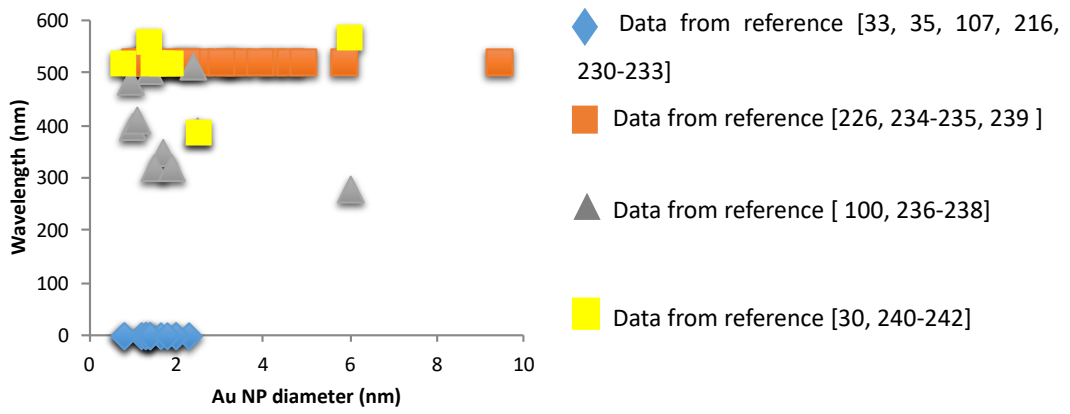

Figure 4.9 A summary of absorption peak position *v.s.* Au NP size from literature sources. Data points shown with blue diamond points are for NP where no peak was observed; Data points shown with orange squares are for NP with distinct absorption at 520 nm; Data points shown with grey triangles are for NP with peaks in the range form 280 nm to 512 nm; data points shown with yellow squares are for NP with two distinct peaks in the range of 370 nm to 570 nm.

4.3.2 Au NPs capped with TA-CONH-PEG

The TA-COOH-PEG capped Au NCs (Chapter 4.3.1) were synthesised using an ester

as the linker to connect thioctic acid and PEG. However, the stability of this ligand was low, hence the ester linker was replaced with the amide group (-CONH-). Amide shows greater stability compared to ester due to the resonance forms of the amide.

The TA-CONH-PEG capped Au NPs were synthesized following the same procedure as for DHLA-*O*-mPEG capped Au NPs (Chapter 4.3.1). The molar ratio of Au to ligands was 1: 3 and molar ratio of Au: $NaBH_4$ was 1: 2. As shown in Figure 4.10, the absorption spectrum of this Au NCs solution revealed a distinct absorption peak at 340 nm and a small peak at 520 nm. We note that ligand only solution has no distinct absorption features in this wavelength range.

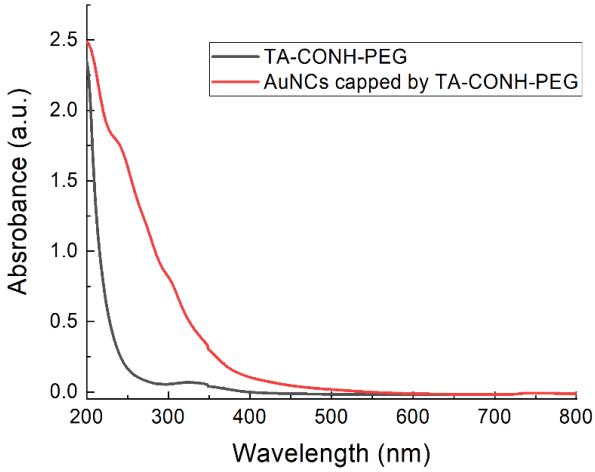

Figure 4.10 The UV/Vis spectra of solutions of TA-CONH-PEG550-OCH_3 (black) and TA-CONH-PEG550-OCH_3 capped Au NCs (red).

To optimize the method to produce ultra-small particles, the effect of several parameters on the NCs properties have been investigated: the molar ratio of gold to

ligands, stirring time and pH value of the starting solution.

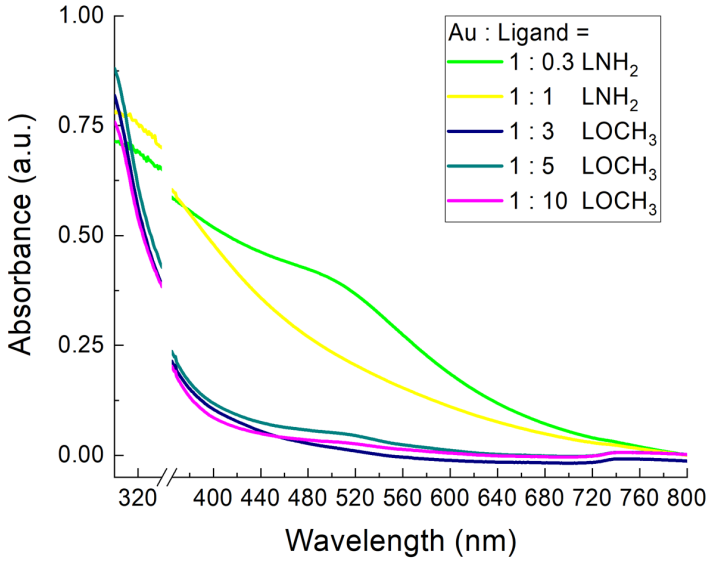

Figure 4.11 The UV/Vis spectra of Au NCs with Au: Ligand molar ratio of 1:0.3 (green, LNH_2), 1:1 (yellow, LNH_2) 1:3 (navy, $LOCH_3$), 1:5 (viridian, $LOCH_3$), 1:10 (rose, $LOCH_3$), an experimental artefact (between 340 and 365 nm) was intentionally deleted.

Au: Ligands ratio ranging from 1:0.3 to 1:10 were explored. It is expected that the greater ratio of ligands will provide more efficient surface passivation, leading to formation of smaller Au NP. The UV/Vis absorption spectra of Au NCs produced with different amounts of capping molecules are shown in the Figure 4.11. The absorption profile of the nanoparticles produced with 1 : 0.3 ratio of Au to ligand showed resonance peak at ~ 520 nm, indicating formation of larger particles (d > 3 nm). Although, all other ratios had no distinct absorption, the 1:1 ratio revealed greater

absorption of $\lambda > 300$ nm compared to other samples. No significant absorption in this range was observed for solutions produced with 1:3, 1:5 and 1:10 ratio samples. The ratio of Au : ligands = 1:3 was chosen for further studies as NPs formed had $d < 2$ nm and the colloidal solutions had long shelf life (> 6 months).

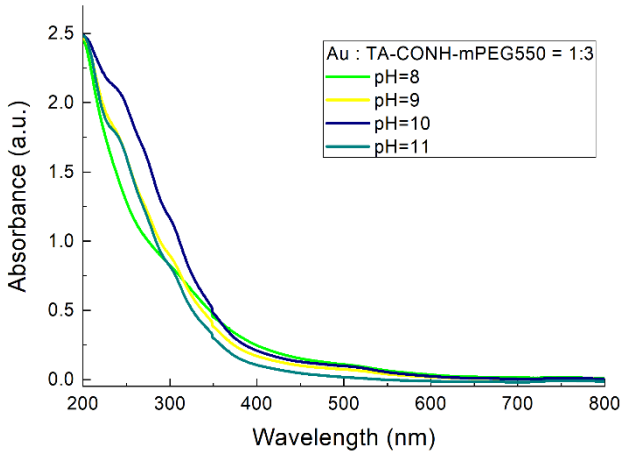

Figure 4.12 The UV/Vis spectra of TA-CONH-mPEG550 capped Au NCs synthesized at pH of 8 (black), 9 (bright green), 10 (yellow) and 11 (dark green).

The effect of the pH of the Au-precursor solution on Au NCs size was considered. The pH was adjusted by adding 2M NaOH before addition of tetrachloroauric acid. The pH is a crucial parameter for the synthesis of polymers capping metal nanoparticles. Since the morphology and size of the nanoparticles could be controlled by changing the pH of the media.[244] The UV/Vis absorption spectra of samples synthesized at pH = 8, 9, 10, show a distinct absorption around 520 nm, compared with samples synthesized at pH 11 (Figure 4.12), indicating that smaller NCs were formed at this pH.

We envisaged that an increased pH leading to improvement of the reduction rate of gold ions and accelerated reduction is suggested as a key step to obtain smaller particles, stable against aggregation.[216]

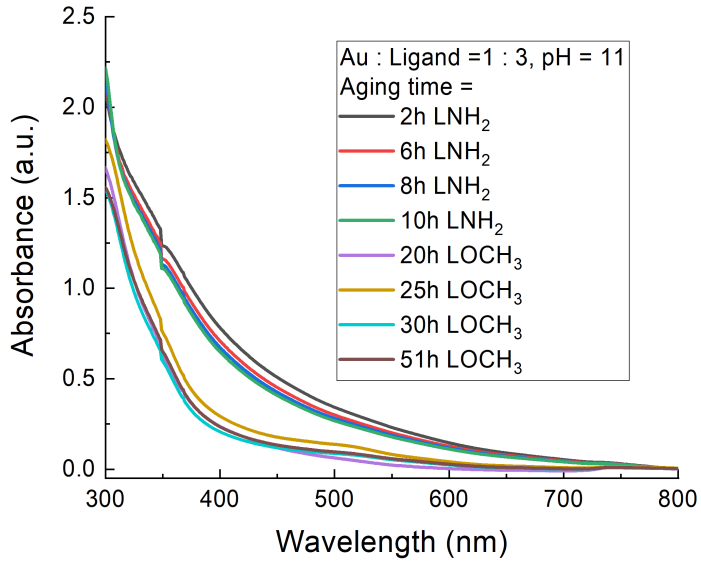

Figure 4.13 Representative UV/Vis spectra of LNH_2 or $LOCH_3$ capped Au NCs synthesized at pH = 11 with different aging time from 2 h to 51 h.

The reaction time affects the nanoparticle size. Syntheses were performed with different reaction ageing times from 2 h to 51 h at room temperature. The UV-Vis spectra (Figure 4.13) of the NPs produced with t_{Aging} = 20 hrs revealed no absorption band at 520 nm, while samples prepared with longer ageing times revealed absorption peak at 520 nm, and those produced at shorter aging times revealed stronger absorption at λ > 300 nm. These results indicate that longer ageing time of the reaction leads to growth of larger particles and shorter ageing time may result in incomplete reaction.

Hence, we selected t_{Aging}= 20 hrs for further synthesis.

Informed by these studies, we summarized the optimized synthesis parameters: the molar ratios of gold and ligands = 1:3; stirring time t_{Aging} = 20 hrs; and pH value of the starting solution at 11. These conditions are used in further experiments.

4.3.4 Au NCs capped with different PEG-based ligands

The benefit of -NH_2 terminated capping ligands is its properties of modification. Au NPs are easily modified to attach to molecules for further biological applications. With the optimized parameters of Au NCs synthesis: pH 11, Au : Ligand = 1:3 and aging time 20 h, DHLA-NH-PEG400-NH_2 capped Au NCs dispersions were produced in aqueous solutions (see Chapter 3.2.3 for experimental details).

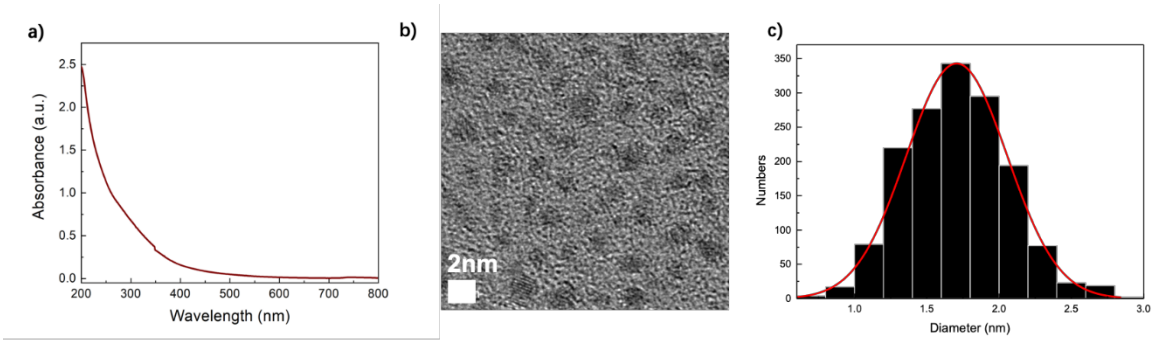

Figure 4.14 (a) A representative UV/Vis spectrum and for DHLA-NH-PEG400-NH_2 stabilized Au NCs. **(b)** High-resolution TEM image and **(c)** histogram of size distributions of NCs.

In the absorption profile of these Au NCs (Figure 4.14a) no absorption peak was detected around 520 nm, as expected for d < 2 nm. The size of NCs was confirmed by

HRTEM. To assess the morphology, the Au NCs were deposited on graphene oxide coated copper grid. Images were acquired on JEOL-2100F microscope operated by Dr M. Fay (nmRC Nottingham). Figure 4.14b shows a typical HR-TEM image. From the analysis of TEM images, it was found that gold nanoparticles are spherical in shape and have an average diameter of 1.7 ± 0.4 nm.

The length of the capping ligands may have effects on the density of surface coverage. According to Hinterwirth *et al.,*[216] ligand density linearly increases with decreasing ligand length. This may affect the particle size and their colloidal stability. Longer ligands may lead to low surface coverage, which may cause aggregation and precipitation.

To explore the effect of PEG length, PEG was used with molecular weight of 200, 400 and 550. The length of this molecule is estimated to be 1.97 nm, 3.16 nm and 4.05 nm, separately by estimated in *Materials Studios for a stretched molecule*.

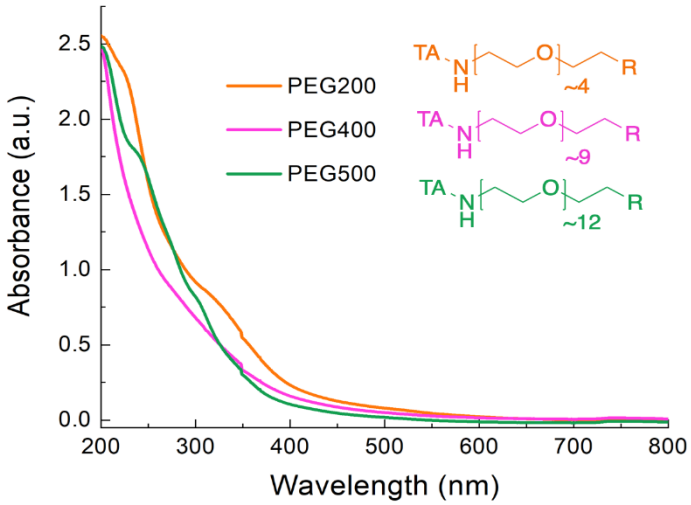

Figure 4.15 UV-Vis absorption spectra of Au NCs capped with PEG-based ligands with PEG molecular weight of 200, 400 and 550. Inset show a chemical structure of the ligands.

No absorption peak was recorded at ~520 nm for these Au NCs solution, indicating that the diameter of these particles was smaller than 2 nm. We conclude that all capping ligand used, PEG 200 to 550, can be used to produce sub 2 nm Au NCs, meeting the projects requirements.

To investigate the impact of the terminating groups, PEG-based ligands with LCOOH, LNH_2, $LOCH_3$, and LN_3 were used to stabilize Au NCs, produced with the following synthesis parameters: the molar ratios of gold to ligands = 1:3; aging time 20 hrs; and pH = 11 for the starting solution.

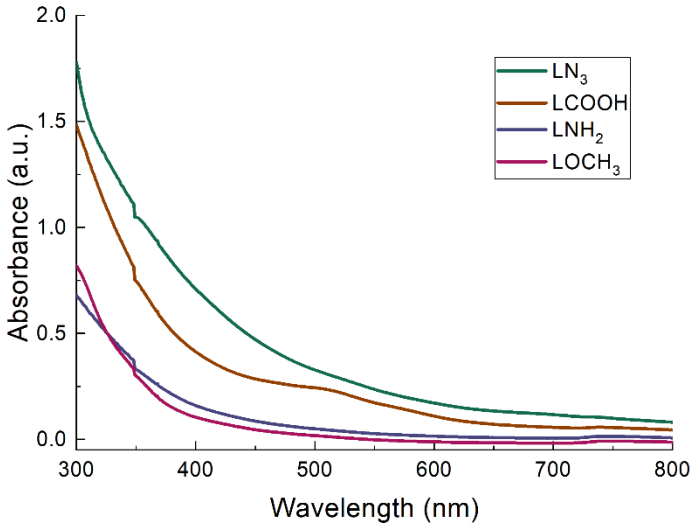

Figure 4.16 UV-Vis absorption spectra of Au NCs capped with PEG-based ligands with PEG ended with –COOH (red), -NH_2(blue), -OCH_3(green), and -N_3(black).

It is apparent that solutions of Au NCs capped with the same concentration of LNH_2 and $LOCH_3$ have weaker absorption around 520 nm, indicating a smaller size of Au NCs compared to LN_3 and LCOOH. We envisaged that the pH of the reaction affects the size of the Au NCs capped by ligands with different terminal functional groups. However, further research is needed for a deeper understanding of the relationship. Also, azide will be converted to $–NH_2$ with the addition of strong reducing agent $NaBH_4$.[245] Hence LN_3 were not used in further work.

We also explored a possibility to produce NCs with mixed ligands, combining LCOOH with $LOCH_3$ or LNH_2 with $LOCH_3$. The molar ratio of inert $LOCH_3$ to reactive LNH_2 (or LCOOH) 1:0, 0.7:0.3, 0.3:0.7 and 0:1 was used. The UV/Vis spectra are shown in Figure 4.17. Consistent with above results (Figure 4.16), no distinct absorption peak

was observed for NCs capped with mixture of LNH_2 and $LOCH_3$. A small peak at ~ 520 nm is resolved for samples containing LCOOH.

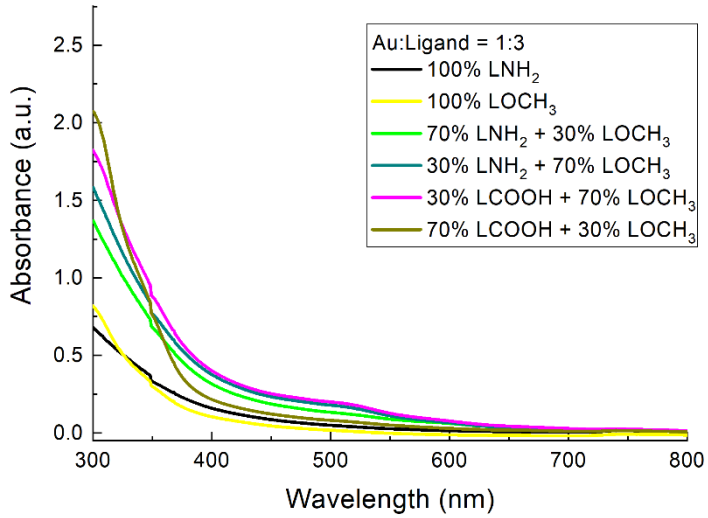

Figure 4.17 The UV/Vis spectra of Au NCs synthesized with different Ligands ratios.

During NC synthesis, the TA-PEG ligand is reduced to DHLA-PEG. We compared Au NCs synthesized with TA-PEG and DHLA-PEG. Both samples showed flat absorption at ~ 520 nm (Figure 4.18), indicating similar size Au NCs were obtained with both disulfide and dithiol ligands. Hence, there is no need to reduce TA to DHLA before the synthesis. The absorption feature in Au NCs dispersions UV/Vis spectrum could be from unreacted tetrachoroauric acid: a pronounced peak at 290 nm was reported for pure aurate solution.[116]

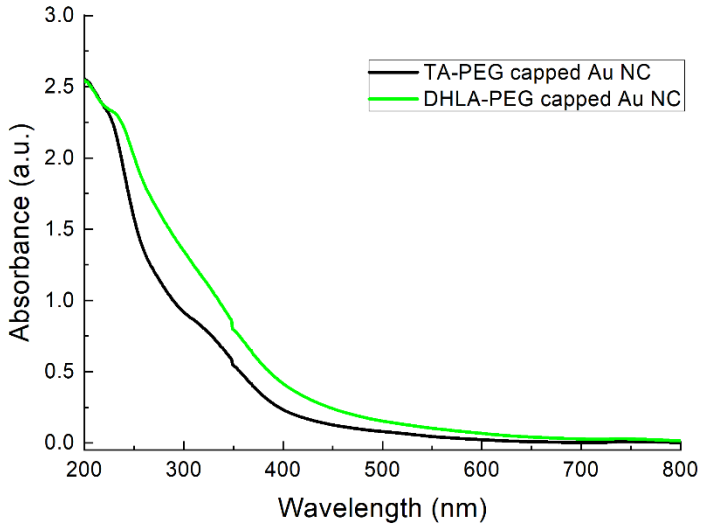

Figure 4.18 The UV/Vis spectra of Au NCs capped with TA-NH-PEG400-NH_2 (black) and DHLA-NH-PEG200-NH_2 (green).

4.3.5 Study of the stability of Au NC solutions

The stability of Au NCs in different environments has significant implications for their future use. As a result, the effects of temperature and pH on colloidal stability and optical properties was studied.

The stability of TA-PEG400-NH_2 /TA- MPEG550 capped Au NCs was assessed over a period of 1 month, at different pH (pH = 6 - 9) and at physiological temperature (T = 37 °C). The UV/Vis characterization was carried out after storing at 4 °C for 1 month; heating a sample of TA-NH-PEG400-NH_2 and TA-NH-mPEG550 capped Au NCs to T = 40 °C using water bath for 1 h, adjusting pH of the aqueous solution from slightly basic pH = 9 to neutral pH = 7 then to slightly acidic pH = 6.

For both Au NC solutions studied, the UV/Vis spectra (Figure 4.19) did not reveal any significant changes, indicating that pH in the range from 6 to 9 did not affect the stability of the solutions. The thermal treatment has not caused any significant changes to optic properties, only slightly weaker absorption was observed. No precipitation was observed over 1 month storage, hence stability of colloidal solutions was not affected.

It can be concluded that TA-NH-PEG400-NH_2 capped Au NCs and TA-NH-mPEG550-capped Au NCs are stable at physiologically relevant pH and temperature.

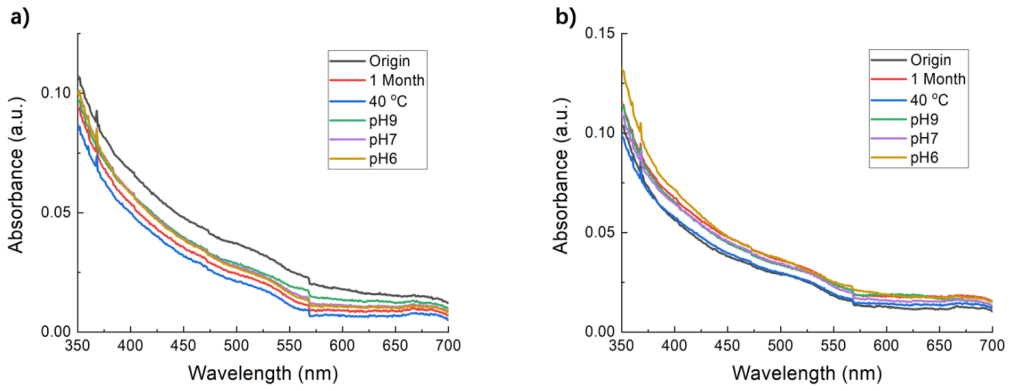

Figure 4.19 The UV/Vis spectra of Au NC aqueous solutions exposed to different conditions: original (black), 1 month old (red), 40°C of original (blue), pH = 9 (yellow), 7 (pink), 6 (brown) of original. **(a)** TA-NH-PEG400-NH_2 capped Au NCs; **(b)** TA-NH-mPEG550 capped Au NCs.

Long-term stability study is required for long shelf life of the product. The long-term stability of Au NCs was examined by UV/Vis absorption on freshly prepared DHLA-NH-PEG200-NH_2 capped nanocluster solutions, after one month and after six months

of storage at 4 °C (Figure 4.20). The solutions remained aggregate-free and no significant changes were observed, indicating that the nanoparticles retain their shape/size and capping layer over the period of at least 6 months. This indicates that binding of thiol group in capping ligand to gold atoms on NCs surface is sufficiently strong and provides efficient passivation of the surface, reducing the rate of Ostwald ripening and preventing aggregation.

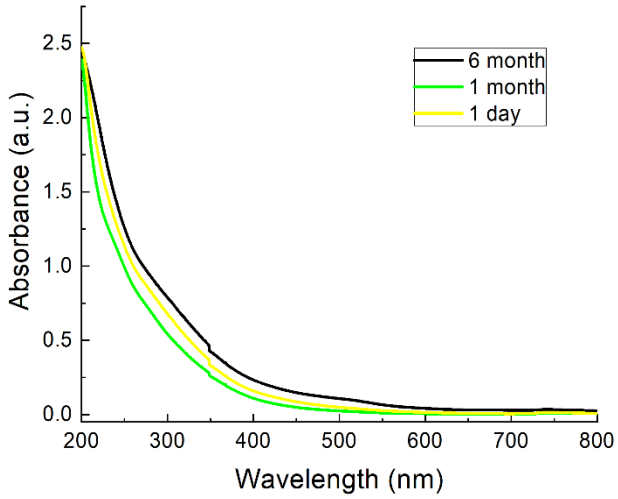

Figure 4.20 The UV/Vis spectra of DHLA-NH-PEG200-NH_2 capped Au NCs, as-synthesized (original, yellow), and stored for 1 month (green) and 6 months (black) at 4 °C.

The pH and temperature stability study of TA-NH-PEG200-NH_2/ DHLA-NH-PEG200-NH_2 capped Au NCs was also studied. The pH of the Au NCs dispersions was adjusted by adding 0.5 M NaOH, and 0.5 M HCl solution and stored for 24 h at 4 °C. The stability of Au NCs against changing pH and temperature was probed in the

range of pH = 3 - 11 and T = 40 °C and 50 °C for 1 hr. No noticeable change was observed at the range of temperature and pH's studied.

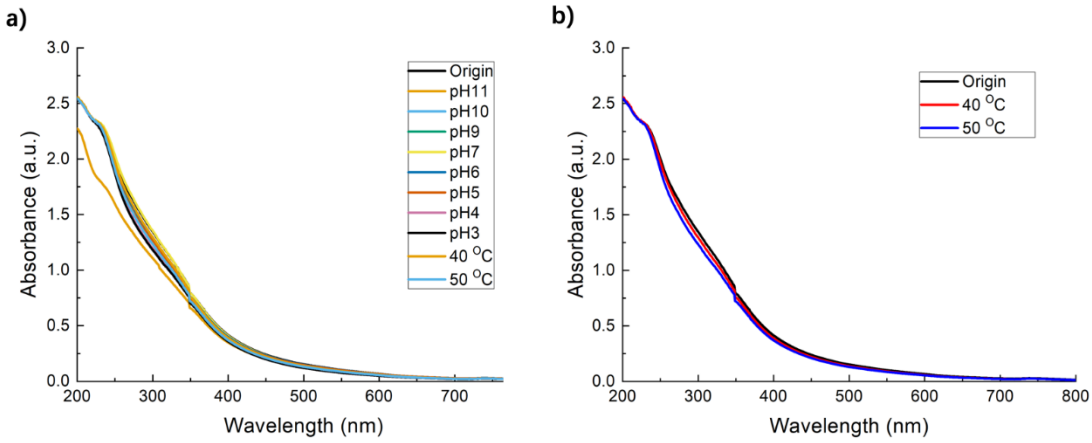

Figure 4.21 The UV/Vis spectra of DHLA-NH-PEG200-NH_2 capped Au NCs solutions exposed to **(a)** different pH and **(b)** treated for 1 h at different temperatures.

These results confirm that Au NCs capped with PEG-modified dihydrolipoic acid demonstrate remarkable colloidal stability over a broad pH and temperature range.

The stability of Au NC dispersions capped by TA-NH-PEG200-NH_2 is similar to DHLA-NH-PEG200-NH_2. The pH and thermal treatment has not affected the UV/Vis absorption profiles.

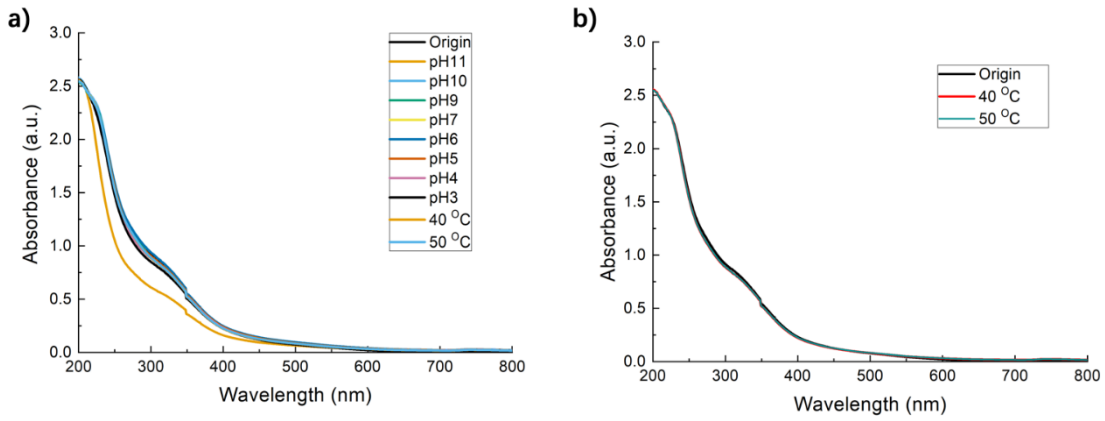

Figure 4.22 The UV/Vis spectra of TA-NH-PEG200-NH_2 capped Au NCs solutions exposed to **(a)** different pH and **(b)** treated for 1 h at different temperatures.

Small changes are observed for both samples at pH = 11. It is well documented that thiol ligands are the best candidate to maintain the stability of gold nanoparticles.[117, 120, 246] However, the stability of nanomaterials in aqueous solution also depends on the surface charge or the ligands structure. At pH 11, NH_2 terminated PEG ligands are expected to be less protonated (pka of amines: ~10.7) and affect the Au NCs overall absorption.

The results on synthesis of Au NCs capped by PEG-modified lipoic acid ligands, as bidentate anchoring groups, clearly demonstrate remarkable colloidal stability over a broad pH and temperature ranges, and long-term stability. Strong coordination of the anchoring group onto the metal surface combined with the inert nature of the PEG makes these materials very promising for applications both in life sciences and electronics.

4.3.6 Magnetic properties of Au NCs

4.3.6.1 Magnetic properties studied by SQUID

Bulk gold is diamagnetic, [113] but ligated gold nanoclusters have been reported to demonstrate magnetism in previous research.[247] The reasons are not yet fully understood, however several reasons have been suggested for the explanations of magnetism in NPs: 1) Their molecular-like structure. Jin *et al.*[248] proposed the reason that the magnetism arises from an unpaired spin having distinct P-like character and delocalized among the gold core in the HOMO both by DFT calculations and experiments. 2) The electron orbitals at the interaction of ligands and gold core, the spin-orbit coupling between surface-bound thiols and gold surface atoms. Which proposed by Hernandes *et.al.*,[249, 250] as the gold particle size decreases and surface area to volume ratio increases, the likelihood of ferromagnetism increases. The magnetization data of water-soluble PEG capped Au NCs (1.7 nm) and organic-soluble Au NCs (2.2 nm) were probed using a superconducting quantum interference device (SQUID) magnetometer at a temperature range from 2 to 50 K.

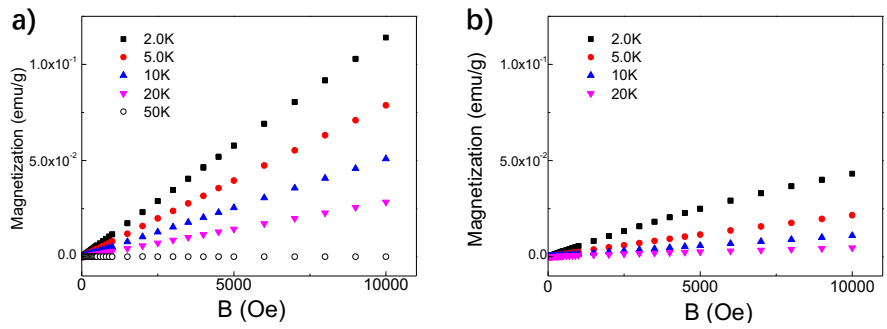

Figure 4.23 Magnetization of Au NCs with average diameter of (a) 1.7 nm (water-soluble) and (b) 2.2 nm (organic-soluble).Measurements were performed by Dr. F. Moro.

Figure 4.23 shows dependence of magnetization on magnetic field strength for Au NCs samples at temperatures of 2 K, 5 K, 10 K, 20 K and 50 K. Both samples exhibit a typical paramagnetic behavior below 50 K. With an increasing magnetic field, the paramagnetic response rises linearly. The magnetic susceptibility is an indicator for the paramagnetic strength of materials and can be estimated from the slope of the magnetic hysteresis (MH) curves (results are listed in Table 4.1). It is apparent that water-soluble Au NCs have larger susceptibility values compared to the organic-soluble NCs. Moreover, the magnetic properties of both Au NCs studied are temperature dependent: the lower the temperature, the stronger the paramagnetic property.

Table 4.1 Magnetic susceptibility of Au NCs at different temperatures.

Temperatures (K)	Susceptibility (1 × 10^{-6} emu/gOe)	
	1.7 nm Au NCs	2.2 nm Au NCs
2	7.16/11.45	5.33/4.52
5	3.51/7.89	2.34/2.19
10	1.96/5.10	1.20/1.11
20	1.05/2.85	0.55/0.47
50	0.44/-	0.15/-
300	6.69 × 10^{-2} /-	- 0.0191/-

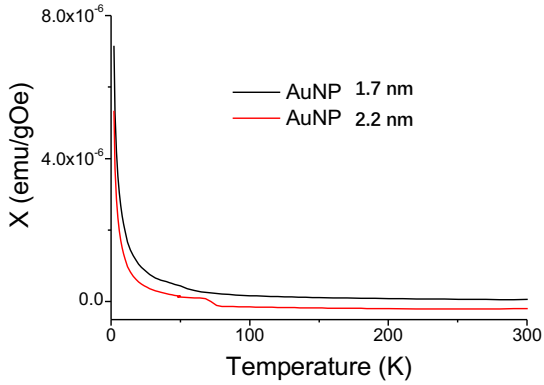

Figure 4.24 Temperature dependence of magnetization susceptibility for 1.7 nm Au NCs and 2.2 nm Au NPs.

Our magnetic studies using Superconducting Quantum Interference Device (SQUID) of the AuNPs with sizes 1.7 nm and 2.2 nm show that at low temperatures (T < 50 K) the nanoparticles are paramagnetic and the smaller NCs possess magnetic susceptibly which gradually decrease from 2 K (7.16 x 10^{-6} emu/gOe v.s. 5.33 x 10^{-6} emu/gOe) to 50 K (0.44 x 10^{-6} emu/gOe v.s. 0.15 x10^{-6} emu/gOe)(see Figure 4.24 and Table 4.1). For AuNCs with diameter of 1.7 nm the paramagnetic properties are observable up to room temperature(6.69 x 10^{-8} emu/gOe at T = 300 K).

However, the magnetic susceptibility values of dodecanethiol capped Au NCs changes from positive to negative values at temperature T = 70 K, indicating that larger gold nanoclusters are diamagnetic at higher temperature.

It is anticipated that all our PEG-capped water-soluble NPs with d = 1.7 nm are paramagnetic. SQUID is a very sensitive technique which may also include signal from ligands that effects the results. Also, for used in biomedical applications, Au NCs should be paramagnetic at room temperature. Hence, further studies are needed to probe this effect.

4.3.6.2 Magnetic properties studied by ^{1}H NMR

NMR spectroscopy offers a sensitive tool to assess magnetism in NPs, by measuring relaxation times of protons located near a magnetic centre. ^{1}H and ^{13}C, spectra were obtained using a Bruker Avance 500 spectrometer at 500 MHz and at 125.7 MHz, respectively. T_1 and T_2 relaxation time were measured with inversion recovery pulse

sequence and CPMG pulse sequence from ^{1}H NMR performed on a 600 MHz spectrometer at a repetition rate of 1 s. All spectra were acquired at 298K and referenced to tetramethylsilane (TMS) for an external standard.

Theoretically,[251] when a spin label is located close to a proton, magnetic dipole interactions lead to paramagnetic relaxation enhancement (PRE), increasing the relaxation rate of the nuclear magnetization and resulting in the suppression of the NMR signal of the neighbouring nucleus. The line-width of observed NMR proton signal is significantly perturbed. The paramagnetic enhancement is expected to decrease with increasing distance between spin label and the proton studied. Relaxation rates were studied on our Au NCs to access their magnetic properties. A typical ^{1}H-NMR spectrum measured on the synthesized DHLA-PEG-NH_2 capped Au NCs and DHLA-PEG-NH_2 alone are shown in Figure 4.25.

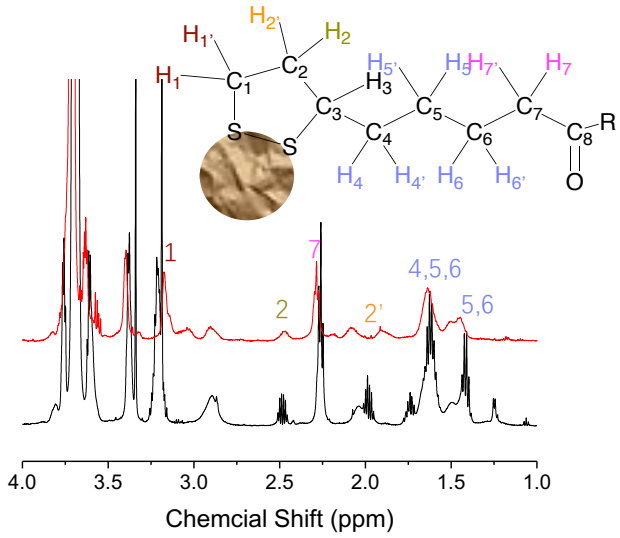

Figure 4.25 Representative ^{1}H NMR spectra of DHLA-PEG400-NH_2 (black) and DHLA-PEG-NH_2 capped Au NCs (red) recorded at room temperature. All samples were prepared in solvent consisting of 90% H_2O + 10% D_2O (Inset shows a structure of thioctic acid attached to gold core with numbered hydrogens and carbons).

The ^{1}H NMR spectra of DHLA-PEG400-NH_2 capped Au NCs and DHLA-PEG400-NH_2 samples were compared. To determine the peaks of protons in ligand molecules close to the Au NCs surface, a complete assignment of all observable NMR resonances was carried out by combining 1D ^{1}H, ^{13}C NMR spectra, 2D-COSY, and 2D-HSQC techniques. The corresponding protons are numbered in a proximity sequence to gold core on the DHLA molecular structure and labelled on ^{1}H NMR spectra in Figure 4.27.

It is evident that the intensity of NMR signals closets to the gold surface are lower and resonances are broader compared to ligand only peaks. The signal broadening suggests

the presence of paramagnetic compound in the proximity to corresponding protons. Hence, these results support our previous results, suggesting presence of paramagnetic gold core.

As expected, longitudinal relaxation time, T_1, of protons in the vicinity of paramagnetic Au NCs samples is expected to be shorter compared to ligand only solutions. Table 4.2 summarises all the observed T_1 values.

Table 4.2 Longitude relaxation time T_1 (unit: second) for Au NCs and Ligands

Position	***AuNP***	***Ligands***
1	1.207	1.889
2	0.66	1.614
2'	0.5869	0.993
4,5,6	0.467	0.704
5,6	0.525	0.76
7	0.615	0.667

We observe a clear trend in value of T_1 depending on a distance between proton and NCs surface: the T_1 difference decreased with increasing distance to the gold core (Figure 4.26).

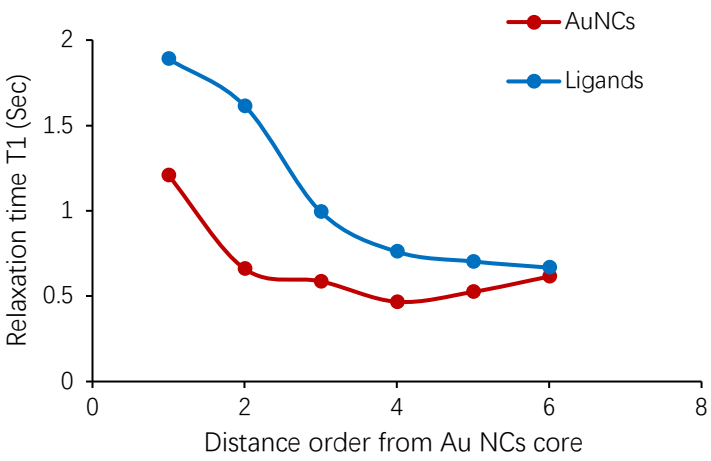

Figure 4.26 Dependence of T_1 time on distance between protons on ligands and Au NC surface, for NC solutions(red) and ligands only solution.

4.4 Conclusions

A range of Au NCs with different capping ligands was successfully synthesized. Au NCs capped by dodecantheiol are soluble in *iso*-propane and have homogeneous size distribution of 2.2 ± 0.4 nm. By changing the ligands used, water-soluble gold nanoclusters capped by PEG-based ligands with average diameter of 1.7 ± 0.4 nm were also synthesized. Optimized parameters for Au NCs synthesis were obtained: Au: Ligands ratios = 1: 3, reaction pH = 11, aging time 20 hrs. The aqueous Au NCs produced exhibited long-term colloidal stability over a wide range of pH (3-10) and

temperatures (T = 40 °C and 50 °C). Both organic-soluble and water-soluble gold nanoclusters demonstrated paramagnetism at temperature lower than 50 K. However, PEG-based Au NCs had a stronger paramagnetism which was further verified by a shorter relaxation times, T_1, observed for protons on capping ligands in Au NC samples estimated from ^{1}H NMR studies.

Chapter 5

Au NCs conjugated with folic acid

Folic acid (FA) is a natural vitamin B9 that has been shown to be an effective ligand for targeted cancer therapies.[252] FA binds to a tumor-associated antigen known as a folate receptor (FR), of which there are four glycol-polypeptide types: FRα, FRβ, FRγ, FRδ, with a range of molecular weights from 38 to 45 kDa.[253-256] The alpha isoform, FRα, known as FOLR 1, is a glycosylphosphatidylinositol (GPI) – an anchored membrane protein with a high affinity (dissociate coefficient $k_d = 10^{-9}$) for binding and coordinating transport of the active form of folic acid.[257] It was demonstrated that folic acid can act as a drug delivery vector if an active pharmaceutical can be attached to it, without disrupting *in vivo* recognition. Recently, folic acid modified pharmaceutical agents have been proved to have a better attachment to FR positive cell line than FR negative cells in several cases.[258]

5.1 Folic acid conjugated with PEG ligands

In Chapter 4, we demonstrated the synthesis of paramagnetic and water-soluble Au NCs with long term colloidal stability. Two strategies are proposed below to conjugate folic acid with the gold nanoclusters: 1) Conjugation of thiol modified-FA on the surface of PEG-capped Au NCs; 2) Coupling folic acid with TA-PEG ligands prior to synthesis of the nanoclusters.

The yielding of first strategy may be scarified by extra post treatment steps in addition to synthesis. Therefore, we chose to attach FA to our previous ligand obtained first. As shown in Figure 5.1, folic acid has two carboxylic acid groups in α and γ positions,

In 1991, Leamon *et al.*[259] published reports of numerous chemotherapeutic agents targeted by FA, and suggested that modification of the α– carboxylic acid groups disrupts FR binding recognition, whereas, conjugation to γ– carboxylic acid has no disrupting effects. The pKa values of folic acid are 4.7(α–COOH), 6.9 (γ–COOH).

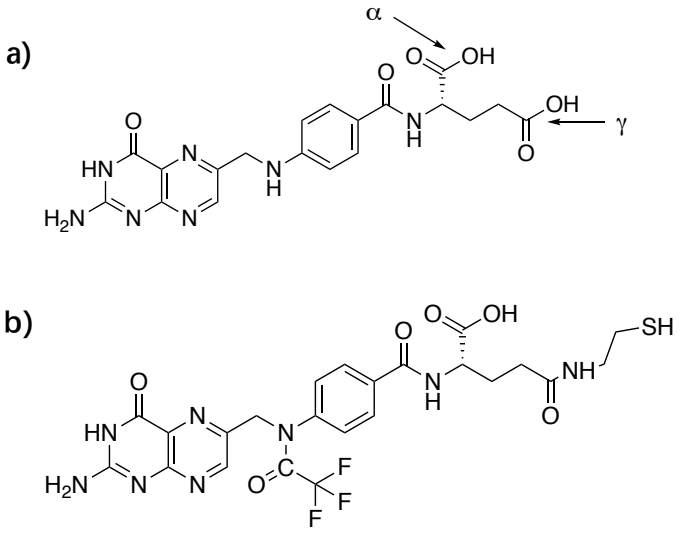

Figure 5.1 a) Chemical structure of Folic acid with α– and γ– carboxylic acid groups indicated. **b)** Structure of folic acid- γ- SH with TFA ester modified (unpublished work).

We were aiming to synthesise folic acid conjugated PEG-based ligands at the γ– carboxylic acid position. Mixture of two regioisomers, α– FA-PEG and γ– FA-PEG are potentially products obtained from direct synthesis of connecting folic acid and PEG-NH_2 *via* coupling methods, which will likely lower the targeting efficiency of cancer cells.

Water-soluble trifluoroacetic acid (TFA) modified FA- γ- SH (shown in Figure 5.1b) was provided by collaborators in Italy (Mr. Salvatore Pacifico, University of Ferrara). Once PEG-maleimide is obtained, conjugation of FA and PEG is carried out by Michael addition reaction. Reactions between thiols and maleimide have long been recognized as the most efficient Michael-type additions.[164] Given its reliability, efficiency, and selectivity, thiol-maleimide reactions have been a primary means of bio-conjugation for several decades.[64]

5.1.1 Synthesis of PEG-NH-maleimide

The synthetic route used to produce PEG-NH-maleimide is shown in Figure 5.2. First,

Mitusnobu reaction was carried out between 3-bromo-1-propanol and maleimide in the presence of triphenylphosphine and diisopropyl azodicarboxylate (DIAD). The bromine was then replaced by the amine group on PEG ligands by an S_N2 reaction.

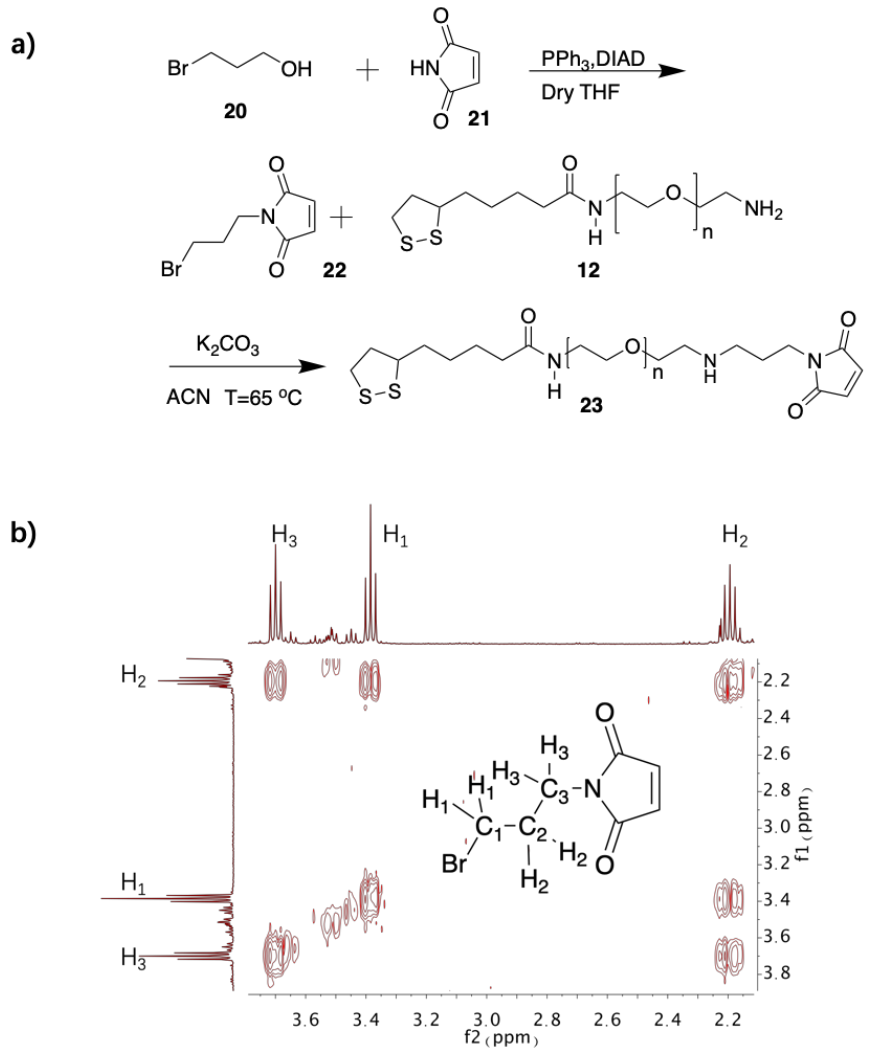

Figure 5.2 a) Scheme of PEG-NH_2-maleimide synthesis and **b)** COSY NMR of compound **(22)** (Inset shows the structure of compound **(22)** with numbered hydrogens and carbons).

COSY NMR was used to assess the success of the reaction. Protons peaks were confirmed and assigned (Figure 5.2). The COSY NMR results were inconclusive and successful synthesis of compound **(22)** was not confirmed by mass-spectroscopy as isotopic bromine peaks were absent. We opted to carry on the procedure by reacting compound **(22)** with the primary amine group on PEG ligands, to see if compound **(23)**

could be generated. Unfortunately, neither the NMR or MS indicated successful formation of compound **(23)**. Two possible reasons for reaction failure are: (i) compound **(22)** was not obtained. (ii) the last step of the procedure is more plausible for secondary amine, not for primary one. This method was discarded.

5.1.2 Synthesis of PEG-COOH-maleimide

An alternative synthetic route had been planned using carboxylic acid terminated ligands (Scheme 5.1). PEG-COOH **(12)** was coupled with NH_2-maleimide **(25)**. (see also Chapter 3.2.2). Compound **(25)** was successfully attained in a yield of ~ 25%. Compound **(26)** was produced by removal of *tert*-butyloxycarbonyl protecting group (Boc) and the free amino was used for the synthesis of compound **(27)**.

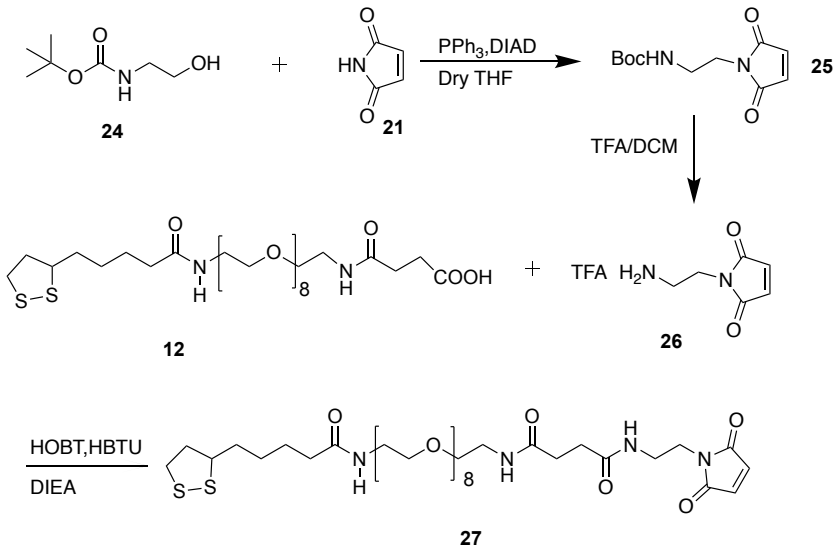

Scheme 5.1 Reaction sequences of PEG-COOH-maleimide synthesis.

The coupling reaction between PEG-COOH and NH_2-maleimide was then carried out using EDC as the amide coupling reagents in the presence of DMAP, but this failed to

produce the desired compound. Then HoBT, HBTU, DIEA were used as coupling agents in a trial reaction between thioctic acid (TA) and compound **(26)**. After TA-maleimide was obtained in this way, the procedure was then repeated between TA-PEG-COOH **(12)** and compound **(26).** The scale-up reaction successfully formed PEG-COOH-maleimide **(27)** in a good yield of ~ 64 %.

5.1.3 Michael addition of FA-SH (TFA-ester) to maleimide

To produce FA-PEG-TA ligands, a one step Michael thiol addition reaction of FA-SH with maleimide-PEG-TA was used (Scheme 5.2, see also Chapter 3.2.2 for details). No FA-conjugated product was visible in MS or NMR in the first experiment. Due to limited quantity of FA-SH, HPLC was used purify the reaction mixtures, however, no trace of desired structure was detected by MS in all 20 fractions analysed.

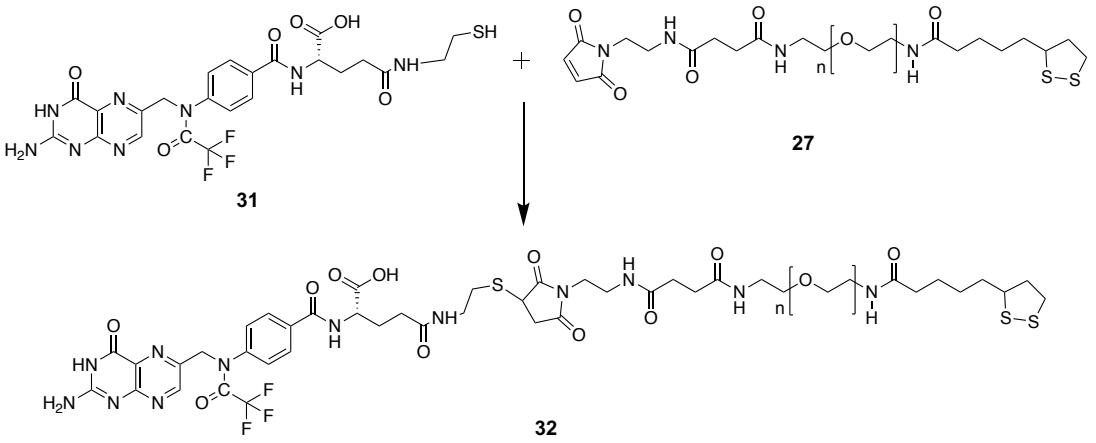

Scheme 5.2 Michael addition of FA-SH to TA-PEG-maleimide.

The reaction conditions had to be optimized for producing the desired product. So, a trial experiment was carried out: cystamine conjugating to PEG-maleimide with the same parameters that would be used for FA-SH adding to PEG-maleimdie. It was proved that maleimide was successfully attached to cystamine by MS (at 406.12 $^{1+}$m/z, the exact mass is 405.12).

5.1.3.1 Synthesis of FA-SH

In order to synthesize FA-SH, we had to consider the limited quantity of FA-SH provided by our collaborators (Mr. Salvatore Pacifico, University of Ferrara) and how to successfully attach our PEG-maleimide to it by the thiol addition reaction. The synthesis route is shown in Scheme 5.3. We activated the -COOH as NHS-ester first, then added cystamine (see also Chapter 3.2.2 for details).

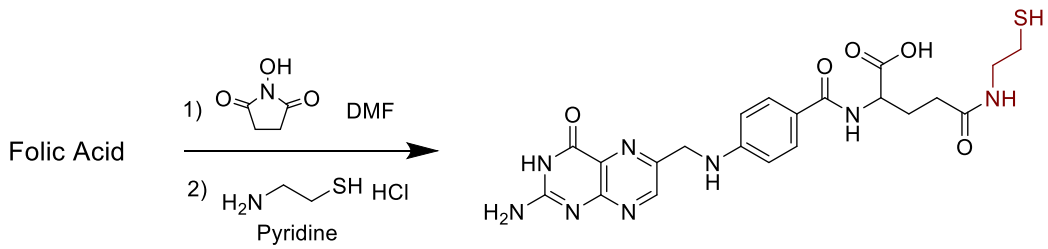

(28)

Scheme 5.3 Scheme of synthesis of FA-SH (**28**).

The conjugated structure of folic acid with cystamine was confirmed by NMR (detailed ^{1}H NMR are listed in Chapter 3.2.2.3) and MS (peak at 501.16 $^{1+}$m/z, the exact mass is 500.16). The type of regioisomer (α– or γ–) would be probed in later chapter.

5.1.3.2 Michael addition of FA-SH to maleimide

Compound (**28**) was used in a thiol Michael addition reaction with FA-cystamine and TA-PEG-maleimide, FA-PEG-TA was identified via MS. However, as shown in the MS spectrum (Figure 5.3), the PEG starting materials is still present in the reaction mixture, indicating an incomplete reaction.

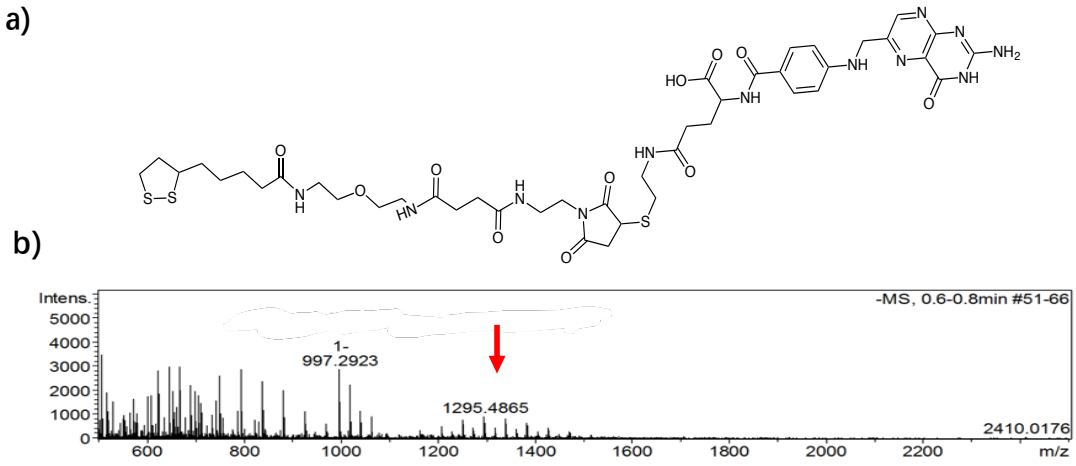

Figure 5.3 a) Chemical structure and **b)** mass spectrum of FA-PEG-TA. Arrow indicating the desired peaks.

5.2 Synthesis of TA-PEG-FA

FA-PEG-TA was synthesized in Chapter 5.1 by conjugating the modified folic acid and maleimide attached PEG using thiol-Michael addition, however, the reaction yield was too low. Also, the conjugation carboxylic acid site remains unknown. According to the structural configuration of folate receptor presented by Chen *et al.*,[36, 54, 62, 65, 92, 237, 260-265] the key recognition part of folic acid is the *pterin* group, indicating that modification of glutamate part will not affect the conjugation with folate receptors.

Which means it is not necessary to know the conjugated site on folic acid. In the Chapter 5.2, the direct coupling of TA-PEG-NH_2 and folic acid is explored aiming to increase reaction yield.

5.2.1 Coupling of FA and TA-PEG-NH_2

We considered possible coupling of folic acid with TA-PEG-NH_2 directly. The synthesis scheme is shown in Scheme 5.4. (See also Chapter 3.2.2 for details)

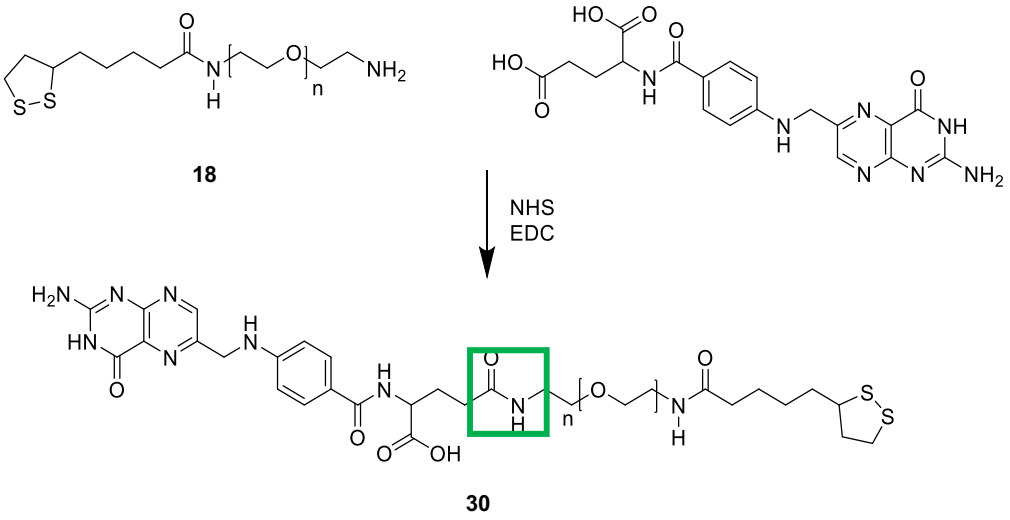

Scheme 5.4 Synthesis scheme of direct coupling of FA to TA-PEG-NH_2.

The mass spectrometry (MS) study confirms that conjugation of folic acid to TA-PEG-NH_2 was successful (Figure 5.4a). The MS shows only mono-conjugation. Since the γ-COOH has a lower pKa (4.7) than α-COOH (6.8), it is reasonable to assume that the conjugation was performed at the gamma site. However, a NOESY NMR experiment (Figure 5.4b) revealed that the alpha site was also activated and conjugated by TA-PEG-NH_2. Two coupling peaks between carbon proton and nitrogen carbon were

detected, interaction of H_aH_c, H_bH_c, indicates the α-site was linked.

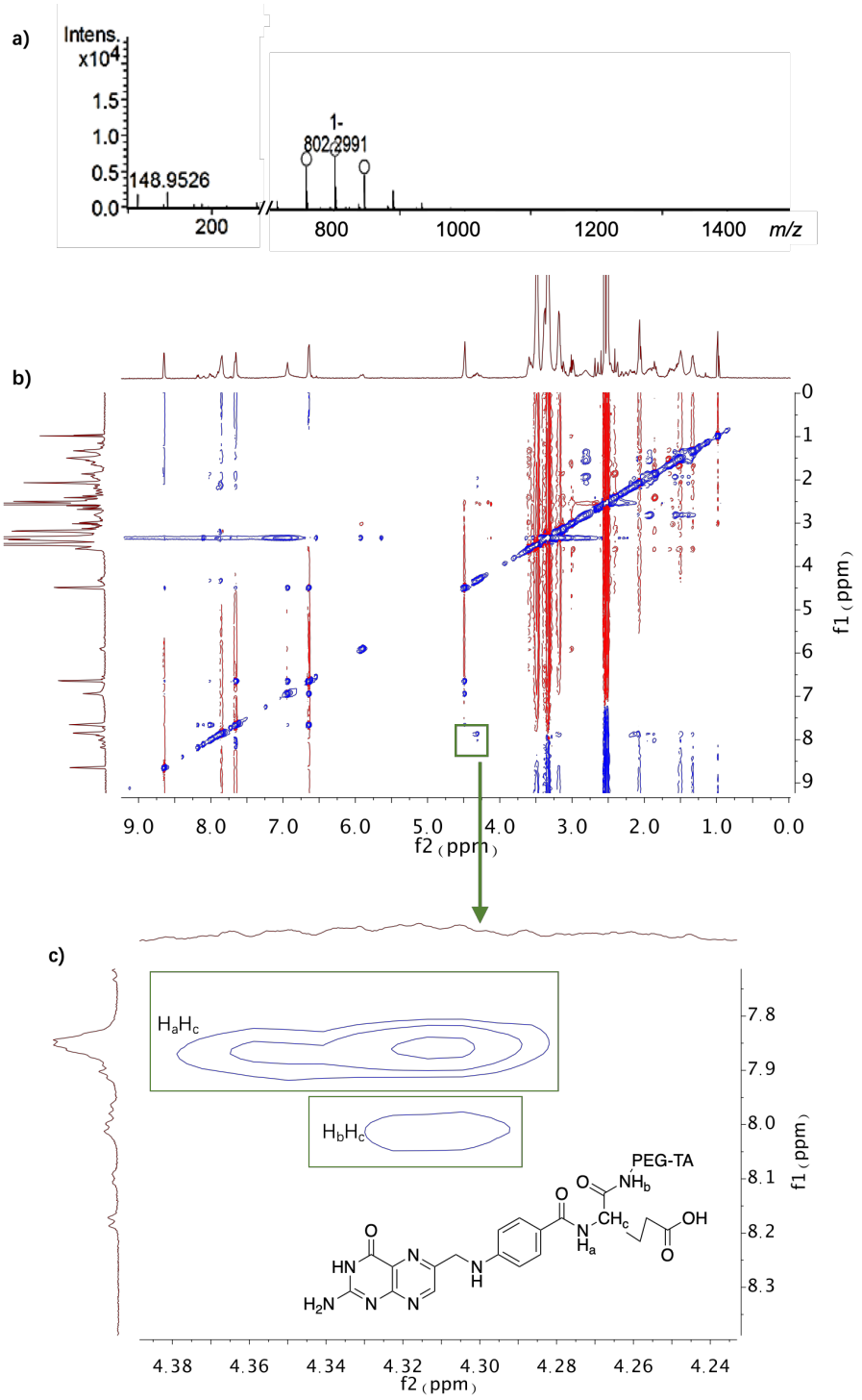

Figure 5.4 a) Mass spectrum **b, c)** NOESY NMR spectrum of FA-PEG-TA.

In summary, we have synthesized folic acid coupled PEG-TA ligands as a mixture of

α- and γ- conjugates. Nevertheless, based on Chen *et al.*'s study, both isomers are expected to target the folate receptors. The FA-PEG-TA obtained was then used for Au NCs synthesis.

5.3 Synthesis of Au NCs with FA conjugated ligands

The Au NCs were synthesized following the same procedure as for PEG-capped Au NCs (Figure 5.5**a**, see also Chapter 3.2.7 for details). Instead of using PEG-TA as ligands, FA-PEG-TA was used. The presence of FA did not affect the NC formation and monodisperse water-soluble spherical gold nanoclusters were formed with an average diameter of 1.60 $\pm$ 0.26 nm. A representative HRTEM image of FA-Au NCs is shown in Figure 5.5**d**.

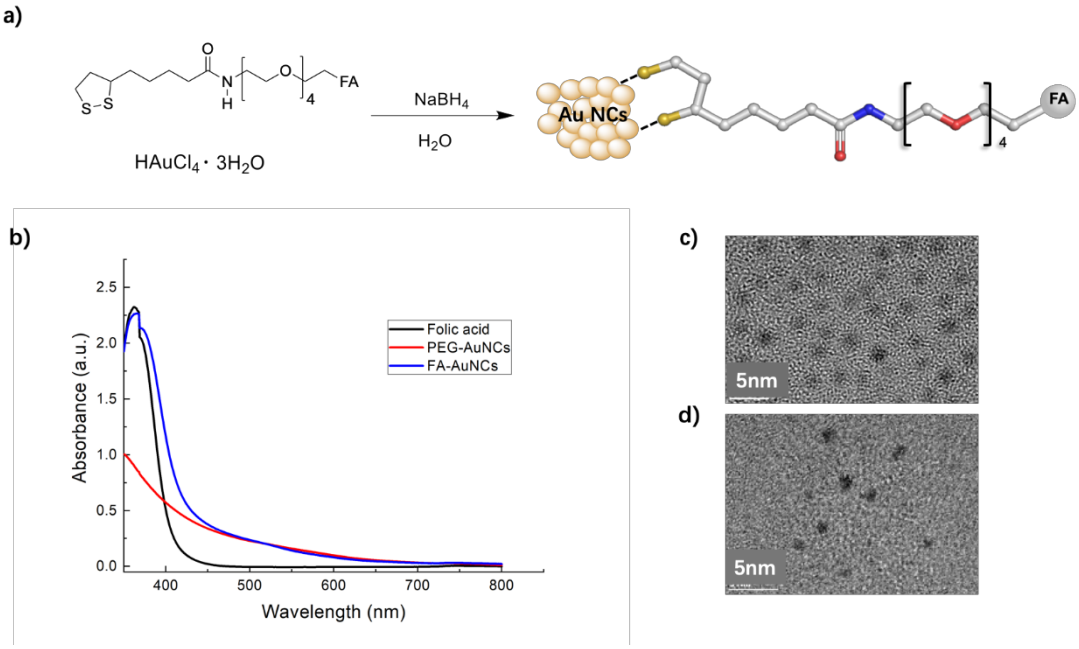

Figure 5.5 a) Synthesis scheme of FA-Au NCs. **b)** UV/Vis spectra of FA solution, PEG-Au NCs and FA-Au NCs solutions. HRTEM images of PEG-Au NCs **(c)** and FA-Au NCs **(d)**.

The UV/Vis spectrum shown in the Figure 5.5b confirmed the presents of folic acid on Au NCs. FA-PEG only showed no absorption at wavelength over 450 nm, while FA-Au NCs had same absorption in this range, indicating the formation of gold nanoclusters as PEG-Au NC. The observation of an absorption peak at ~ 370 nm in the solution of FA- Au NCs, confirmed the conjugation of folic acid on Au NCs, which was not observed in the PEG capped Au NC solutions.

The ^{1}H NMR spectra of both PEG-Au NCs and FA-PEG-Au NCs are shown in Figure 5.6. It was obvious that the FA-Au NCs spectrum (red) displays extra peaks (with blue arrows labelled) compared to that of PEG-Au NCs (green), indicating the presence of

folic acid of FA-PEG-Au NC sample.

Combined UV/Vis and NMR results proved that the Au NCs has been successfully conjugated with folic acid.

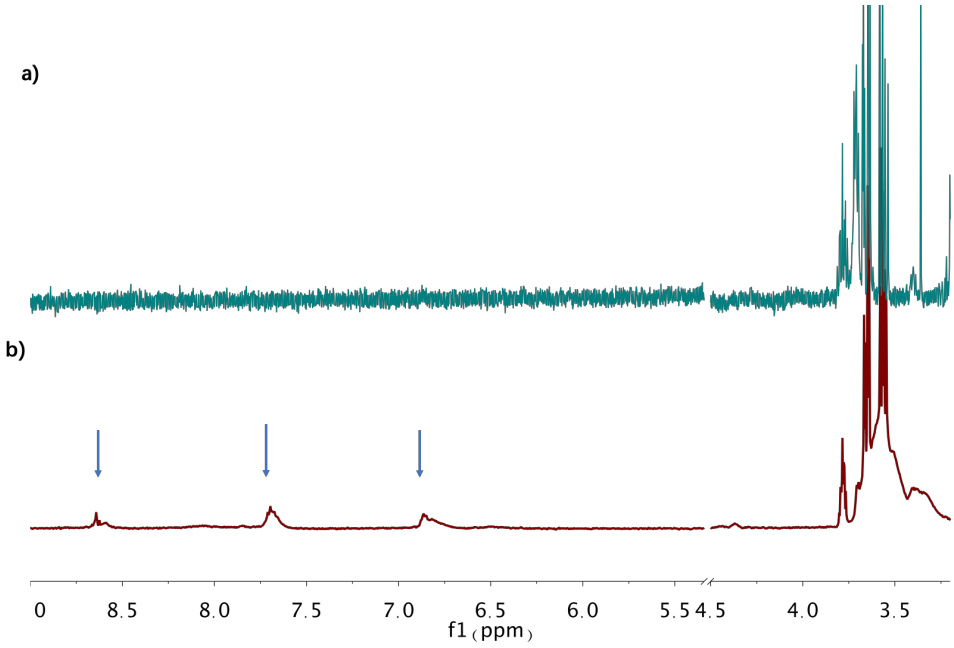

Figure 5.6 ^{1}H NMR spectra of **a)** PEG capped AuNCs and **b)** FA-PEG capped AuNCs.

A confocal imaging study was carried out to characterize the fluorescence properties of FA-Au NCs. Very weak fluorescence emission images was recorded for FA-Au NCs. Further optimization of imaging studies are needed to fully explore the potential of this material. However, since detectable fluorescence is recorded (Appendix), we envisaged that the folic acid conjugated gold nanoclusters can be potentially used as imaging agents.

5.3.1 Targeting activity of Au NCs capped with FA-PEG-TA

We have produced FA-PEG-TA-Au NCs and PEG-TA-Au NCs using the same synthesis parameters. UV/Vis spectra (Figure 5.5b) of FA-Au NCs and PEG-Au NCs have similar profile across the wavelength range 450 nm – 800 nm. The absorption spectrum of FA-Au NCs also revealed a distinct peak at ~ 370 nm, which was attributed to folic acid. These results also indicate that both nanoclusters sizes were below 2 nm, since no absorption at ~ 520 nm was observed.

The size of Au nanoclusters was analyzed using HR-TEM images recorded on a JEOL-2100F. The average sizes of PEG-Au NCs was 1.91 ± 0.33 nm (Figure 5.7). The FA-PEG-Au NCs had an average diameter of 1.60 ± 0.26 nm (Figure 5.5b). Both FA-Au NCs and PEG-Au NCs samples revealed narrow size distribution of spherical-like particles. The inter-crystal distance in Au NCs was 2.35 Å, which corresponds to the phase (111) of face-centered cubic (FCC) crystal structure. But it was hard to discern that FA-PEG capped Au NCs exhibiting the same structure in those images, limiting by the graphs resolutions. Since both NCs were obtained by the same procedures, we proposed that FA-PEG-Au NCs had the same structure, however, further analysis was needed to probe this.

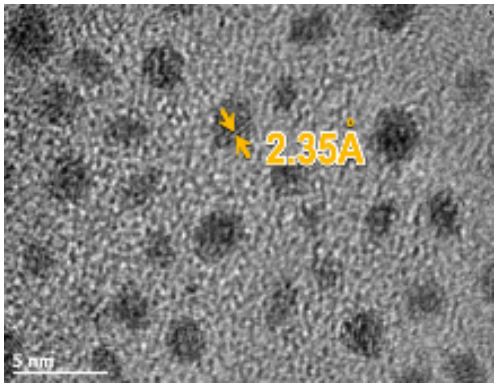

Figure 5.7 HRTEM images of PEG-Au NCs (arrows indicating the inter-crystal distance).

Since FA-PEG-TA ligands are longer than PEG-TA ligands, the capping efficiency may be different. We investigated the percentage coverage of ligands on the surface of NCs by probing the atom ratio of sulfur and gold, using an elemental analysis carried out by energy-dispersive X-ray spectroscopy (EDX) on JEOL-2100F. The atomic percentages of S and Au were 0.51 %: 0.80 % for PEG-Au NCs, the ratio of Au : S was estimated to be 1.57. The atomic percentages of S and Au were 0.18 % and 0.29% respectively for FA-Au NCs, Au : S ratio was 1.61. Hence, the PEG-Au NCs and FA-PEG-Au NCs have comparable Au/S ratios.

Table 5.1 Au : S ratio of Au NCs capped with PEG and FA-PEG ligands.

Sample	Sulfur (%)	Gold (%)	Au : S atomic ratio
PEG-Au NCs	0.51	0.80	1.57
FA-PEG-Au NCs	0.18	0.29	1.61
$Au_{38}(SR)_{24}$ [64]	/	/	1.58

Previous research on atomically precise gold nanoclusters were looked through, including $Au_{20}(SR)_{16}$, $Au_{24}(SR)_{20}$, $Au_{25}(SR)_{18}$, $Au_{36}(SR)_{24}$, $Au_{38}(SR)_{24}$, $Au_{40}(SR)_{24}$, $Au_{55}(SR)_{31}$, $Au_{67}(SR)_{35}$, $Au_{102}(SR)_{44}$, $Au_{130}(SR)_{50}$, and $Au_{144}(SR)_{60}$. [266] The $Au_{38}(SR)_{24}$ (Au/S = 1.58) was found to have the similar value with our NCs. All these atomic precisely nanoclusters are below 2 nm in size and are organic-soluble, while our Au NCs are water-soluble.

We estimated that our NCs contain 38 gold atoms. However, there is significant difference in the UV/Vis spectra of organic-soluble Au NCs compared to our DHLA-capped Au NCs. The spectra of water-soluble Au NCs solutions had no noticeable absorption feature at range of 400 nm – 800 nm, however, the $Au_{38}(SR)_{24}$ had two distinct absorption peaks at ~ 480 nm and 640 nm (Figure 5.8). Hence, the Au atom number in water-soluble Au NCs needed to be determined by other methods.

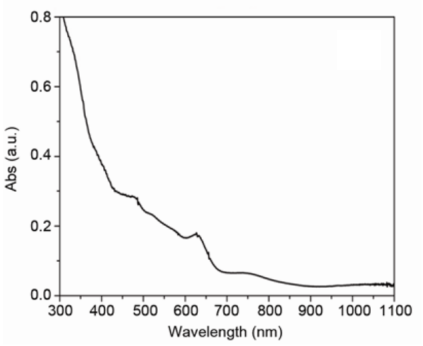

Figure 5.8 UV-vis spectrum of $Au_{38}(SC2H4Ph)_{24}$ nanoclusters.[267]

Both FA-Au NCs and PEG-Au NCs were excited by 254 nm UV lamp and images were captured by cameras. As shown in Figure 5.9, the observed colors were not identical even under same excitation wavelength. The fluorescence of PEG-Au NCs is weak, with slightly red emission observed, while the FA-PEG-Au NCs showing a strong blue fluorescence.

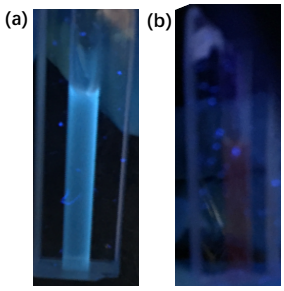

Figure 5.9 Photographs of fluorescence of **(a)** FA-PEG-Au NCs solutions and **(b)** PEG-Au NCs solutions with excitation at 254 nm.

Two reasons were proposed for the difference observed: (1) The structures of these two nanoclusters are different. (2) The fluorescence is affected by the ligands used and folic acid could be the main contributor to the blue fluoresce observed in FA-

PEG-Au NCs, since previous report confirmed fluorescence of FA at ~ 460 nm, in the range of blue light. [244]

5.3.2 Effect of synthesise parameters on FA-targeted Au NCs

Folic acid conjugated PEG ligands showed different properties compared to PEG based ligands, including their lengths, solubility, absorption profile, etc. The optimized parameters for PEG-stabilized Au NCs may not be directly transferable to FA-PEG-stabilized Au NCs, hence it is necessary to investigate the effect of the synthesis conditions (pH, Au: ligands ratios) on the formation of FA-PEG-Au NCs.

Folic acid has different solubility in media at different pHs.[268] The pH of ligands' solution used for synthesis was adjusted to pH = 7, 8, 9,10 or 11. Gold precursors were added in a molar ratio of 1: 3 of Au to ligands, and 1:2 of Au to $NaBH_4$. The aging time was 20 hrs.

The UV/Vis absorption spectra of these samples are shown in Figure 5.15. It is obvious that the lower reaction pH resulted in stronger absorption, which significantly enhanced NCs synthesis at pH = 7 at the wavelength range of 400 - 800 nm. No peak was observed at ~ 520 nm. Also, the Au NCs synthesized at pH = 7 did not produce a clear solution, exhibiting light yellow flocculation. We believed that the NCs precipitated due to low solubility of folic acid at pH ~ 7. The absorption profile of NCs synthesized at pH = 11 had the absorption profile expected for sub 2 nm particles (Figure 5.10). Therefore, pH 11 was chosen for further synthesis.

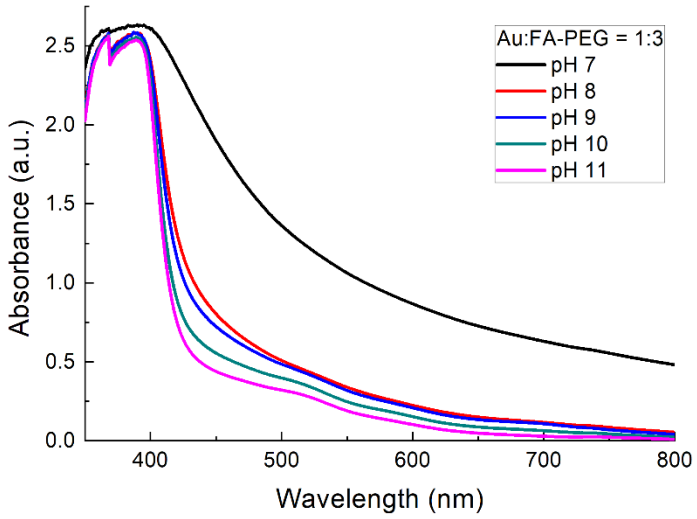

Figure 5.10 UV/Vis spectra of FA-PEG-Au NCs solutions synthesised at different pH values.

Since the diameter width of FA- PEG ligands is larger than PEG-based ligands (4.5 nm *vs.* 3.1 nm), their coverage density on gold surface will be affected.[268-270] The ratio of gold to ligands was investigated. The pH of ligands solution for synthesis was adjusted to pH = 11. Gold precursors were added in molar ratios of 1: 0.3, 1: 1, 1: 3, 1: 5 or 1:10 of Au to ligands; with fixed molar ratio of 1:2 of Au to $NaBH_4$, and each reaction was stirred for 20 hrs at room temperature.

All synthesises produced clear colloidal solutions, without any precipitate detected. The UV/Vis absorption spectra of each samples are shown in Figure 5.11. The 1 : 0.3 ratio of Au : ligand showed a distinct absorption around ~ 520 nm, indicating inefficient ligand density and formation of larger particles. The 1:1 ratio sample had no absorption at ~ 520 nm, however the absorption intensity was stronger than that

with larger ratios of ligands. Little differences were identified among 1:3, 1:5 and 1:10 samples, all showing absorption profile expected for ultra-small (sub 2 nm) particles. The ratio of 1:3 was chosen for further synthesis.

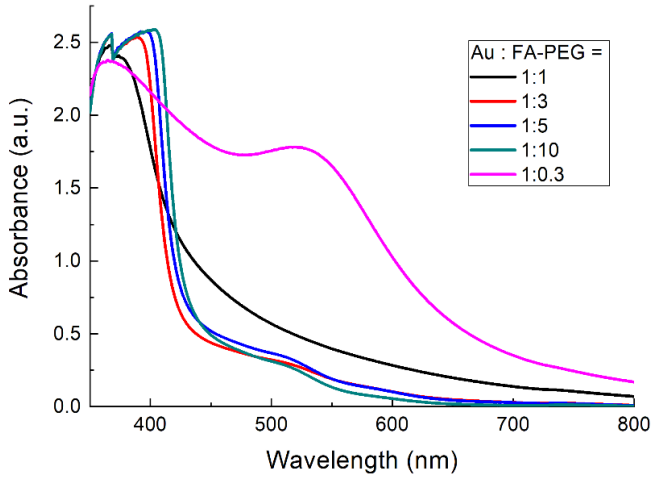

Figure 5.11 The UV/Vis spectra of FA-PEG-Au NCs solutions synthesised with different Au: L molar ratios.

5.3.2 Stability study of FA-PEG-Au NCs

The long-term stability study of FA-PEG capped Au NCs was assessed over a period of up to 2 month stored at 4 °C in the dark; after exposure to different pH and different temperatures after synthesis. UV/Vis spectroscopy was used to record the results.

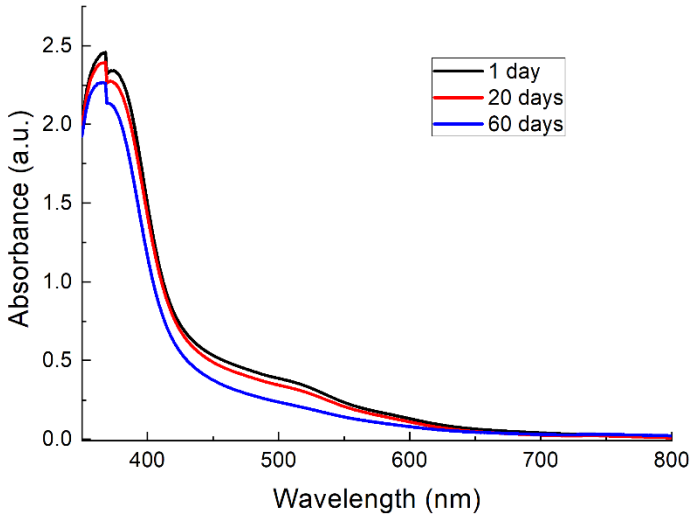

Figure 5.12 The UV/Vis spectra of FA-PEG Au NCs, taken after synthesis (original), and storage for 3 weeks and 2 months at 4 °C.

UV/Vis spectra of freshly prepared, 3 weeks old and 2 month old FA-PEG-Au NCs, stored at 4 °C are shown in Figure 5.12. The colloidal solutions remained aggregate-free with no significant changes in UV/Vis, indicating that the nanoparticles retain their shape/size and capping layer. Hence, attachment of FA does not alter the ability of ligands to provide efficient passivation of the surface and to stabilize them in aqueous solution.

The colloidal stability of NP can be altered by pH as it will change both the strength of ligand binding to Au NP and the charge on the ligand.

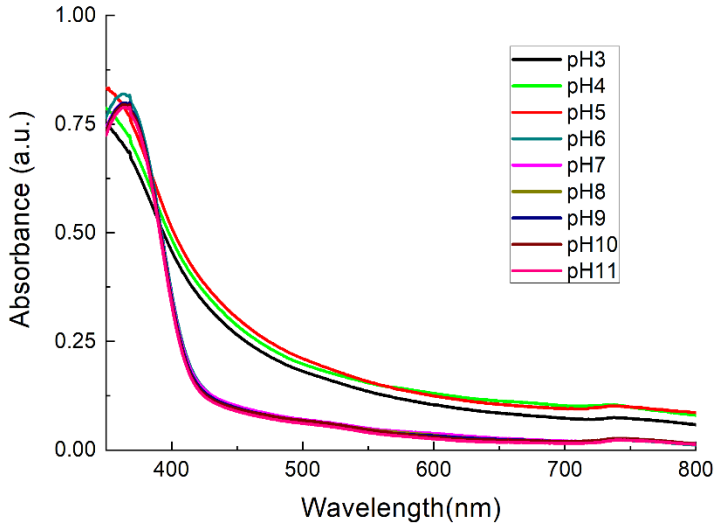

Figure 5. 13 The UV/Vis spectra of FA-PEG-TA capped Au NCs solutions at various pH values.

The pH of the Au NC solutions was adjusted by addition of 0.5 M NaOH, or 0.5 M HCl solution. Following 24 h storage at 4 °C, the stability of the Au NCs against changing pH and temperature was probed in the range of pH from 3 to 11. The absorption profiles of Au NP solutions at pH ≤ 6 are very similar, as well as those at pH ≥ 7.

These results confirmed that Au NCs capped with FA-PEG-TA present remarkable colloidal stability at neutral and basic environment. However, when the pH of the solution is lower than 6, the absorption was largely enhanced. This can be explained by the low solubility of folic acid under acidic solutions, leading to separation of gold nanoclusters capped by FA-based ligands from the colloidal solution and formation of aggregates. The observed aggregation is reversible by addition of NaOH to increase

the pH.

We observed that all synthesized solutions being stored for 24 h at 4 °C retained their colloidal stability. Solutions treated to pH values in the range from 7-11 were also stable, Solutions stored at acidic pH became flocculated. The precipitation was reversible if solution pH was increased.

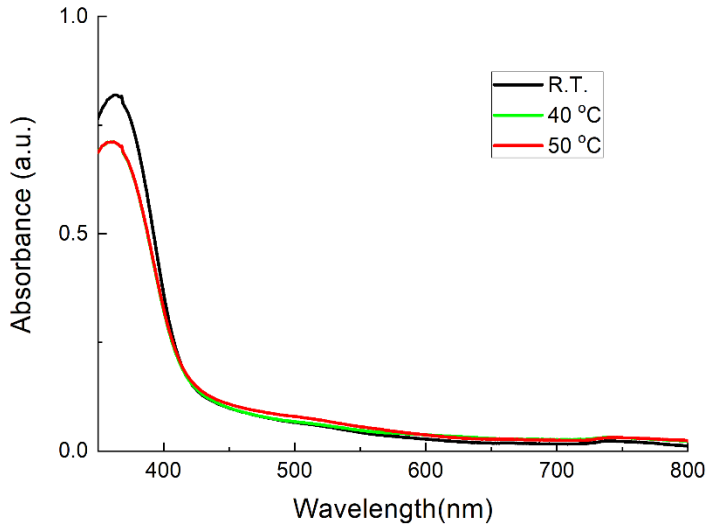

Figure 5.14 The UV/Vis spectra of FA-PEG-TA capped Au NCs solutions treated at temperatures of 40 °C and 50 °C.

The thermal stability of Au NCs capped with FA-PEG-TA were studied at T = 40 °C and 50 °C. The vials containing Au NC solutions were heated in a water bath and kept for 1 h. The UV/Vis absorption profiles have not revealed any significant changes, apart from decrease of intensity of peak at 370 nm. At first, we proposed that the decomposition of folic acid at higher temperature is a possible reason for the weaker absorption following thermal treatment at 50 °C. Day *et al.*[271] reported that folic acid

has a retention of 75 - 92% after 2 h at 100 °C, which shows that folic acid is slight unstable at such temperatures. But it seems very unlikely at 50 °C, since many studies on folic acid stability in liquid media were in agreement with a starting degradation temperate of 180 °C.[248] However, the absorption of gold nanoclusters at 520 nm was not disturbed by the increased temperature, indicating thermal stability of Au NCs solutions.

In conclusion, FA-PEG-TA-stabilized Au NCs have long shelf life (> 3 months) and are stable at pH is above 7 and at T = 40 °C or 50 °C.

5.3.4 The magnetic properties of FA-PEG Au NCs

^{1}H NMR was used to assess the magnetic properties of FA targeted Au NCs. The studies were performed by the method described in Chapter 4.3.6.2.

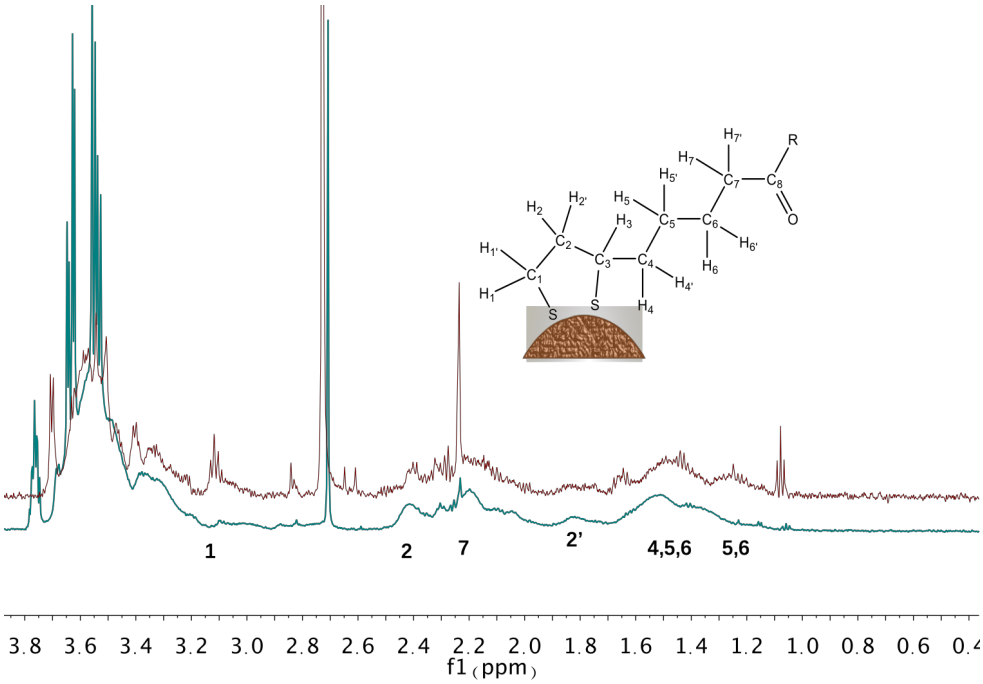

Figure 5.15 600 MHz ^{1}H NMR spectrum of FA-PEG only (red) and FA-PEG Au NCs (blue) in 90% H_2O + 10% D_2O at 298K (Inset shows a structure of thioctic acid attached to gold core with numbered hydrogens and carbons).

The ^{1}H NMR spectra of FA-PEG-TA capped Au NCs and FA-PEG-TA only samples are shown in Figure 5.15. A complete assignment of all observable nuclei was established by combining 1D ^{1}H, ^{13}C NMR spectra with 2D-COSY and HSQC techniques. The corresponding protons are numbered in a proximity sequence to the gold core on the TA molecular structure and labelled on ^{1}H NMR spectra (Figure 5.16).

The results are comparable to those for PEG-TA capped Au NCs: peaks of protons close to the gold core were less intense and broader compared to ligand only sample. The signal broadening results from proximity of proton to metal core and is likely due to interaction with species of paramagnetic in the samples. Since this effect is a

manifestation of unpaired electron magnetic moments effecting efficient nuclear relaxation.[122, 139, 272-274]

The longitudinal relaxation time, T_1, of the protons in close proximity to the paramagnetic Au NCs is expected to be shorter than for ligand-only solutions. The Table 5.2 summarizes the T_1 values estimated in our studies.

Table 5.2 Longitudinal relaxation time, T_1, for Au NCs and ligands only solutions.

Position	***T1, Au NP(sec)***	***T1, Ligands(sec)***
1	0.74	0.75
2	0.85	1.55
2'	0.687	0.69
4,5,6	0.634	0.76
5,6	0.696	0.91
7	0.7	1.32

The paramagnetic enhancement is expected to decrease with longer distance.[272, 275] We observed an overall decrease of T_1 values. However, no significant changes were observed for ^{1}H in positions 1 and 2', which requires further investigations.

In summary, the presence of signal broadening in proton NMR and shorten T_1 times

confirmed the paramagnetic centre of FA-Au NCs.

5.4 Conclusions

In this chapter, we have confirmed that FA conjugated ligands were successfully used to stabilize the Au NCs solutions. The size of Au NCs formed is 1.6 ± 0.3 nm.

Two methods were used to obtain FA conjugated PEG-TA ligands: 1) FA was modified to FA-SH, while PEG-TA was converted into maleimide-PEG-TA, then FA-SH was attached to PEG by a thiol Michael addition; 2) Direct coupling of FA to NH_2-PEG-TA. The FA-PEG-TA was used in colloidal synthesis of Au NCs with following optimized parameters: molar ratio of Au: Ligand = 1:3, pH = 11. The FA aqueous solution of capped Au NCs have colloidal stability both in a basic environment and at temperatures up to T = 50 °C. The long-term stability of FA-Au NCs were demonstrated at least for 2 months. The analysis of T_1 relaxation time indicated the presence of paramagnetic centers in FA-PEG-Au NCs.

Chapter 6

In Vitro studies of targeted and non-targeted Au NCs

Colloidal Au NCs are of potential interest for cancer therapy. However, several studies indicated possible NC-induced cytotoxicity,[276] which is determined by NC structure, size and capping ligands.[277]

More than 70 different types of serum proteins have been found adsorbed to the PEG capped Au NPs surfaces (PEG at densities up to 1.25 PEG/nm^2).[278] However, PEG was also found to resist protein absorption and reduce nonspecific endocytosis uptake.[156] Zhang *et al.* had investigated the *in vivo* toxicity in mice with 5, 10, 30 and 60 nm PEG(size not mentioned)-capped Au NPs, showed that all four particles presented side effects in mice with different severities.[279] However, there is limited information on toxicity on Au NCs capped with PEG or other capping ligands with d < 5 nm.

To assess the potential of our Au NCs for bio applications, an *in vitro* study was carried out to investigate the effects of Au NCs on cell viability. MTT assays were used to evaluate the *in vitro* cytotoxicity of Au NCs. ICP-MS was employed to quantify the cellular uptake of Au NCs. Considering the reported recycling rate of FR α as 5.7 - 20 h, [280] we chose 72 h as the incubation time to for MTT assay to maximize the

internalization of NPs by the cells.

6.1 *In vitro* cytotoxicity study of Au NCs

Cell viability assays were performed to assess *in vitro* cytotoxicity of Au NCs (see Chapter 3.3.1 and Figure 6.1 for details). Briefly, cells were seeded in a 96-well plate at a density of 3000 cells per well for 24 h. Au NC solutions were added at a range of concentrations between 10 nM to 100 μM, and cultured at 37 °C for 72 h. 3-(4,5-Dimethylthiazol2-yl)-2,5-diphenyltetrazoliumbromide (MTT) was added to each well at an ending concentration of 0.5 mg/mL. After 2.5 h incubation, the growth medium was removed and DMSO was added to dissolve the produced formazan; The absorbance was measured at 550 nm (extinction coefficient of MTT formazan is 16900 at 578 nm)[252] for each well. Each assay was repeated at least 2 times, and each concentration was repeated 6 times.

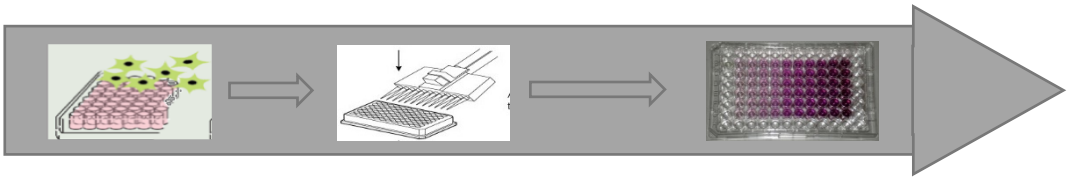

Figure 6.1 The schematic representation of a procedure used for MTT assay.

6.1.1 Cytotoxicity of Au NC capped with different length PEG

The MTT assays were analyzed with Au NCs of d < 2 nm stabilized by DHLA-PEG400-NH_2, DHLA-PEG550-OCH_3, and DHLA/TA-PEG200 with a gold concentration from 10 nM to 100 μM. The concentrations of gold were assumed as no loss in synthesis procedures. We have selected a human-derived colorectal carcinoma cell line, HCT-116 and a human-derived breast cancer, MCF-7 to evaluate the toxicity

The cell viability, expressed as percentage of the untreated control, of MCF-7 and HCT-116 exposed to Au NCs for 72 h are shown in Figure 6.2.

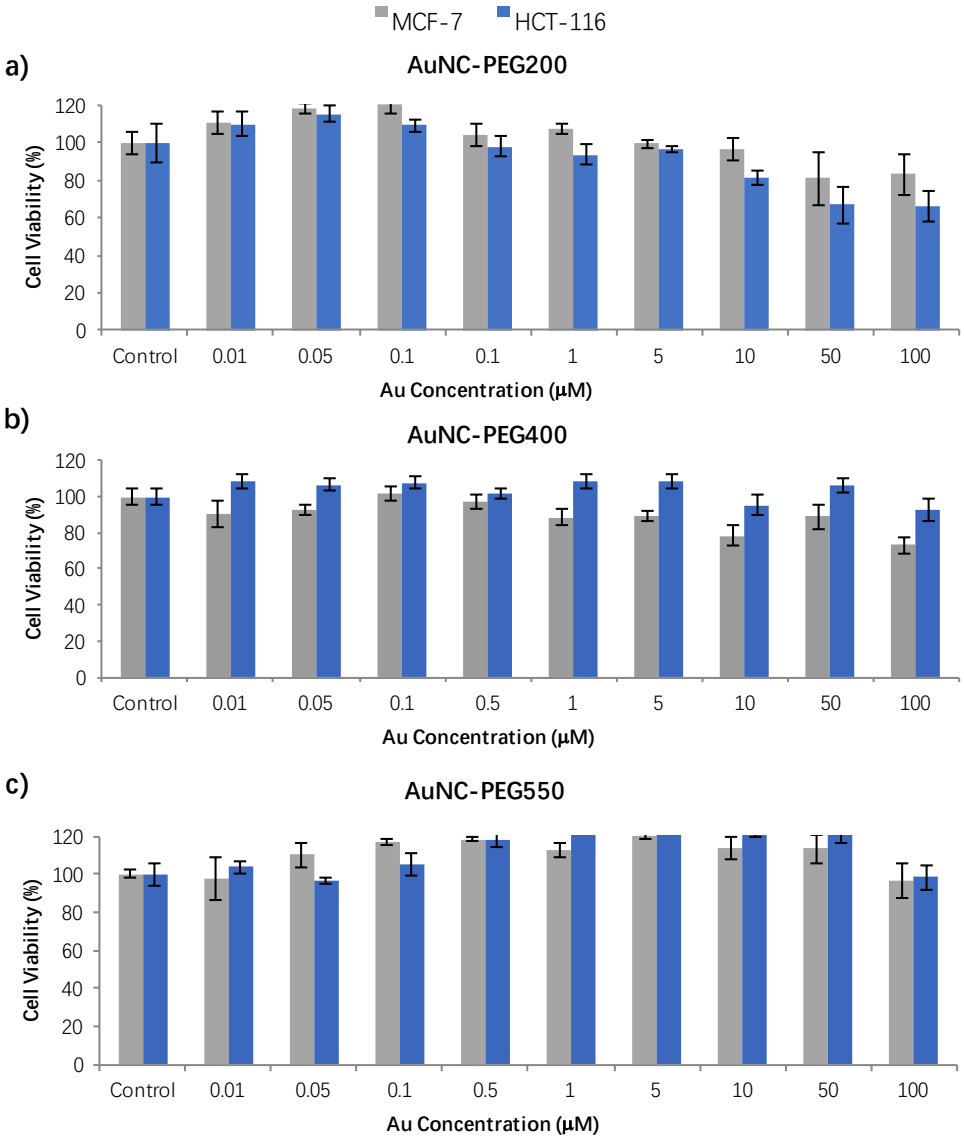

Figure 6.2 Viability of MCF-7 and HCT-116 cells after 72 h of incubation with different concentrations of **(a)** DHLA-NH-PEG200-NH_2 **(b)** DHLA-PEG400-NH_2 **(c)** DHLA-PEG550-OCH_3 capped Au NCs estimated from MTT assay. The error bars represent the standard deviation over 6 repeats.

Both cell lines retain over 60% viability following 72 h exposure to Au NCs at Au concentration up to 100 μM. The DHLA-NH-PEG400-NH_2 capped Au NCs showed no toxic effects with cell viability > 70 %: 80 % for MCF-7 and ~ 70% for HCT-116

at exposure concentration of 100 μm. The DHLA-NH-PEG550-OCH_3 capped Au NCs also showed high cell viability > 90 % at exposure concentration up to 100 μm both for MCF-7 and HCT-116. The cell viability of DHLA-NH-PEG200-NH_2 capped Au NCs are > 80% for MCF-7, however only ~ 60 % for HCT-116. We proposed that shorter ligands may lead to a closer distance of gold surface and cells' apparatus, the 'naked' surface gold affects apparatus' functions and result in a lower cell viability. Leopold *et al.*[281] produced PEG200 capped Au NPs size of 12 nm – 27 nm. They observed a cell viability over 80% with A549 cells treated by PEG-Au NPs below the concentration of 450×10^{-9} M. These Au NPs are therefore regarded as having good biocompatibility.

Hence, we have demonstrated that our PEG-capped Au NC have little side effects on the viability of MCF-7 and HCT-116 cell lines.

6.1.2 Targeting high folate-receptor expressing cell lines with FA-conjugated Au NCs

In order to assess possible toxicity induced by FA and to probe if FA is showing targeting capability, two cell lines were selected: involved in this analysis, folate receptor expressing breast cancer cells (FR-positive), MCF-7 and MDA-MB-231. FR-negative cell line, HCT-116 was used as control cells. The cellular uptake of FA-Au NCs by FR-positive cells is anticipated to be higher than by FR-negative cell lines.

The studies of receptors in cells are sparce. For FR, four isoforms of FR were identified

as FR (α, β, γ, δ).[282] Moreover, they are activated even when the folate is at low concentration or when rapid cell growth requires elevated folate uptake. However, the isoforms have different cellular distribution patterns and tissue specificity. FR α is expressed in normal epithelial cells and its expression is markedly enhanced in several carcinomas, including breast cancers. The FR β is often overexpressed in non-epithelia malignancies.[283, 284] These two isoforms are not expected to be present at the same time. Yang *et al.*[285] suggested that the coexistence of FR β was not possible on the tumour itself, but on the tumour-associated macrophages (TAMs) that accumulated at the tumour sites.

Several studies reported that MCF-7 cells are FR overexpressing,[282, 286] while other reports suggested that they are FR-negative. [287] The MDA-MB-231, another breast cancer cell line, was confirmed to have a high folate receptor expression. MDA-MB-231 cell lines was found to have the greatest abundance of FR α. with 369 ± 6 fg/cell. The MCF-7 have 209 ± 5 fg/cell of FR α.[288] There are no reports suggesting folate receptor overexpression by HCT-116 cells.

The cells were exposed to Au concentration from 10 nM to 500 μM. The observed cell viability is shown in Figure 6.3. For concentrations up to 100 μM, all cell lines retained viability over 80 %. These results are comparable to previously reported values for FA-conjugated AuNP.

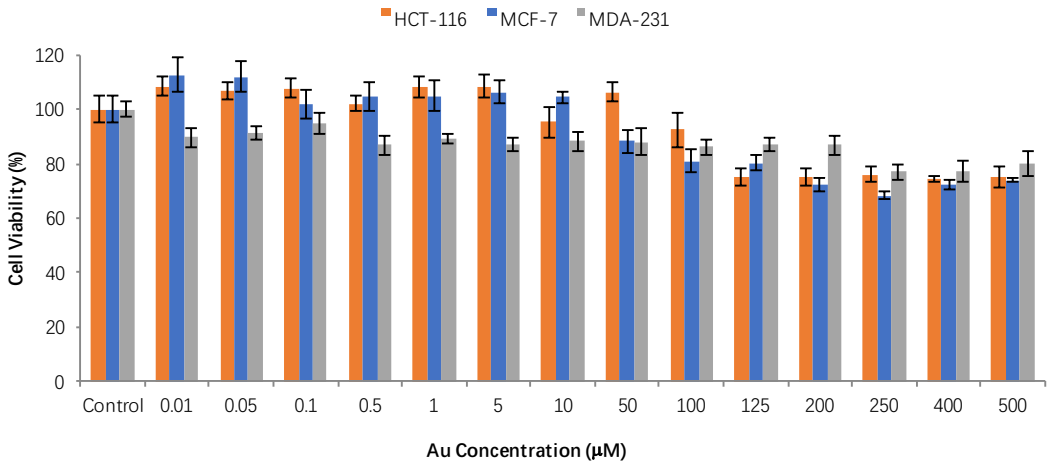

Figure 6.3 All Viability of MCF-7, HCT-116 and MDA-MB-231 cells after 72 h exposed to **FA-PEG-TA** capped Au NCs. The error bars represent variations between 6 repeats of each concentration.

Based on amount of FA receptors, MDA-MB-231 cells were expected to uptake more gold nanoclusters than other two cell lines, however the cytotoxicity observed was comparable. Hence, cellular uptake studies are needed to quantity Au NC uptake by FR-positive cell line and FR-negative cell line.

6.2 Cellular uptake of FA-PEG-Au NCs

MTT assays revealed no cytotoxicity induced by non-targeted and targeted Au NCs in all studied cell lines. To confirm the ability of FA to target cells, the cellular uptake of Au NCs was assessed by ICP-MS. Two types of cell lines were chosen for cellular uptake study, FR-positive cell lines, MDA-MB-231 and FR-negative A549, a human lung cancer cell line. A549 were found more FR-negative than HCT-116.

6.2.1 Uptake of Au NCs by folate receptor - positive cell lines

The results of ICP-MS are expressed in weight concentrations, and were related to the nanoparticle numbers. For the first experiment, PEG-Au NCs and FA-PEG Au NCs were incubated with MDA-MB-231 for 72 h (see Chapter 3.3.2 for details). After washing out the extracellular Au NCs with PBS, the cells were digested by concentrated HNO_3 and diluted by adding water to volume of 5 ml and ready for ICP-MS analysis. The detailed results are listed in Table 6.1. ICP-MS experiments were performed by Dr. Scott Young (University of Nottingham). The treatment concentration value was also estimated by ICP-MS using Au NCs only solutions.

Table 6.1 Concentration and cellular uptake of Au NCs by MDA-MB-231 determined by ICP-MS.

	Treatment concentration (*μ*g/well)	**Amount of Au uptake (μg)**	**Au uptake (%)**
FA-Au NCs	56.25	9.98	17.7
PEG-Au NCs	382.30	35.12	9.2

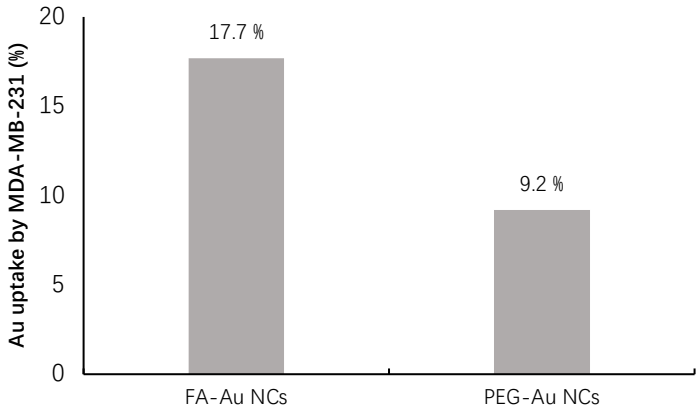

Figure 6.4 Au NC uptake in MDA-MB-231cell line exposed to PEG-Au NCs and FA-Au NCs nanocomposites.

As shown in Figure 6.4, the uptake of the folic acid modified Au NCs was about 2 times greater (17.7 %) compared to non-targeted PEG-Au NCs (9.19 %), despite lower effective treatment concentration. These results indicate that FA-Au NCs have a higher uptake rate than PEG-Au NCs in FR-positive cells, confirming FA induced targeting.

For the 2nd time of ICP-MS analysis, 2 mL of Au NCs at concentration of 10 μg /mL were used to treat both MDA-MB-231 and A549 cells for 72 hrs. The results are summarized in the Table 6.2.

Table 6.2 Concentration and cellular uptake of FA-Au NCs/PEG-Au NCs by MDA-MB-231determined by ICP-MS.

	Treatment concentration (*μ*g/well)	**Amount of Au uptake (μg)**	**Au uptake (%)**
FA-Au NCs	20.00	11.86	59.31
PEG-Au NCs	20.00	9.97	49.85

Despite lower effective treatment concentration, greater Au uptake was obtained. About 10 % enhancement of uptake induced by FA was observed. We proposed that since the first experiment we were using a more concentrated Au NCs solution, a lower cell viability is the reason for the observed difference. Less remaining cells would lead to less amount of Au uptaken. We conducted cell viability assay to support the suggestions (Figure 6.5). Since cells for ICP-MS study were incubated in 2 mL of media, a concentration of 20 μg/mL was used for the treatment used in 1st experiment and 10 μg/mL corresponds to 2nd experiment. As displayed in Figures 6.5, the cell viability of 20 μg/mL (62%) was slightly lower than 10 μg/mL (67%).

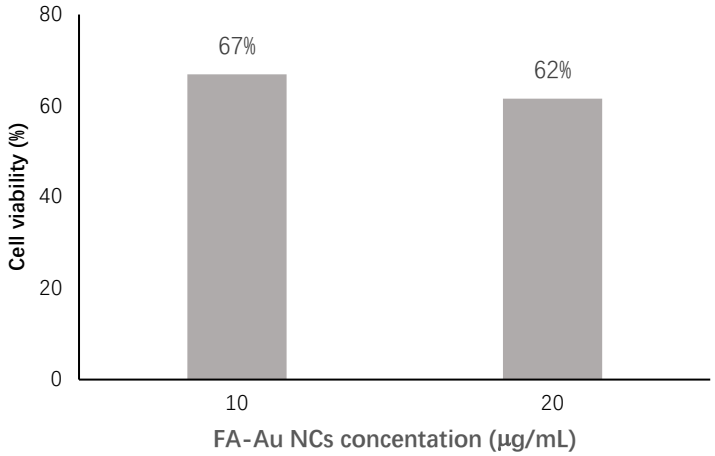

Figure 6.5 Cell viability of MDA-MB-231 of 72 hrs incubation with FA-Au NCs in concentrations of 10 μg/mL and 20 μg/mL.

We suggested that smaller cellular uptake by cells were result in small quantity of alive cells, the lower viability was leaded by treatment with concentrated Au NCs solutions. This also explain the small Au uptake of PEG-Au NCs by MDA-MB-231. The cell viability assays were carried out using PEG-Au NCs concentration of 200 μg/mL denoting 382.3 μg, and 10 μg/mL for 20 μg sample. The cell viability was 68% and 41% of 10 μg/mL and 200 μg/mL, respectively. Although the value of cells viability under 10 μg/mL only show about 1.5 times of that under 200 μg/mL, the images (Figure 6.6 b and c) show obvious differentiations. Most cells in 10 μg/mL media were still alive, while cells in 200 μg/mL were observed with mortality and accumulation. We envisaged that the high cell viability of sample treated with concentrated Au NCs solution was attributed to the absorption of Au NCs in high concentration.

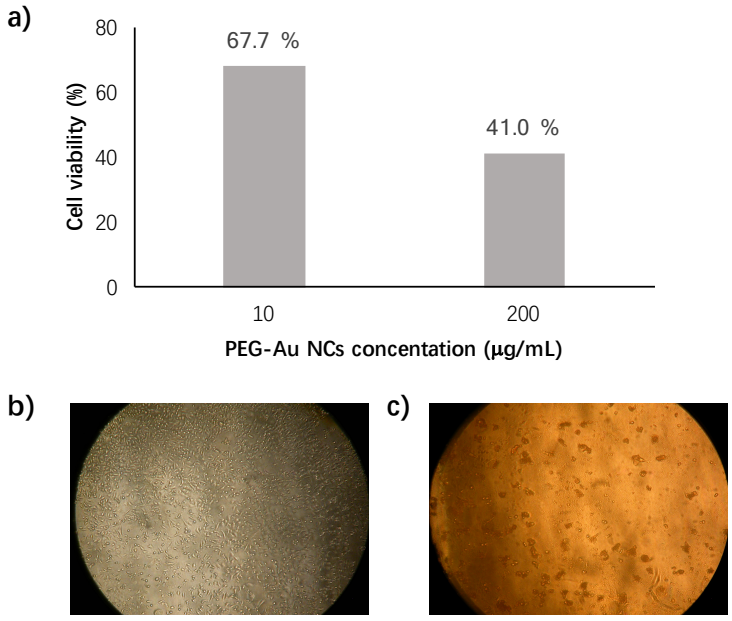

Figure 6.6 a) Cell viability of MDA-MB-231 after 72 hrs incubation with PEG-Au NCs at concentrations of 10 µg/mL and 200 µg/mL and optical microscopy images of cells after exposed to Au NCs at concentration of **(b)** 10 µg/mL and **(c)** 200 µg/mL.

The cellular uptake experiment was repeated for 3rd time. New batches of the Au NCs were synthesized and used for cells treatment. The parameters and results are listed in Table 6.3. The incubating concentrations of two types Au NCs solutions are comparable: 13 µg/mL for FA-Au NCs, and 14.15 µg/mL for PEG-Au NCs. It is apparent that MDA-MB-231 uptaken more FA-Au NCs (66.3%) than PEG-Au NCs (58.34%).

Table 6.3 Concentration and cellular uptake of FA-Au NCs/PEG-Au NCs by MDA-MB-231determined by ICP-MS.

	Treatment concentration (*μ*g/well)	**Amount of Au uptake (μg)**	**Au uptake (%)**
FA-Au NCs	25.99	17.23	66.30
PEG-Au NCs	28.30	16.51	58.34

We note, that these repeat experiments represented three different conditions of cells treatment concentrations: 1) FA-Au NCs quantities (56.25 μg) largely smaller than PEG-Au NCs' (382.3 μg); 2) FA-Au NCs quantities and PEG-Au NCs' were identical (20 μg); 3) FA-Au NCs (25.99 μg) quantities slightly smaller than PEG-Au NCs (28.3 μg). The cellular uptake weight rate of both Au NCs by MDA-MB-231 are shown in Figure 6.7. Our results indicate that FA modified Au NCs given a greater uptake than non-targeted Au NCs for all three conditions.

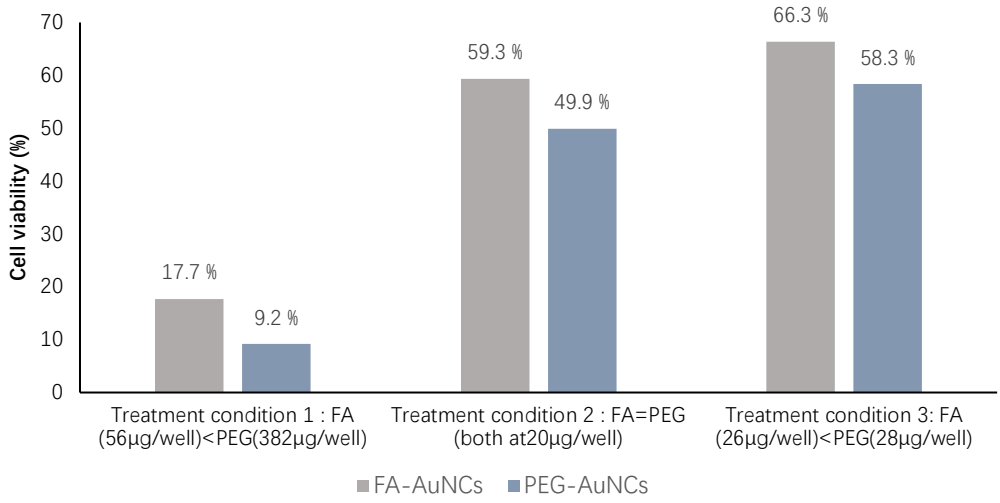

Figure 6.7 Comparison of FA-Au NCs and PEG-Au NCs cellular uptake rate by cell line MDA-MB-231.

6.2.2 FR-negative cell lines uptake of Au NCs

We conducted a cellular uptake study on FR-positive cell lines MDA-MB-231, and demonstrated greater uptake of folate receptor targeted Au NCs compared to non-targeted cells. In this part, a FR-negative A549, human lung cancer cell line was studied for comparison.

The procedure used was similar to that used for MDA-MB-231 and was repeated 2 times. Comparable weight concentration of clusters was used. A concentration of 10 µg/mL was used to incubating cells with both Au NCs for the first experiment. The 2nd experiment used concentrations of 13 µg/mL for FA-Au NCs, 14.15 µg/mL for PEG-Au NCs, corresponding to ~ 26 µg/well for FA-Au NCs and ~ 28 µg/well for PEG-Au NCs. The cellular uptake of two types Au NCs by A549 are listed in Table 6.4.

Table 6.4 Concentration and cellular uptake of FA-Au NCs/PEG-Au NCs by A549 determined by ICP-MS.

	Treatment concentration (*μ*g/well)	Amount of Au uptake (μg)	Au uptake (%)
FA-Au NCs	25.99	13.15	50.59
PEG-Au NCs	28.30	11.32	40.01

It was surprising to find that, for the FR-absent cell lines, FA-Au NCs (50.59 %) still displayed superior endocytose than PEG-Au NCs (40.1 %). It was expected that they would have similar intracellular weight of gold. We suggested the smaller size of FA-Au NCs (1.60 nm) than PEG-Au NCs (1.91 nm) that lead to a better retention of FA-Au NCs in cells.

Table 6.5 Concentration and cellular uptake of FA-Au NCs by MDA-MB-231 and A549 determined by ICP-MS.

Cell lines	Treatment concentration (*μ*g/well)	Amount of Au uptake (μg)	Au uptake (%)
MDA-MB-231	25.99	17.23	66.30
A549	25.99	13.15	50.59

A comparison of gold incorporated in FR-positive cells and FR-negative cells is

presented in Table 6.5. Since the same concentration of Au NCs were used in incubating both cells, the initial amount of seeded cells were kept the same, 5×10^5 cell/well. We also counted each line cells number in the reference wells after 72 hrs incubation in PBS media, the results were all around 1x 10^6 cell/well (~ 1.05×10^6 cell/well of MDA-MB-231, ~ 0.9×10^6 cell/well of A549). We propose that small difference in cell number cannot account for the observed different in uptake, FA-Au NCs exhibited a higher uptake in FR-positive cell line MDA-MB-231 (66.3 %) than FR-negative cell line A549 (50.59 %). As expected, the FR-positive cell line uptakes FA-Au NCs more effectively than FR-negative one.

In this project, we used ICP-MS to assess and quantify the cellular uptake of Au NCs. Further studies using the complementary analysis, such as competitor assay (using unbounded ligand as competitor) could be used to confirm ligand specific uptake. Hou *et. al*, [289] incubated cells with labeled folic acid in the presence and absence of unlabeled folic acid and successfully carried out the FR α binding and uptake assays.

6.3 Conclusions

In this chapter, we have investigated the *in vitro* behaviour of folic acid modified Au NCs and non-modified Au NCs. MTT assays were carried out to examine the cytotoxicity, and ICP-MS were used to analyse the gold uptake by cells.

Both FA-Au NCs and PEG-Au NCs were shown to be non-toxic to HCT-116, and MCF-7. FR-positive cell line MDA-MB-231dispalyed a high tolerance of FA-Au NCs

up to concentration of 500 μM.

FA-Au NCs show stronger cellular uptake than PEG-Au NCs with MDA-MB-231 in both cells treatment concentration scenarios: identical treating concentration or FA-Au NCs concentration less than that of PEG-Au NCs. These results confirm our predictions, since MDA-MB-231 have high expression of folate receptor, leading to more FA-Au NCs bonded than normal NCs.

This proposal was further confirmed by comparing the cellular uptake of FA-Au NCs on FR-positive MDA-MB-231 and FR-negative A549. Cell lines MDA-MB-231 uptake more Au NCs than A549 under the same incubation concentrations, 13 μg/ml.

We found that FR-negative cell lines also absorbed increased targeted NCs than non-targeted NCs, and proposed that targeted NCs were prompted be included by A549 since its smaller size. However, the endocytosis mechanism may different with FR-positive cells. We suggested that the size effect was the main factor for NCs accumulating in A549 cells, and receptor endocytosis was the main factor for MDA-MB-231.

Chapter 7

Conclusions and future work

In this project, a range of Au NCs with different capping ligands were successfully synthesized. Au NCs capped with dodecantheiol are soluble in *iso*-propane and have homogeneous size distribution of 2.2 ± 0.4 nm. Then, water-soluble gold nanoclusters was produced using PEG-based ligands. By optimizing experimental parameters for Au NCs synthesis as Au: Ligands ratios = 1: 3, reaction pH values: ~11, aging time = 20 hrs, Au NCs capped by TA-PEG400-NH_2 with an average diameter of 1.7 ± 0.4 nm were obtained. The produced aqueous Au NCs solution exhibited long-term colloidal stability (over 180 days), high tolerance over a wide range of pH (3-10) and temperatures (T = 40 °C and 50 °C). Both dodecanthiol-capped and PEG-capped gold nanoclusters demonstrated paramagnetism at a temperature lower than 50 K. PEG-capped revealed magnetic property up to 300 K. Moreover, PEG-based Au NCs had stronger paramagnetism which was further verified by a shorter relaxation times T_1 observed for protons on the capping ligands in Au NC samples estimated from ^{1}H NMR studies.

For Au NCs further application on cancer treatment, we have confirmed that FA conjugated ligands, an targeting agents, were successfully used to stabilize the Au NCs solutions. The FA conjugated PEG-TA ligands was generated by direct coupling of folic acid to NH_2-PEG-TA. FA-AuNCs with an average diameter of 1.6 ± 0.3 nm was

produced by colloidal synthesis using the optimized parameters: molar ratio of Au: Ligand = 1:3, pH = 11. The aqueous solution of FA-Au NCs show long-term colloidal stability in a basic environment and at temperatures up to T = 50 °C. The analysis of T_1 relaxation time of protons on ligands indicated the presence of paramagnetic centers in FA-PEG-Au NCs.

Finally, we probed the cytotoxicity of targeting Au NCs and non-targeting Au NCs using cell viability assay and quantified their cellular uptake by ICP-MS. All water-soluble Au NCs were demonstrated non-toxic to HCT-116, and MCF-7. The FR-positive cell line MDA-MB-231 even displayed a high tolerance to FA-Au NCs up to a concentration of 500 μM. FA-Au NCs show greater cellular uptake than PEG-Au NCs (1.1-1.9 fold) with MDA-MB-231 which attributed to the cell lines' high expression of folate receptor. The comparison of cellular uptake FA-Au NCs on FR-positive MDA-MB-231 (1.3 fold of A549) and FR-negative A549 further confirmed this proposal. We also found that FR-negative cell lines absorbed increased targeted NCs than non-targeted NCs. It was proposed that targeted NCs were prompted be included in FR-negative cell by a different endocytosis mechanism, the size effect was the main factor for NCs accumulating in A549 cells. While the receptor endocytosis was the main factor for MDA-MB-231.However, further study need be done to verify this proposal.

We have proceeded many results with this project, however, some questions remain. We hope that these questions could be investigated in future research.

i) The quantification of Au NCs' magnetic properties, like the spin state of the system which can be explored and calculate by further electron paramagnetic resonance (EPR) or NMR study. To offer a better instruction for its potential therapy applications.

ii) Although folic acid was successfully attached to Au NCs by the PEG intermediate, we are not able to determine which carboxyl site was conjugated. More works need be carried out to confirm this.

iii) We have demonstrated that FR-positive cell lines MDA-MB-231 showed higher uptake of FA-capped Au NCs than FR-absence cell lines A549, but lacking an good understanding of the uptake mechanism.

iv) The *in vivo* studies will be executed. Targeted and non-targeted composites will be explored in mice bearing orthotropic tumors in the future.

References

1. Salata, O. V., Applications of nanoparticles in biology and medicine. *J. Nanobiotechnol.* **2004,** *2,* 3.

2. Pankhurst, Q. A.; Connolly, J.; Jones, S. K.; Dobson, J., Applications of magnetic nanoparticles in biomedicine. *J. Phys. D: Appl. Phys.* **2003,** *36*, R167.

3. Daniel, M.-C.; Astruc, D., Gold Nanoparticles: Assembly, Supramolecular Chemistry, Quantum-Size-Related Properties, and Applications toward Biology, Catalysis, and Nanotechnology. *Chem. Rev.* **2003,** *104*, 293-346.

4. Gupta, A. K.; Gupta, M., Synthesis and surface engineering of iron oxide nanoparticles for biomedical applications. *Biomaterials* **2005,** *26*, 3995-4021.

5. Mauter, M. S.; Elimelech, M., Environmental applications of carbon-based nanomaterials. *Environ. Sci. Technol.* **2008,** *42*, 5843-5859.

6. Royston, E.; Ghosh, A.; Kofinas, P.; Harris, M. T.; Culver, J. N., Self-assembly of virus-structured high surface area nanomaterials and their application as battery electrodes. *Langmuir* **2008,** *24*, 906-912.

7. Feynman, R. P., There's plenty of room at the bottom. *Eng. Sci.* **1960,** *23,* 22-36.

8. Laurent, S.; Forge, D.; Port, M.; Roch, A.; Robic, C.; Vander Elst, L.; Muller, R. N., Magnetic iron oxide nanoparticles: synthesis, stabilization, vectorization, physicochemical characterizations, and biological applications. *Chem. Rev.* **2010,** *110*, 2574-2574.

9. Ray, S. C.; Saha, A.; Jana, N. R.; Sarkar, R., Fluorescent carbon nanoparticles: synthesis, characterization, and bioimaging application. *J. Phys. Chem. C* **2009,** *113*, 18546-18551.

10. Kelly, K. L.; Coronado, E.; Zhao, L. L.; Schatz, G. C., The Optical Properties of Metal Nanoparticles: The Influence of Size, Shape, and Dielectric Environment. *J. Phys. Chem. B* **2002,** *107*, 668-677.

11. Vollath, D.; Szabó, D. V.; Hauβelt, J., Synthesis and properties of ceramic nanoparticles and nanocomposites. *J*. *Eur*. *Ceram*. *Soc*. **1997,** *17*, 1317-1324.

12. Alivisatos, A. P., Semiconductor clusters, nanocrystals, and quantum dots. *Science* **1996,** *271*, 933-937.

13. Kumari, A.; Yadav, S. K.; Yadav, S. C., Biodegradable polymeric nanoparticles based drug delivery systems. *Colloids Surf*. *B*. *Biointerfaces* **2010,** *75*, 1-18.

14. Wang, Y.; Xia, Y., Bottom-up and top-down approaches to the synthesis of monodispersed spherical colloids of low melting-point metals. *Nano Lett.* **2004,** *4*, 2047-2050.

15. Iravani, S., Green synthesis of metal nanoparticles using plants. *Green Chem.* **2011,** *13*, 2638-2650.

16. Yeh, Y.-C.; Creran, B.; Rotello, V. M., Gold nanoparticles: preparation, properties, and applications in bionanotechnology. *Nanoscale* **2012,** *4*, 1871-1880.

17. Zhu, M.; Lanni, E.; Garg, N.; Bier, M. E.; Jin, R., Kinetically Controlled, High-Yield Synthesis of Au25 Clusters. *J. Am. Chem. Soc.* **2008,** *130*, 1138-1139.

18. Tseng, R. J.; Huang, J.; Ouyang, J.; Kaner, R. B.; Yang, Polyaniline nanofiber/gold nanoparticle nonvolatile memory. *Nano Lett.* **2005,** *5*, 1077-1080.

19. Radić, N.; Obradović, B. M.; Kostić, M.; Dojčinović, B.; Hudcová, M.; Kuraica, M. M.; Černák, M., Deposition of gold nanoparticles on polypropylene nonwoven pretreated by dielectric barrier discharge and diffuse coplanar surface barrier discharge. *Plasma Chem*. *Plasma Process*. **2013,** *33*, 201-218.

20. Faraday, M., The Bakerian Lecture: Experimental Relations of Gold (and Other Metals) to Light. *Philos*. *Trans*. *R*. *Soc*. *London* **1857,** *147*, 145-181.

21. Moirangthem, R. S.; Yaseen, M. T.; Wei, P.-K.; Cheng, J.-Y.; Chang, Y.-C., Enhanced localized plasmonic detections using partially-embedded gold nanoparticles and ellipsometric measurements. *Biomed*. *Opt*. *Express* **2012,** *3*, 899-910.

22. Wu, Z.; Suhan, J.; Jin, R., One-pot synthesis of atomically monodisperse, thiol-

functionalized Au-25 nanoclusters. *J. Mater. Chem.* **2009,** *19*, 622-626.

23. Teo, B. K.; Sloane, N. J. A., Magic numbers in polygonal and polyhedral clusters. *Inorg. Chem.* **1985,** *24*, 4545-4558.

24. Knight, W. D.; Clemenger, K.; de Heer, W. A.; Saunders, W. A.; Chou, M. Y.; Cohen, M. L., Electronic Shell Structure and Abundances of Sodium Clusters. *Phys. Rev. Lett.* **1984,** *52*, 2141-2143.

25. Häkkinen, H., Electronic shell structures in bare and protected metal nanoclusters. *Adv. Phys.: X* **2016,** *1*, 467-491.

26. Mori, T.; Hegmann, T., Determining the composition of gold nanoparticles: a compilation of shapes, sizes, and calculations using geometric considerations. *J. Nanopart. Res.* **2016,** *18*, 295.

27. Li, H.; Li, L.; Pedersen, A.; Gao, Y.; Khetrapal, N.; Jónsson, H.; Zeng, X. C., Magic-number gold nanoclusters with diameters from 1 to 3.5 nm: relative stability and catalytic activity for CO oxidation. *Nano Lett.* **2015,** *15*, 682-688.

28. Lopez-Acevedo, O.; Tsunoyama, H.; Tsukuda, T.; Hakkinen, H.; Aikens, C. M., Chirality and electronic structure of the thiolate-protected Au-38 nanocluster. *J. Am. Chem. Soc.* **2010,** *132*, 8210-8218.

29.Gautier, C.; Bürgi, T., Chiral Inversion of Gold Nanoparticles. *J. Am. Chem. Soc.* **2008,** *130*, 7077-7084.

30. Shang, L.; Azadfar, N.; Stockmar, F.; Send, W.; Trouillet, V.; Bruns, M.; Gerthsen, D.; Nienhaus, G. U., One-pot synthesis of near-infrared fluorescent gold clusters for cellular fluorescence lifetime imaging. *Small* **2011,** *7*, 2614-2620.

31. Yang, Y.; Chen, S., Surface Manipulation of the Electronic Energy of Subnanometer-Sized Gold Clusters: An Electrochemical and Spectroscopic Investigation. *Nano Lett.* **2003,** *3*, 75-79.

32. Shang, L.; Nienhaus, G. U., Gold nanoclusters as novel optical probes for in vitro and in vivo fluorescence imaging. *Biophys. Rev.* **2012,** *4*, 313-322.

33. Huang, X.; Luo, Y.; Li, Z.; Li, B.; Zhang, H.; Li, L.; Majeed, I.; Zou, P.; Tan, B., Biolabeling Hematopoietic System Cells Using Near-Infrared Fluorescent Gold Nanoclusters. *J*. *Phys*. *Chem*. *C* **2011,** *115*, 16753-16763.

34. Liu, C.-L.; Liu, T.-M.; Hsieh, T.-Y.; Liu, H.-W.; Chen, Y.-S.; Tsai, C.-K.; Chen, H.-C.; Lin, J.-W.; Hsu, R.-B.; Wang, T.-D.; Chen, C.-C.; Sun, C.-K.; Chou, P.-T., Gold nanodots: in vivo metabolic imaging of insulin with multiphoton fluorescence of human insulin–Au nanodots *Small* **2013,** *9*, 2102-2102.

35. Crespo, P.; Litrán, R.; Rojas, T. C.; Multigner, M.; de la Fuente, J. M.; Sánchez-López, J. C.; García, M. A.; Hernando, A.; Penadés, S.; Fernández, A., Permanent Magnetism, Magnetic Anisotropy, and Hysteresis of Thiol-Capped Gold Nanoparticles. *Phys. Rev. Lett.* **2004,** *93*, 087204.

36. Li, G.; Jin, R., Atomically precise gold nanoclusters as new model catalysts. *Acc*. *Chem*. *Res*. **2013,** *46*, 1749-1758.

37. Wang, J.; Zhang, G.; Li, Q.; Jiang, H.; Liu, C.; Amatore, C.; Wang, X., In vivo self-bio-imaging of tumors through in situ biosynthesized fluorescent gold nanoclusters. *Sci. Rep.* **2013,** *3*, 1157.

38. Govindaraju, S.; Ankireddy, S. R.; Viswanath, B.; Kim, J.; Yun, K., Fluorescent gold nanoclusters for selective detection of dopamine in cerebrospinal fluid. *Sci. Rep.* **2017,** *7*, 40298.

39. Cai, B.; Jia, B.; Shi, Z.; Gu, M., Near-field light concentration of ultra-small metallic nanoparticles for absorption enhancement in a-Si solar cells. *Appl*. *Phys*. *Lett*. **2013,** *102*, 093107.

40. Chen, Y.-S.; Choi, H.; Kamat, P. V., Metal-cluster-sensitized solar cells. A new class of thiolated gold sensitizers delivering efficiency greater than 2%. *J*. *Am*. *Chem*. *Soc*. **2013,** *135*, 8822-8825.

41. White, S. B.; Kim, D.-H.; Guo, Y.; Li, W.; Yang, Y.; Chen, J.; Gogineni, V. R.; Larson, A. C., Biofunctionalized Hybrid Magnetic Gold Nanoparticles as Catalysts for Photothermal Ablation of Colorectal Liver Metastases. *Radiology* **2017,** *285*, 809-819.

42. Giepmans, B. N. G.; Adams, S. R.; Ellisman, M. H.; Tsien, R. Y., The Fluorescent Toolbox for Assessing Protein Location and Function. *Science* **2006,** *312*, 217-224.

43. Wiedenmann, J.; Nienhaus, G. U., Live-cell imaging with EosFP and other photoactivatable marker proteins of the GFP family. *Expert Rev*. *Proteomics* **2006,** *3*, 361-374.

44. Resch-Genger, U.; Grabolle, M.; Cavaliere-Jaricot, S.; Nitschke, R.; Nann, T., Quantum dots versus organic dyes as fluorescent labels. *Nat. Meth.* **2008,** *5*, 763-775.

45. Nienhaus, G. U.; Wiedenmann, J., Structure, Dynamics and Optical Properties of Fluorescent Proteins: Perspectives for Marker Development. *ChemPhysChem* **2009,** *10*, 1369-1379.

46. Bakueva, L.; Gorelikov, I.; Musikhin, S.; Zhao, X. S.; Sargent, E. H.; Kumacheva, E., PbS quantum dots with stable efficient luminescence in he near-IR sperctral range. *Adv. Mater.* **2004,** *16*, 926-929.

47. Kim, J. S.; Cho, K. J.; Tran, T. H.; Nurunnabi, M.; Moon, T. H.; Hong, S. M.; Lee, Y.-k., In vivo NIR imaging with CdTe/CdSe quantum dots entrapped in PLGA nanospheres. *J. Colloid Interface Sci.* **2011,** *353*, 363-371.

48. Deng, H.-H.; Shi, X.-Q.; Wang, F.-F.; Peng, H.-P.; Liu, A.-L.; Xia, X.-H.; Chen, W., Fabrication of water-Soluble, green-emitting gold nanoclusters with a 65% photoluminescence quantum yield via host–guest recognition. *Chem. Mater.* **2017,** *29*, 1362-1369.

49. Link, S.; Beeby, A.; FitzGerald, S.; El-Sayed, M. A.; Schaaff, T. G.; Whetten, R. L., Visible to infrared luminescence from a 28-atom gold cluster. *J. Phys. Chem. B* **2002,** *106*, 3410-3415.

50. Shang, L.; Dong, S.; Nienhaus, G. U., Ultra-small fluorescent metal nanoclusters: synthesis and biological applications. *Nano Today* **2011,** *6*, 401-418.

51. Wu, X.; He, X.; Wang, K.; Xie, C.; Zhou, B.; Qing, Z., Ultrasmall near-infrared

gold nanoclusters for tumor fluorescence imaging in vivo. *Nanoscale* **2010,** *2*, 2244-2249.

52. Leifert, A.; Pan-Bartnek, Y.; Simon, U.; Jahnen-Dechent, W., Molecularly stabilised ultrasmall gold nanoparticles: synthesis, characterization and bioactivity. *Nanoscale* **2013,** *5*, 6224-6242.

53. Ke, C.-Y.; Chen, T.-H.; Lu, L.-C.; Tseng, W.-L., Understanding thiol-induced etching of luminescent gold nanoclusters. *RSC Adv.* **2014,** *4*, 26050-26056.

54. Zeng, C.; Chen, Y.; Li, G.; Jin, R., Magic Size Au-64(S-c-C6H11)(32) Nanocluster Protected by Cyclohexanethiolate. *Chem. Mater.* **2014,** *26*, 2635-2641.

55. Duan, H.; Nie, S., Etching colloidal gold nanocrystals with hyperbranched and multivalent polymers: a new route to fluorescent and water-soluble atomic clusters. *J. Am. Chem. Soc.* **2007,** *129*, 2412-2413.

56. Jana, N. R.; Gearheart, L.; Murphy, C. J., Seeding Growth for Size Control of 5−40 nm Diameter Gold Nanoparticles. *Langmuir* **2001,** *17*, 6782-6786.

57. Israelsen, N. D.; Hanson, C.; Vargis, E., Nanoparticle properties and synthesis effects on surface-enhanced raman scattering enhancement factor: an introduction. *Sci. World J.* **2015,** *2015*, 124582.

58. Brust, M.; Walker, M.; Bethell, D.; Schiffrin, D. J.; Whyman, R., Synthesis of thiol-derivatised gold nanoparticles in a two-phase Liquid-Liquid system. *J. Chem. Soc., Chem. Commun.* **1994,** 801-802.

59. Brust, M.; Fink, J.; Bethell, D.; Schiffrin, D. J.; Kiely, C., Synthesis and reactions of functionalised gold nanoparticles. *J. Chem. Soc., Chem. Commun.* **1995,** *0*, 1655-1656.

60. Zhu, X.; Jin, S.; Wang, S.; Meng, X.; Zhu, C.; Zhu, M.; Jin, R., One-Pot Synthesis of Phenylmethanethiolate-Protected Au-20(SR)(16) and Au-24(SR)(20) Nanoclusters and Insight into the Kinetic Control. *Chem. - Asian J.* **2013,** *8*, 2739-2745.

61. Zhu, M.; Qian, H.; Jin, R., Thiolate-Protected Au-24(SC2H4Ph)(20) Nanoclusters: Superatoms or Not? *J*. *Phys*. *Chem*. *Lett*. **2010,** *1*, 1003-1007.

62. Kumar, S.; Jin, R., Water-soluble Au-25(Capt)(18) nanoclusters: synthesis, thermal stability, and optical properties. *Nanoscale* **2012,** *4*, 4222-4227.

63. Chevrier, D. M.; Chatt, A.; Zhang, P.; Zeng, C.; Jin, R., Unique Bonding Properties of the Au-36(SR)(24) Nanocluster with FCC-Like Core. *J*. *Phys*. *Chem*. *Lett*. **2013,** *4*, 3186-3191.

64. MacDonald, M. A.; Zhang, P.; Chen, N.; Qian, H.; Jin, R., Solution-Phase Structure and Bonding of Au-38(SR)(24) Nanoclusters from X-ray Absorption Spectroscopy. *J. Phys. Chem. C* **2011,** *115*, 65-69.

65. Zeng, C.; Chen, Y.; Li, G.; Jin, R., Synthesis of a Au-44(SR)(28) nanocluster: structure prediction and evolution from Au-28(SR)(20), Au-36(SR)(24) to Au-44(SR)(28). *Chem*. *Commun*. **2014,** *50*, 55-57.

66. Qian, H.; Jin, R., Ambient Synthesis of Au-144(SR)(60) Nanoclusters in Methanol. *Chem. Mater.* **2011,** *23*, 2209-2217.

67. Qian, H.; Jin, R., Synthesis and electrospray mass spectrometry determination of thiolate-protected Au-55(SR)(31) nanoclusters. *Chem*. *Commun*. **2011,** *47*, 11462-11464.

68. Ohta, T.; Shibuta, M.; Tsunoyama, H.; Negishi, Y.; Eguchi, T.; Nakajima, A., Size and structure dependence of electronic states in thiolate-protected gold nanoclusters of Au25(SR)18, Au38(SR)24, and Au144(SR)60. *J*. *Phys*. *Chem*. *C* **2013,** *117*, 3674- 3679.

69. McPartlin, M.; Mason, R.; Malatesta, L., Novel cluster complexes of gold(0)-gold(I). *J*. *Chem*. *Soc*. *D* **1969,** *0*, 334-334.

70. Mingos, D. M. P., Molecular-orbital calculations on cluster compounds of gold. *J*. *Chem*. *Soc*., *Dalton Trans*. **1976,** *0*, 1163-1169.

71. Briant, C. E.; Theobald, B. R. C.; White, J. W.; Bell, L. K.; Mingos, D. M. P.; Welch, A. J., Synthesis and X-ray structural characterization of the centred icosahedral gold cluster compound [Aul3(PMe2Ph)10Cl2](PF6)3; the realization of a theoretical prediction. *J*. *Chem*. *Soc*., *Chem*. *Commun*. **1981,** *0*, 201-202.

72. Shichibu, Y.; Negishi, Y.; Watanabe, T.; Chaki, N. K.; Kawaguchi, H.; Tsukuda, T., Biicosahedral gold clusters Au-25(PPh3)(10)(SCnH2n+1)(5)Cl-2 (2+) (n=2-18): A stepping stone to cluster-assembled materials. *J*. *Phys*. *Chem*. *C* **2007,** *111*, 7845-7847.

73. Shichibu, Y.; Konishi, K., HCl-Induced Nuclearity Convergence in Diphosphine-Protected Ultrasmall Gold Clusters: A Novel Synthetic Route to "Magic-Number" Au13 Clusters. *Small* **2010,** *6*, 1216-1220.

74. Pettibone, J. M.; Hudgens, J. W., Synthetic Approach for Tunable, Size-Selective Formation of Monodisperse, Diphosphine-Protected Gold Nanoclusters. *J*. *Phys*. *Chem*. *Lett*. **2010,** *1*, 2536-2540.

75. Si Kae, J.; Chen, Y.; Shi, Q.; Cheng, W., Nanoparticle superlattices: the roles of soft ligands. *Adv*. *Sci*. *(Weinheim, Ger.)* **2017,** *5*, 1700179.

76. Nguyen, D. H.; Lee, J. S.; Choi, J. H.; Park, K. M.; Lee, Y.; Park, K. D., Hierarchical self-assembly of magnetic nanoclusters for theranostics: Tunable size, enhanced magnetic resonance imagability, and controlled and targeted drug delivery. *Acta Biomater.* **2016,** *35*, 109-117.

77. Zhang, X.-D.; Luo, Z.; Chen, J.; Wang, H.; Song, S.-S.; Shen, X.; Long, W.; Sun, Y.-M.; Fan, S.; Zheng, K.; Leong, D. T.; Xie, J., Storage of gold nanoclusters in muscle leads to their biphasic in vivo clearance. *Small* **2014,** *11*, 1683-1690.

78. Que, Y.; Feng, C.; Zhang, S.; Huang, X., Stability and catalytic activity of PEG-b-PS-capped gold nanoparticles: a matter of PS chain length. *J*. *Phys*. *Chem*. *C* **2015,** *119*, 1960-1970.

79. Kolate, A.; Baradia, D.; Patil, S.; Vhora, I.; Kore, G.; Misra, A., PEG — A versatile conjugating ligand for drugs and drug delivery systems. *J*. *Controlled Release* **2014,** *192*, 67-81.

80. Knop, K.; Hoogenboom, R.; Fischer, D.; Schubert Ulrich , S., Poly(ethylene glycol) in drug delivery: pros and cons as well as potential alternatives. *Angew*. *Chem*. *Int*. *Ed*. **2010,** *49*, 6288-6308.

81. Qin, A.; Fu, L. T.; Wong, J. K. F.; Chau, L. Y.; Yip, S. P.; Lee, T. M. H., Precipitation of PEG/carboxyl-modified gold nanoparticles with magnesium pyrophosphate: a new platform for real-time monitoring of loop-mediated isothermal amplification. *ACS Appl*. *Mater*. *Interfaces* **2017,** *9*, 10472-10480.

82. Dutta, N.; Dutta, A.; Roy Choudhury, N., Gold Nanoparticles and Fluorescent Proteins, Optically Coupled Hybrid Architectures. In *Encyclopedia of Metalloproteins*, Kretsinger, R.; Uversky, V.; Permyakov, E., Eds. Springer New York: 2013; 895-908.

83. Xie, J.; Zheng, Y.; Ying, J. Y., Protein-Directed Synthesis of Highly Fluorescent Gold Nanoclusters. *J. Am. Chem. Soc.* **2009,** *131*, 888-889.

84. Tam, N. C. M.; McVeigh, P. Z.; MacDonald, T. D.; Farhadi, A.; Wilson, B. C.; Zheng, G., Porphyrin–lipid stabilized gold nanoparticles for surface enhanced raman scattering based imaging. *Bioconj*. *Chem*. **2012,** *23*, 1726-1730.

85. Munro, C. J.; Knecht, M. R., Solution effects on peptide-mediated reduction and stabilization of Au nanoparticles. *Langmuir* **2017,** *33*, 13757-13765.

86. Katti, K. K.; Kattumuri, V.; Bhaskaran, S.; Katti, K. V.; Kannan, R., Facile and general method for synthesis of sugar coated gold nanoparticles. *Int*. *J*. *Green Nanotechnol*. **2009,** *1*, B53-B59.

87. Leng, Y.; Fu, L.; Ye, L.; Li, B.; Xu, X.; Xing, X.; He, J.; Song, Y.; Leng, C.; Guo, Y.; Ji, X.; Lu, Z., Protein-directed synthesis of highly monodispersed, spherical gold nanoparticles and their applications in multidimensional sensing. *Sci*. *Rep*. **2016,** *6*, 28900.

88. Stine, K. J., Enzyme immobilization on nanoporous gold: a review. *Biochem*. *Insights* **2017,** *10*, 1-12.

89. Shin, J.; Zhang, X.; Liu, J., DNA-functionalized gold nanoparticles in macromolecularly crowded polymer solutions. *J*. *Phys*. *Chem*. *B* **2012,** *116*, 13396-13402.

90. Haiss, W.; Thanh, N. T. K.; Aveyard, J.; Fernig, D. G., Determination of Size and Concentration of Gold Nanoparticles from UV−Vis Spectra. *Anal. Chem.* **2007,** *79*, 4215-4221.

91. Cui, M.; Zhao, Y.; Song, Q., Synthesis, optical properties and applications of ultra-small luminescent gold nanoclusters. *Trends Anal*. *Chem*. **2014,** *57*, 73-82.

92. Zhou, M.; Zeng, C.; Chen, Y.; Zhao, S.; Sfeir, M. Y.; Zhu, M.; Jin, R., Evolution from the plasmon to exciton state in ligand-protected atomically precise gold nanoparticles. *Nat*. *Commun*. **2016,** *7*, 13240.

93. Tsukuda, T., Toward an Atomic-Level Understanding of Size-Specific Properties of Protected and Stabilized Gold Clusters. *Bull. Chem. Soc. Jpn.* **2012,** *85*, 151-168.

94. Chen, L.-Y.; Wang, C.-W.; Yuan, Z.; Chang, H.-T., Fluorescent Gold Nanoclusters: Recent Advances in Sensing and Imaging. *Anal. Chem.* **2014,** *87*, 216-229.

95. Jin, R.; Zeng, C.; Zhou, M.; Chen, Y., Atomically Precise Colloidal Metal Nanoclusters and Nanoparticles: Fundamentals and Opportunities. *Chem. Rev.* **2016,** *116*, 10346-10413.

96. Martin, M. N.; Li, D.; Dass, A.; Eah, S.-K., Ultrafast, 2 min synthesis of monolayer-protected gold nanoclusters ($d < 2$ nm). *Nanoscale* **2012,** *4*, 4091-4094.

97. Roduner, E., Size matters: why nanomaterials are different. *Chem*. *Soc*. *Rev*. **2006,** *35*, 583-592.

98.Qin, W.; Lohrman, J.; Ren, S., Magnetic and optoelectronic properties of gold nanocluster–thiophene assembly. *Angew*. *Chem*. *Int*. *Ed*. **2014,** *53*, 7316-7319.

99. Qu, X.; Li, Y.; Li, L.; Wang, Y.; Liang, J.; Liang, J., Fluorescent Gold

Nanoclusters: Synthesis and Recent Biological Application. *J. Nanomater.* **2015,** *2015*, 23.

100. Schaeffer, N.; Tan, B.; Dickinson, C.; Rosseinsky, M. J.; Laromaine, A.; McComb, D. W.; Stevens, M. M.; Wang, Y.; Petit, L.; Barentin, C.; Spiller, D. G.; Cooper, A. I.; Levy, R., Fluorescent or not? Size-dependent fluorescence switching for polymer-stabilized gold clusters in the 1.1-1.7 nm size range. *Chem*. *Commun*. **2008,** *0*, 3986- 3988.

101. Apell, P.; Monreal, R.; Lundqvist, S., Photoluminescence of noble metals. *Phys*. *Scr*. **1988,** *38*, 174.

102. Huang, T.; Murray, R. W., Visible luminescence of water-soluble monolayer-protected gold clusters. *J. Phys. Chem. B* **2001,** *105*, 12498-12502.

103. Venkatesh, V.; Shukla, A.; Sivakumar, S.; Verma, S., Purine-stabilized green fluorescent gold nanoclusters for cell nuclei imaging applications. *ACS Appl*. *Mater*. *Interfaces* **2014,** *6*, 2185-2191.

104. Lin, C.-A. J.; Yang, T.-Y.; Lee, C.-H.; Huang, S. H.; Sperling, R. A.; Zanella, M.; Li, J. K.; Shen, J.-L.; Wang, H.-H.; Yeh, H.-I.; Parak, W. J.; Chang, W. H., Synthesis, Characterization, and Bioconjugation of Fluorescent Gold Nanoclusters toward Biological Labeling Applications. *ACS Nano* **2009,** *3*, 395-401.

105. Dulkeith, E.; Morteani, A. C.; Niedereichholz, T.; Klar, T. A.; Feldmann, J.; Levi, S. A.; van Veggel, F. C. J. M.; Reinhoudt, D. N.; Möller, M.; Gittins, D. I., Fluorescence Quenching of Dye Molecules near Gold Nanoparticles: Radiative and Nonradiative Effects. *Phys. Rev. Lett.* **2002,** *89*, 203002.

106. Chompoosor, A.; Han, G.; Rotello, V. M., Charge Dependence of Ligand Release and Monolayer Stability of Gold Nanoparticles by Biogenic Thiols. *Bioconj. Chem.* **2008,** *19*, 1342-1345.

107. Ding, W.; Liu, Y.; Li, Y.; Shi, Q.; Li, H.; Xia, H.; Wang, D.; Tao, X., Water-soluble gold nanoclusters with pH-dependent fluorescence and high colloidal stability over a wide pH range via co-reduction of glutathione and citrate. *RSC Adv.* **2014,** *4*, 22651-

22659.

108. Tamura, M.; Fujihara, H., Chiral Bisphosphine BINAP-Stabilized Gold and Palladium Nanoparticles with Small Size and Their Palladium Nanoparticle-Catalyzed Asymmetric Reaction. *J. Am. Chem. Soc.* **2003,** *125*, 15742-15743.

109. Boyen, H.-G.; Kästle, G.; Weigl, F.; Koslowski, B.; Dietrich, C.; Ziemann, P.; Spatz, J. P.; Riethmüller, S.; Hartmann, C.; Möller, M.; Schmid, G.; Garnier, M. G.; Oelhafen, P., Oxidation-Resistant Gold-55 Clusters. *Science* **2002,** *297*, 1533-1536.

110. Karakoti, A. S.; Das, S.; Thevuthasan, S.; Seal, S., PEGylated Inorganic Nanoparticles. *Angew*. *Chem*. *Int*. *Ed*. **2011,** *50*, 1980-1994.

111. Garitaonandia, J. S.; Insausti, M.; Goikolea, E.; Suzuki, M.; Cashion, J. D.; Kawamura, N.; Ohsawa, H.; Gil de Muro, I.; Suzuki, K.; Plazaola, F.; Rojo, T., Chemically induced permanent magnetism in Au, Ag, and Cu nanoparticles: localization of the magnetism by element selective techniques. *Nano Lett.* **2008,** *8*, 661-667.

112. Trudel, S., Unexpected magnetism in gold nanostructures: making gold even more attractive. *Gold Bull.* **2011,** *44*, 3-13.

113. Zhu, M.; Aikens, C. M.; Hendrich, M. P.; Gupta, R.; Qian, H.; Schatz, G. C.; Jin, R., Reversible Switching of Magnetism in Thiolate-Protected Au-25 Superatoms. *J. Am. Chem. Soc.* **2009,** *13*, 2490-+.

114. Venzo, A.; Antonello, S.; Gascón, J. A.; Guryanov, I.; Leapman, R. D.; Perera, N. V.; Sousa, A.; Zamuner, M.; Zanella, A.; Maran, F., Effect of the Charge State (z = −1, 0, +1) on the Nuclear Magnetic Resonance of Monodisperse Au25[S(CH2)2Ph]18z Clusters. *Anal. Chem.* **2011,** *83*, 6355-6362.

115. Antonello, S.; Perera, N. V.; Ruzzi, M.; Gascón, J. A.; Maran, F., Interplay of Charge State, Lability, and Magnetism in the Molecule-like Au25(SR)18 Cluster. *J. Am. Chem. Soc.* **2013,** *135*, 15585-15594.

116. Nealon, G. L.; Donnio, B.; Greget, R.; Kappler, J.-P.; Terazzi, E.; Gallani, J.-L., Magnetism in gold nanoparticles. *Nanoscale* **2012,** *4*, 5244-5258.

117.Negishi, Y.; Tsunoyama, H.; Suzuki, M.; Kawamura, N.; Matsushita, M. M.; Maruyama, K.; Sugawara, T.; Yokoyama, T.; Tsukuda, T., X-ray magnetic circular dichroism of size-selected, thiolated gold clusters. *J*. *Am*. *Chem*. *Soc*. **2006,** *128*, 12034-12035.

118.Yamamoto, Y.; Miura, T.; Suzuki, M.; Kawamura, N.; Miyagawa, H.; Nakamura, T.; Kobayashi, K.; Teranishi, T.; Hori, H., Direct Observation of Ferromagnetic Spin Polarization in Gold Nanoparticles. *Phys. Rev. Lett.* **2004,** *93*, 116801.

119.Li, C.-Y.; Karna, S. K.; Wang, C.-W.; Li, W.-H., Spin polarization and quantum spins in Au nanoparticles. *Int*. *J*. *Mol*. *Sci*. **2013,** *14*, 17618-17642.

120. Ayuela, A.; Crespo, P.; García, M. A.; Hernando, A.; Echenique, P. M., sp magnetism in clusters of gold thiolates. *New J*. *Phy*. **2012,** *14*, 013064.

121. Lewinski, N.; Colvin, V.; Drezek, R., Cytotoxicity of nanoparticles. *Small* **2008,** *4*, 26-49.

122. Wu, Y. L.; Putcha, N.; Ng, K. W.; Leong, D. T.; Lim, C. T.; Loo, S. C. J.; Chen, X. D., Biophysical Responses upon the Interaction of Nanomaterials with Cellular Interfaces. *Acc. Chem. Res.* **2013,** *46*, 782-791.

123. Albanese, A.; Tang, P. S.; Chan, W. C. W., The effect of nanoparticle size, shape, and surface chemistry on biological systems. *Annu*. *Rev*. *Biomed*. *Eng*. **2012,** *14*, 1-16.

124. Monopoli, M. P.; Åberg, C.; Salvati, A.; Dawson, K. A., Biomolecular coronas provide the biological identity of nanosized materials. *Nat*. *Nanotechnol*. **2012,** *7*, 779.

125. Murugan, K.; Choonara, Y. E.; Kumar, P.; Bijukumar, D.; du Toit, L. C.; Pillay, V., Parameters and characteristics governing cellular internalization and trans-barrier trafficking of nanostructures. *Int*. *J*. *Nanomed*. **2015,** *10*, 2191-2206.

126. Shang, L.; Nienhaus, K.; Jiang, X.; Yang, L.; Landfester, K.; Mailänder, V.; Simmet, T.; Nienhaus, G. U., Nanoparticle interactions with live cells: quantitative fluorescence microscopy of nanoparticle size effects. *Beilstein J*. *Nanotechnol*. **2014,** *5*, 2388-2397.

127. Wang, T.; Bai, J.; Jiang, X.; Nienhaus, G. U., Cellular uptake of nanoparticles by membrane penetration: a study combining confocal microscopy with FTIR spectroelectrochemistry. *ACS Nano* **2012,** *6*, 1251-1259.

128. Yau, S. H.; Varnavski, O.; Goodson, T., An Ultrafast Look at Au Nanoclusters. *Acc. Chem. Res.* **2013,** *46*, 1506-1516.

129. Chakraborty, I.; Pradeep, T., Atomically Precise Clusters of Noble Metals: Emerging Link between Atoms and Nanoparticles. *Chem. Rev.* **2017,** *117*, 8208-8271.

130. Yu, Q.; Gao, P.; Zhang, K. Y.; Tong, X.; Yang, H.; Liu, S.; Du, J.; Zhao, Q.; Huang, W., Luminescent gold nanocluster-based sensing platform for accurate H2S detection in vitro and in vivo with improved anti-interference. *Light: Sci. Appl.* **2017,** *6*, e17107.

131. Grüner, F.; Blumendorf, F.; Schmutzler, O.; Staufer, T.; Bradbury, M.; Wiesner, U.; Rosentreter, T.; Loers, G.; Lutz, D.; Richter, B.; Fischer, M.; Schulz, F.; Steiner, S.; Warmer, M.; Burkhardt, A.; Meents, A.; Kupinski, M.; Hoeschen, C., Localising functionalised gold-nanoparticles in murine spinal cords by X-ray fluorescence imaging and background-reduction through spatial filtering for human-sized objects. *Sci. Rep.* **2018,** *8*, 16561.

132. Kim, C. S.; Li, X.; Jiang, Y.; Yan, B.; Tonga, G. Y.; Ray, M.; Solfiell, D. J.; Rotello, V. M., Cellular imaging of endosome entrapped small gold nanoparticles. *MethodsX* **2015,** *2*, 306-315.

133. Li, K., Investigation on cellular uptake of gold nanoparticles by multiphoton laser scanning microscopy. Ph.D, Saarland University, **2013**.

134. Lin, C.-A. J.; Lee, C.-H.; Hsieh, J.-T.; Wang, H.-H.; Li, J. K.; Shen, J.-L.; Chan, W.-H.; Yeh, H.-I.; Chang, W. H., Review: Synthesis of fluorescent metallic nanoclusters toward biomedical application: recent progress and present challenges. *J. Med. Biol. Eng.* **2009,** *29*, 276-283.

135. Shaheen, U.; Cesbron, Y.; Violaine, S., Gold nanoparticles delivery in mammalian live cells: a critical review. *Nano Rev.* **2010,** *1*, 4889.

136. Pruteanu, M.; Neher, S. B.; Baker, T. A., Ligand-controlled proteolysis of the escherichia coli transcriptional regulator ZntR. *J. Bacteriol*. **2007,** *189*, 3017-3025.

137. Shah, N. B.; Dong, J.; Bischof, J. C., Cellular uptake and nanoscale localization of gold nanoparticles in cancer using label-free confocal Raman microscopy. *Mol. Pharm.* **2010,** *8*, 176-184.

138. Mayhew, T. M.; Mühlfeld, C.; Vanhecke, D.; Ochs, M., A review of recent methods for efficiently quantifying immunogold and other nanoparticles using TEM sections through cells, tissues and organs. *Ann. Anat.* **2009,** *191*, 153-170.

139. Nativo, P.; Prior, I. A.; Brust, M., Uptake and intracellular fate of surface-modified gold nanoparticles. *ACS Nano* **2008,** *2*, 1639-1644.

140. Alkilany, A. M.; Nagaria, P. K.; Hexel, C. R.; Shaw, T. J.; Murphy, C. J.; Wyatt, M. D., Cellular uptake and cytotoxicity of gold nanorods: molecular origin of cytotoxicity and surface effects. *Small* **2009,** *5*, 701-708.

141. Alkilany, A. M.; Murphy, C. J., Gold nanoparticles with a polymerizable surfactant bilayer: synthesis, polymerization, and stability evaluation. *Langmuir* **2009,** *25*, 13874-13879.

142. Liu, Y.; Shipton, M. K.; Ryan, J.; Kaufman, E. D.; Franzen, S.; Feldheim, D. L., Synthesis, stability, and cellular internalization of gold nanoparticles containing mixed peptide-poly (ethylene glycol) monolayers. *Anal. Chem.* **2007,** *79*, 2221-2229.

143. Cho, E. C.; Xie, J.; Wurm, P. A.; Xia, Y., Understanding the role of surface charges in cellular adsorption versus internalization by selectively removing gold nanoparticles on the cell surface with a I2/KI etchant. *Nano Lett.* **2009,** *9*, 1080-1084.

144. Kim, C.; Agasti, S. S.; Zhu, Z.; Isaacs, L.; Rotello, V. M., Recognition-mediated activation of therapeutic gold nanoparticles inside living cells. *Nat Chem* **2010,** *2* (11), 962-966.

145. Hennig, A.; Bakirci, H.; Nau, W. M., Label-free continuous enzyme assays with macrocycle-fluorescent dye complexes. *Nat. Methods.* **2007,** *4*, 629-632.

146. Wang, J.; Liu, G., Imaging nano–bio interactions in the kidney: Toward a better

understanding of nanoparticle clearance. *Angew. Chem. Int. Ed.* **2018,** *57*, 3008-3010.

147.Chithrani, B. D.; Chan, W. C. W., Elucidating the Mechanism of Cellular Uptake and Removal of Protein-Coated Gold Nanoparticles of Different Sizes and Shapes. *Nano Lett.* **2007,** *7*, 1542-1550.

148. Elnakat, H.; Ratnam, M., Distribution, functionality and gene regulation of folate receptor isoforms: implications in targeted therapy. *Adv. Drug Del. Rev.* **2004,** *56*, 1067-1084.

149. Tomassetti, A.; Mangiarotti, F.; Mazzi, M.; Sforzini, S.; Miotti, S.; Galmozzi, E.; Elwood, P. C.; Canevari, S., The variant hepatocyte nuclear factor 1 activates the P1 promoter of the human α-folate receptor gene in ovarian carcinoma. *Cancer Res.* **2003,** *63*, 696-704.

150. Danhier, F.; Feron, O.; Préat, V., To exploit the tumor microenvironment: Passive and active tumor targeting of nanocarriers for anti-cancer drug delivery. *J. Controlled Release* **2010,** *148*, 135-146.

151. Kelemen, L. E., The role of folate receptor alpha in cancer development, progression and treatment: Cause, consequence or innocent bystander? *Int. J. Cancer* **2006,** *119*, 243-250.

152. Jhaveri, M. S.; Rait, A. S.; Chung, K.-N.; Trepel, J. B.; Chang, E. H., Antisense oligonucleotides targeted to the human α folate receptor inhibit breast cancer cell growth and sensitize the cells to doxorubicin treatment. *Mol. Cancer Ther.* **2004,** *3*, 1505-1512.

153. Corona, G.; Giannini, F.; Fabris, M.; Toffoli, G.; Boiocchi, M., Role of folate receptor and reduced folate carrier in the transport of 5-methyltetrahydrofolic acid in human ovarian carcinoma cells. *Int. J. Cancer* **1998,** *75*, 125-133.

154. Rijnboutt, S.; Jansen, G.; Posthuma, G.; Hynes, J. B.; Schornagel, J. H.; Strous, G. J., Endocytosis of GPI-linked membrane folate receptor-alpha. *J. Cell Biol.* **1996,** *132*, 35-47.

155. Tian, J. W.; Luo, Y. P.; Huang, L. W.; Feng, Y. Q.; Ju, H. X.; Yu, B. Y., Pegylated

folate and peptide-decorated graphene oxide nanovehicle for in vivo targeted delivery of anticancer drugs and therapeutic self-monitoring. *Biosens. Bioelectron.* **2016,** *80*, 519-524.

156. Paulos, C. M.; Reddy, J. A.; Leamon, C. P.; Turk, M. J.; Low, P. S., Ligand Binding and Kinetics of Folate Receptor Recycling in Vivo: Impact on Receptor-Mediated Drug Delivery. *Mol. Pharmacol.* **2004,** *66*, 1406.

157. Luyckx, M.; Votino, R.; Squifflet, J.-L.; Baurain, J.-F., Profile of vintafolide (EC145) and its use in the treatment of platinum-resistant ovarian cancer. *Int. J. Women's Health* **2014,** *6*, 351-8.

158. O'Shannessy, D. J.; Somers, E. B.; Maltzman, J.; Smale, R.; Fu, Y.-S., Folate receptor alpha (FRA) expression in breast cancer: identification of a new molecular subtype and association with triple negative disease. *SpringerPlus* **2012,** *1*, 1-9.

159. O'Shannessy, D. J.; Yu, G.; Smale, R.; Fu, Y.-S.; Singhal, S.; Thiel, R. P.; Somers, E. B.; Vachani, A., Folate receptor alpha expression in lung cancer: diagnostic and prognostic significance. *Oncotarget* **2012,** *3*, 414-425.

160. Xin, W.; Feng, S.; Freisheim, J. H.; Gentry, L. E.; Ratnam, M., Differential stereospecificities and affinities of folate receptor isoforms for folate compounds and antifolates. *Biochem. Pharmacol.* **1992,** *44*, 1898-1901.

161. Antony, A. C., Folate receptors. *Annu. Rev. Nutr.* **1996,** *16*, 501-521.

162. He, Z.; Shi, Z.; Sun, W.; Ma, J.; Xia, J.; Zhang, X.; Chen, W.; Huang, J., Hemocompatibility of folic-acid-conjugated amphiphilic PEG-PLGA copolymer nanoparticles for co-delivery of cisplatin and paclitaxel: treatment effects for non-small-cell lung cancer. *Tumor Biol.* **2016,** *37*, 7809-7821.

163. Lei, D.; Yang, W.; Gong, Y. Q.; Jing, J.; Nie, H. L.; Yu, B.; Zhang, X. L., Non-covalent decoration of carbon dots with folic acid via a polymer-assisted strategy for fast and targeted cancer cell fluorescence imaging. *Sens. Actuator B-Chem.* **2016,** *230*, 714-720.

164. Chen, C.; Ke, J.; Zhou, X. E.; Yi, W.; Brunzelle, J. S.; Li, J.; Yong, E.-L.; Xu, H. E.; Melcher, K., Structural basis for molecular recognition of folic acid by folate receptors. *Nature* **2013,** *500*, 486-489.

165. Mornet, S.; Vasseur, S.; Grasset, F.; Duguet, E., Magnetic nanoparticle design for medical diagnosis and therapy. *J. Mater. Chem.* **2004,** *14* (14), 2161-2175.

166. Na, H. B.; Song, I. C.; Hyeon, T., Inorganic Nanoparticles for MRI Contrast Agents. *Adv. Mater.* **2009,** *21*, 2133-2148.

167. Jun, Y.-w.; Lee, J.-H.; Cheon, J., Chemical design of nanoparticle probes for high-performance magnetic resonance imaging. *Angew*. *Chem*. *Int*. *Ed*. **2008,** *47*, 5122-5135.

168. Jennings, L. E.; Long, N. J., 'Two is better than one'-probes for dual-modality molecular imaging. *Chem. Commun.* **2009,** 3511-3524.

169. Chavanpatil, M. D.; Khdair, A.; Panyam, J., Nanoparticles for Cellular Drug Delivery: Mechanisms and Factors Influencing Delivery. *J. Nanosci. Nanotechnol.* **2006,** *6*, 2651-2663.

170. Anzai, Y.; Piccoli, C. W.; Outwater, E. K.; Stanford, W.; Bluemke, D. A.; Nurenberg, P.; Saini, S.; Maravilla, K. R.; Feldman, D. E.; Schmiedl, U. P.; Brunberg, J. A.; Francis, I. R.; Harms, S. E.; Som, P. M.; Tempany, C. M., Evaluation of Neck and Body Metastases to Nodes with Ferumoxtran 10–enhanced MR Imaging: Phase III Safety and Efficacy Study. *Radiology* **2003,** *228*, 777-788.

171. Sun, C.; Lee, J. S. H.; Zhang, M., Magnetic Nanoparticles in MR Imaging and Drug Delivery. *Adv. Drug Del. Rev.* **2008,** *60*, 1252-1265.

172. Debouttière, P. J.; Roux, S.; Vocanson, F.; Billotey, C.; Beuf, O.; Favre-Réguillon, A.; Lin, Y.; Pellet-Rostaing, S.; Lamartine, R.; Perriat, P.; Tillement, O., Design of gold nanoparticles for magnetic resonance imaging. *Adv. Funct. Mater.* **2006,** *16*, 2330-2339.

173. Wust, P.; Hildebrandt, B.; Sreenivasa, G.; Rau, B.; Gellermann, J.; Riess, H.; Felix, R.; Schlag, P. M., Hyperthermia in combined treatment of cancer. *Lancet Oncol.*

2002, *3* (8), 487-497.

174. Zhang, W.; Guo, Z. Y.; Huang, D. Q.; Liu, Z. M.; Guo, X.; Zhong, H. Q., Synergistic effect of chemo-photothermal therapy using PEGylated graphene oxide. *Biomaterials* **2011,** *32*, 8555-8561.

175. O'Grady, N. P.; Barie, P. S.; Bartlett, J. G.; Bleck, T.; Garvey, G.; Jacobi, J.; Linden, P.; Maki, D. G.; Nam, M.; Pasculle, W., Practice guidelines for evaluating new fever in critically ill adult patients. *Clin. Infect. Dis.* **1998,** *26*, 1042-1059.

176. van der Zee, J., Heating the patient: a promising approach? *Ann. of oncol.* **2002,** *13*, 1173-1184.

177. Glazer, E. S.; Curley, S. A., The ongoing history of thermal therapy for cancer. *Surg. Oncol. Clin N. Am.* **2011,** *20*, 229-235.

178. Habash, R. W.; Bansal, R.; Krewski, D.; Alhafid, H. T., Thermal therapy, part 2: hyperthermia techniques. *CRC Crit. Rev. Bioeng.* **2006,** *34*, 491-542.

179. Hegyi, G.; Szigeti, G. P.; Szász, A., Hyperthermia versus oncothermia: cellular effects in complementary cancer therapy. *J. Evidence-Based Complementary Altern. Med.* **2013,** *2013*, 672873.

180. Takahashi, H.; Niidome, T.; Nariai, A.; Niidome, Y.; Yamada, S., Photothermal reshaping of gold nanorods prevents further cell death. *Nanotechnology* **2006,** *17*, 4431.

181. Oleson, J. R.; Samulski, T. V.; Leopold, K. A.; Clegg, S. T.; Dewhirst, M. W.; Dodge, R. K.; George, S. L., Sensitivity of hyperthermia trial outcomes to temperature and time: implications for thermal goals of treatment. *Int. J. Radiat. Oncol., Biol., Phys.* **1993,** *25*, 289-297.

182. Jaque, D.; Martinez Maestro, L.; del Rosal, B.; Haro-Gonzalez, P.; Benayas, A.; Plaza, J. L.; Martin Rodriguez, E.; Garcia Sole, J., Nanoparticles for photothermal therapies. *Nanoscale* **2014,** *6*, 9494-9530.

183. Habash, R. W.; Bansal, R.; Krewski, D.; Alhafid, H. T., Thermal therapy, Part III: ablation techniques. *CRC Crit*. *Rev*. *Bioeng*. **2007,** *35*, 37-121.

184. Habash, R. W.; Bansal, R.; Krewski, D.; Alhafid, H. T., Thermal therapy, part 1: an introduction to thermal therapy. *CRC Crit*. *Rev*. *Bioeng*. **2006,** *34*, 459-489.

185. Johannsen, M.; Thiesen, B.; Wust, P.; Jordan, A., Magnetic nanoparticle hyperthermia for prostate cancer. *Int*. *J*. *Hyperthermia* **2010,** *26*, 790-795.

186. Salloum, M.; Ma, R.; Weeks, D.; Zhu, L., Controlling nanoparticle delivery in magnetic nanoparticle hyperthermia for cancer treatment: experimental study in agarose gel. *Int*. *J*. *Hyperthermia* **2008,** *24*, 337-345.

187. Dewhirst, M.; Viglianti, B.; Lora-Michiels, M.; Hanson, M.; Hoopes, P., Basic principles of thermal dosimetry and thermal thresholds for tissue damage from hyperthermia. *Int*. *J*. *Hyperthermia* **2003,** *19*, 267-294.

188. Quesson, B.; de Zwart, J. A.; Moonen, C. T. W., Magnetic resonance temperature imaging for guidance of thermotherapy. *J. Magn. Reson. Imaging* **2000,** *12*, 525-533.

189. Thiesen, B.; Jordan, A., Clinical applications of magnetic nanoparticles for hyperthermia. *Int*. *J*. *Hyperthermia* **2008,** *24*, 467-474.

190. Ito, A.; Shinkai, M.; Honda, H.; Kobayashi, T., Medical application of functionalized magnetic nanoparticles. *J. Biosci. Bioeng.* **2005,** *100*, 1-11.

191. Gilchrist, R.; Medal, R.; Shorey, W. D.; Hanselman, R. C.; Parrott, J. C.; Taylor, C. B., Selective inductive heating of lymph nodes. *Ann. Surg.* **1957,** *146*, 596.

192. Johannsen, M.; Gneveckow, U.; Taymoorian, K.; Thiesen, B.; Waldöfner, N.; Scholz, R.; Jung, K.; Jordan, A.; Wust, P.; Loening, S., Morbidity and quality of life during thermotherapy using magnetic nanoparticles in locally recurrent prostate cancer: results of a prospective phase I trial. *Int*. *J*. *Hyperthermia* **2007,** *23*, 315-323.

193. Pissuwan, D.; Valenzuela, S. M.; Cortie, M. B., Therapeutic possibilities of plasmonically heated gold nanoparticles. *Trends Biotechnol.* **2006,** *24*, 62-67.

194. Smith, A. M.; Mancini, M. C.; Nie, S., Second window for in vivo imaging. *Nat.*

Nanotechnol. **2009,** *4*, 710.

195. Weissleder, R., A clearer vision for in vivo imaging. *Nat. Biotechnol.* **2001,** *19*, 316-317.

196. Albota, M. A.; Xu, C.; Webb, W. W., Two-photon fluorescence excitation cross sections of biomolecular probes from 690 to 960 nm. *Appl. Opt.* **1998,** *37*, 7352-7356.

197. Teeguarden, J. G.; Hinderliter, P. M.; Orr, G.; Thrall, B. D.; Pounds, J. G., Particokinetics in vitro: dosimetry considerations for in vitro nanoparticle toxicity assessments. *Toxicol. Sci.* **2007,** *95* (2), 300-312.

198. Nikolic, M. S.; Krack, M.; Aleksandrovic, V.; Kornowski, A.; Förster, S.; Weller, H., Tailor-Made Ligands for Biocompatible Nanoparticles. *Angew*. *Chem*. *Int*. *Ed*. **2006,** *45*, 6577-6580.

199. Jana, N. R.; Earhart, C.; Ying, J. Y., Synthesis of water-soluble and functionalized nanoparticles by silica coating. *Chem. Mater.* **2007,** *19*, 5074-5082.

200. Kang, X.; Guo, X.; Niu, X.; An, W.; Li, S.; Liu, Z.; Yang, Y.; Wang, N.; Jiang, Q.; Yan, C.; Wang, H.; Zhang, Q., Photothermal therapeutic application of gold nanorods-porphyrin-trastuzumab complexes in HER2-positive breast cancer. *Sci. Rep.* **2017,** *7*, 42069.

201. Kawashita, M.; Domi, S.; Saito, Y.; Aoki, M.; Ebisawa, Y.; Kokubo, T.; Saito, T.; Takano, M.; Araki, N.; Hiraoka, M., In vitro heat generation by ferrimagnetic maghemite microspheres for hyperthermic treatment of cancer under an alternating magnetic field. *J*. *Mater*. *Sci*. *Mater*. *Med*. **2008,** *19*, 1897-1903.

202. Vegerhof, A.; Motei, M.; Rudinzky, A.; Malka, D.; Popovtzer, R.; Zalevsky, Z., Thermal therapy with magnetic nanoparticles for cell destruction. *Biomed*. *Opt*. *Express* **2016,** *7*, 4581-4594.

203. Huang, X.; El-Sayed, M. A., Gold nanoparticles: optical properties and implementations in cancer diagnosis and photothermal therapy. *J*. *Adv*. *Res*. **2010,** *1*, 13-28.

204. Mendes, R.; Pedrosa, P.; Lima, J. C.; Fernandes, A. R.; Baptista, P. V., Photothermal enhancement of chemotherapy in breast cancer by visible irradiation of Gold Nanoparticles. *Sci. Rep.* **2017,** *7*, 10872.

205. Zhu, Y.; Dürr, H., The future of electron microscopy. *Phys. Today* **2015,** *68*, 32-38.

206. Ghosh, P.; Han, G.; De, M.; Kim, C. K.; Rotello, V. M., Gold nanoparticles in delivery applications. *Adv Drug Deli. Rev.* **2008,** *60*, 1307-15.

207. Boisselier, E.; Astruc, D., Gold nanoparticles in nanomedicine: preparations, imaging, diagnostics, therapies and toxicity. *Chem. Soc. Rev.* **2009,** *38*, 1759-82.

208. Rankin, N. J.; Preiss, D.; Welsh, P.; Burgess, K. E. V.; Nelson, S. M.; Lawlor, D. A.; Sattar, N., The emergence of proton nuclear magnetic resonance metabolomics in the cardiovascular arena as viewed from a clinical perspective. *Atherosclerosis* **2014,** *237*, 287-300.

209. Riss, T.L.; Moravec, R. A.; Niles, A. L.; Benink, H.A.; Worzella, T. J.; Minor, L., Assay guidance manual: cell viability assays. Bethesda (MD): Eli Lilly & Company and the National Center for Advancing Translational Sciences; **2004**.

210. Jin, R., Quantum sized, thiolate-protected gold nanoclusters. *Nanoscale* **2010,** *2*, 343-362.

211. Zhu, M.; Aikens, C. M.; Hollander, F. J.; Schatz, G. C.; Jin, R., Correlating the Crystal Structure of A Thiol-Protected Au25 Cluster and Optical Properties. *J. Am. Chem. Soc.* **2008,** *130*, 5883-5885.

212. Turkevich, J., Colloidal gold. Part I. *Gold Bull.* **1985,** *18*, 86-91.

213. Martin, M. N.; Basham, J. I.; Chando, P.; Eah, S.-K., Charged Gold Nanoparticles in Non-Polar Solvents: 10-min Synthesis and 2D Self-Assembly. *Langmuir* **2010,** *26*, 7410-7417.

214. Ohyama, J.; Hitomi, Y.; Higuchi, Y.; Tanaka, T., Size Controlled Synthesis of Gold Nanoparticles by Porphyrin with Four Sulfur Atoms. *Top. Catal.* **2009,** *52*, 852-859.

215. Briñas, R. P.; Hu, M.; Qian, L.; Lymar, E. S.; Hainfeld, J. F., Gold Nanoparticle Size Controlled by Polymeric Au(I) Thiolate Precursor Size. *J. Am. Chem. Soc.* **2008,** *130*, 975-982.

216. Aldeek, F.; Muhammed, M. A. H.; Palui, G.; Zhan, N. Q.; Mattoussi, H., Growth of Highly Fluorescent Polyethylene Glycol- and Zwitterion-Functionalized Gold Nanoclusters. *ACS Nano* **2013,** *7*, 2509-2521.

217. La Torre, A.; Fay, M. W.; Rance, G. A.; Gimenez-Lopez, M. d. C.; Solomonsz, W. A.; Brown, P. D.; Khlobystov, A. N., Interactions of Gold Nanoparticles with the Interior of Hollow Graphitized Carbon Nanofibers. *Small* **2012,** *8*, 1222-1228.

218. Mie, G., Beiträge zur Optik trüber Medien, speziell kolloidaler Metallösungen. *Ann. Phys. (Berlin, Ger.)* **1908,** *330*, 377-445.

219. Zhou, M.; Zeng, C.; Chen, Y.; Zhao, S.; Sfeir, M. Y.; Zhu, M.; Jin, R., Evolution from the plasmon to exciton state in ligand-protected atomically precise gold nanoparticles. *Nat. Commun.* **2016,** *7*, 13240.

220. Song, Y.; Huang, T.; Murray, R. W., Heterophase ligand exchange and metal transfer between monolayer protected clusters. *J. Am. Chem. Soc.* **2003,** *125* (38), 11694-11701.

221. Smith, A. M.; Marbella, L. E.; Johnston, K. A.; Hartmann, M. J.; Crawford, S. E.; Kozycz, L. M.; Seferos, D. S.; Millstone, J. E., Quantitative analysis of thiolated ligand exchange on gold nanoparticles monitored by 1H NMR spectroscopy. *Anal. Chem.* **2015,** *87*, 2771-2778.

222. Susumu, K.; Mei, B. C.; Mattoussi, H., Multifunctional ligands based on dihydrolipoic acid and polyethylene glycol to promote biocompatibility of quantum dots. *Nat. Protoc.* **2009,** *4*, 424-436.

223. Yang, Y.; Nan, J.; Hou, J.; Yu, B.; Zhao, T.; Xu, S.; Lv, S.; Zhang, H., Cytotoxicity of gold nanoclusters in human liver cancer cells. *Int. J. Nanomed.* **2014,** *9*, 5441-5448.

224. Mishra, P.; Nayak, B.; Dey, R. K., PEGylation in anti-cancer therapy: an overview. *Asian J. Pharm. Sci.* **2016,** *11*, 337-348.

225. O'Neal, D. P.; Hirsch, L. R.; Halas, N. J.; Payne, J. D.; West, J. L., Photo-thermal tumor ablation in mice using near infrared-absorbing nanoparticles. *Cancer Lett.* **2004,** *209*, 171-176.

226. Lee, M.; Kim, S. W., Polyethylene glycol-conjugated copolymers for plasmid DNA delivery. *Pharm. Res.* **2005,** *22*, 1-10.

227. Mei, B. C.; Susumu, K.; Medintz, I. L.; Mattoussi, H., Polyethylene glycol-based bidentate ligands to enhance quantum dot and gold nanoparticle stability in biological media. *Nat. Protoc.* **2009,** *4*, 412-423.

228. Zhang, F.; Zhang, S.; Pollack, S. F.; Li, R.; Gonzalez, A. M.; Fan, J.; Zou, J.; Leininger, S. E.; Pavía-Sanders, A.; Johnson, R.; Nelson, L. D.; Raymond, J. E.; Elsabahy, M.; Hughes, D. M. P.; Lenox, M. W.; Gustafson, T. P.; Wooley, K. L., Improving paclitaxel delivery: in vitro and in vivo characterization of PEGylated polyphosphoester-based nanocarriers. *J*. *Am*. *Chem*. *Soc*. **2015,** *137*, 2056-2066.

229. Zeng, C.; Liu, C.; Chen, Y.; Rosi, N. L.; Jin, R., Gold-Thiolate Ring as a Protecting Motif in the Au-20(SR)(16) Nanocluster and Implications. *J. Am. Chem. Soc.* **2014,** *136*, 11922-11925.

230. Chang, H.-C.; Chang, Y.-F.; Fan, N.-C.; Ho, J.-a. A., Facile Preparation of High-Quantum-Yield Gold Nanoclusters: Application to Probing Mercuric Ions and Biothiols. *ACS Appl. Mater. Interfaces* **2014,** *6*, 18824-18831.

231. Maity, P.; Tsunoyama, H.; Yamauchi, M.; Xie, S.; Tsukuda, T., Organogold Clusters Protected by Phenylacetylene. *J. Am. Chem. Soc.* **2011,** *133*, 20123-20125.

232. Tsunoyama, H.; Sakurai, H.; Tsukuda, T., Size effect on the catalysis of gold clusters dispersed in water for aerobic oxidation of alcohol. *Chem. Phys. Lett.* **2006,** *429*, 528-532.

233. Hu, X.; Cho, S.-P.; Takai, O.; Saito, N., Rapid Synthesis and Structural Characterization of Well-Defined Gold Clusters bySolution Plasma Sputtering. *Cryst. Growth Des.* **2012,** *12*, 119-123.

234. Joseph, D.; Geckeler, K. E., Synthesis of highly fluorescent gold nanoclusters

using egg white proteins. *Colloids Surf., B* **2014,** *115*, 46-50.

235. Kanaoka, S.; Yagi, N.; Fukuyama, Y.; Aoshima, S.; Tsunoyama, H.; Tsukuda, T.; Sakurai, H., Thermosensitive gold nanoclusters stabilized by well-defined vinyl ether star polymers: Reusable and durable catalysts for aerobic alcohol oxidation. *J. Am. Chem. Soc.* **2007,** *129*, 12060.

236. Bertino, M. F.; Sun, Z.-M.; Zhang, R.; Wang, L.-S., Facile Syntheses of Monodisperse Ultrasmall Au Clusters. *J. Phys. Chem. B* **2006,** *110*, 21416-21418.

237. Das, A.; Liu, C.; Zeng, C.; Li, G.; Li, T.; Rosi, N. L.; Jin, R., Cyclopentanethiolato-Protected Au-36(SC5H9)(24) Nanocluster: Crystal Structure and Implications for the Steric and Electronic Effects of Ligand. *J. Phys. Chem. A* **2014,** *118*, 8264-8269.

238. Kawasaki, H.; Kumar, S.; Li, G.; Zeng, C.; Kauffman, D. R.; Yoshimoto, J.; Iwasaki, Y.; Jin, R., Generation of Singlet Oxygen by Photoexcited Au-25(SR)(18) Clusters. *Chem. Mater.* **2014,** *26*, 2777-2788.

239. Hu, X. L.; Takai, O.; Saito, N., Synthesis of gold nanoparticles by solution plasma sputtering in various solvents. *J. Phys.: Conf. Ser.* **2013,** *417*, 012030.

240. Zhao, S.; Ramakrishnan, G.; Su, D.; Rieger, R.; Koller, A.; Orlov, A., Novel photocatalytic applications of sub-nanometer gold particles for environmental liquid and gas phase reactions. *Appl. Catal., B* **2011,** *104*, 239-244.

241. Shen, P.; Zhao, S.; Su, D.; Li, Y.; Orlov, A., Outstanding activity of sub-nm Au clusters for photocatalytic hydrogen production. *Appl. Catal., B* **2012,** *126*, 153-160.

242. Liu, Y.; Tsunoyama, H.; Akita, T.; Tsukuda, T., Preparation of ∼1 nm Gold Clusters Confined within Mesoporous Silica and Microwave-Assisted Catalytic Application for Alcohol Oxidation. *J. Phys. Chem. C* **2009,** *113*, 13457-13461.

243. Rodríguez, G. R. C.; Gauthier, G. H.; Ladeira, L. O.; Cala, J. A. S.; Cataño, D. L., Effect of pH and chloroauric acid concentration on the geometry of gold nanoparticles obtained by photochemical synthesis. *J. Phy.: Conf. Ser.* **2017,** *935*, 012027-012032.

244. Hinterwirth, H.; Kappel, S.; Waitz, T.; Prohaska, T.; Lindner, W.; Lämmerhofer,

M., Quantifying Thiol Ligand Density of Self-Assembled Monolayers on Gold Nanoparticles by Inductively Coupled Plasma–Mass Spectrometry. *ACS Nano* **2013,** *7*, 1129-1136.

245. Gao, J.; Huang, X.; Liu, H.; Zan, F.; Ren, J., Colloidal stability of gold nanoparticles modified with thiol compounds: bioconjugation and application in cancer cell imaging. *Langmuir* **2012,** *28*, 4464-4471.

246. Erdevig, H. E.; Russek, S. E.; Carnicka, S.; Stupic, K. F.; Keenan, K. E., Accuracy of magnetic resonance based susceptibility measurements. *AIP Advances* **2017,** *7*, 056718.

247. Hernandez, S. C., Measuring the size dependence of the magnetic properties of alkanethiol-coated gold nanocrystals. In *NNIN REU 2006 APS Conference*, Microelectronics Research Center, The University of Texas at Austin **2006**; 66-67.

248. Clore, G. M.; Iwahara, J., Theory, practice and applications of paramagnetic relaxation enhancement for the characterization of transient low-population states of biological macromolecules and their complexes. *Chem. Rev.* **2009,** *109*, 4108-4139.

249. Zhao, X. B.; Li, H.; Lee, R. J., Targeted drug delivery via folate receptors. *Expert Opin. Drug Deliv.* **2008,** *5*, 309-319.

250. Marchetti, C.; Palaia, I.; Giorgini, M.; De Medici, C.; Iadarola, R.; Vertechy, L.; Domenici, L.; Di Donato, V.; Tomao, F.; Muzii, L.; Panici, P. B., Targeted drug delivery via folate receptors in recurrent ovarian cancer: a review. *OncoTargets Ther.* **2014,** *7*, 1223-1236.

251. Sheikh, U. N.; Cohen, C.; Siddiqui, M. T., Utility of Folate Receptor Alpha Immunohistochemistry in Cytology Specimens of Metastatic Breast Carcinoma, Metastatic Serous Carcinoma of Mullerian Origin, and Primary Lung Adenocarcinoma. *Diagn. Cytopathol.* **2016,** *44*, 369-376.

252. Zhao, R.; Diop-Bove, N.; Visentin, M.; Goldman, I. D., Mechanisms of membrane transport of folates into cells and across epithelia. *Annu. Rev. Nutr.* **2011,** *31*, 177-201.

253. Kurosaki, A.; Hasegawa, K.; Kato, T.; Abe, K.; Hanaoka, T.; Miyara, A.; O'Shannessy, D. J.; Somers, E. B.; Yasuda, M.; Sekino, T.; Fujiwara, K., Serum folate receptor alpha as a biomarker for ovarian cancer: Implications for diagnosis, prognosis and predicting its local tumor expression. *Int. J. Cancer* **2016,** *138*, 1994-2002.

254. Li, H.; Cheng, Y.; Liu, Y.; Chen, B., Fabrication of folic acid-sensitive gold nanoclusters for turn-on fluorescent imaging of overexpression of folate receptor in tumor cells. *Talanta* **2016,** *158*, 118-124.

255. Cheng, W.; Liang, C.; Wang, X.; Tsai, H.-i.; Liu, G.; Peng, Y.; Nie, J.; Huang, L.; Mei, L.; Zeng, X., A drug-self-gated and tumor microenvironment-responsive mesoporous silica vehicle: "four-in-one" versatile nanomedicine for targeted multidrug-resistant cancer therapy. *Nanoscale* **2017,** *9*, 17063-17073.

256. Chen, Q.; Zheng, J.; Yuan, X.; Wang, J.; Zhang, L., Folic acid grafted and tertiary amino based pH-responsive pentablock polymeric micelles for targeting anticancer drug delivery. *Mater*. *Sci*. *Eng*., *C* **2018,** *82*, 1-9.

257. Lu, Y. J.; Sega, E.; Leamon, C. P.; Low, P. S., Folate receptor-targeted immunotherapy of cancer: mechanism and therapeutic potential. *Adv. Drug Deli. Rev.* **2004,** *56*, 1161-1176.

258. Nair, D. P.; Podgórski, M.; Chatani, S.; Gong, T.; Xi, W.; Fenoli, C. R.; Bowman, C. N., The thiol-michael addition click reaction: a powerful and widely used tool in materials chemistry. *Chem. Mater.* **2014,** *26*, 724-744.

259. Sun, Y.; Liu, H.; Cheng, L.; Zhu, S.; Cai, C.; Yang, T.; Yang, L.; Ding, P., Thiol Michael addition reaction: a facile tool for introducing peptides into polymer-based gene delivery systems. *Polym*. *Int*. **2018,** *67*, 25-31.

260. Qian, H.; Zhu, M.; Wu, Z.; Jin, R., Quantum sized gold nanoclusters with atomic precision. *Acc*. *Chem*. *Res*. **2012,** *45*, 1470-1479.

261. Zeng, C.; Qian, H.; Li, T.; Li, G.; Rosi, N. L.; Yoon, B.; Barnett, R. N.; Whetten, R. L.; Landman, U.; Jin, R., Total Structure and Electronic Properties of the Gold Nanocrystal Au36(SR)24. *Angew*. *Chem*. *Int*. *Ed*. **2012,** *51*, 13114-13118.

262. Yu, C.; Li, G.; Kumar, S.; Kawasaki, H.; Jin, R., Stable Au-25(SR)(18)/TiO2 Composite Nanostructure with Enhanced Visible Light Photocatalytic Activity. *J*. *Phys*. *Chem*. *Lett*. **2013,** *4*, 2847-2852.

263. Kauffman, D. R.; Alfonso, D.; Matranga, C.; Qian, H.; Jin, R., A Quantum Alloy: The Ligand-Protected Au25-xAgx(SR)(18) Cluster. *J. Phys. Chem. C* **2013,** *117*, 7914-7923.

264. Xu, Q.; Kumar, S.; Jin, S.; Qian, H.; Zhu, M.; Jin, R., Chiral 38-Gold- Atom Nanoclusters: Synthesis and Chiroptical Properties. *Small* **2014,** *10*, 1008-1014.

265. Li, G.; Jiang, D.-e.; Kumar, S.; Chen, Y.; Jin, R., Size dependence of atomically precise gold nanoclusters in chemoselective hydrogenation and active site structure. *ACS Catal.* **2014,** *4*, 2463-2469.

266. Tyagi, A.; Penzkofer, A., Fluorescence spectroscopic behaviour of folic acid. *Chem. Phys.* **2010,** *367*, 83-92.

267. Wu, Z.; Li, X.; Hou, C.; Qian, Y., Solubility of folic acid in water at pH values between 0 and 7 at temperatures (298.15, 303.15, and 313.15) K. *J. Chem. Eng. Data* **2010,** *55*, 3958-3961.

268. Day, B. P. F.; Gregory, J. F., Thermal stability of folic acid and 5-methyltetrahydrofolic acid in liquid model food systems. *J. Food Sci.* **1983,** *48*, 581-587.

269. Gazzali, A. M.; Lobry, M.; Colombeau, L.; Acherar, S.; Azaïs, H.; Mordon, S.; Arnoux, P.; Baros, F.; Vanderesse, R.; Frochot, C., Stability of folic acid under several parameters. *Eur*. *J*. *Pharm*. *Sci*. **2016,** *93*, 419-430.

270. Paine-Wilson, B.; Chen, T. S., Thermal destruction of folacin: Effect of pH and buffer ions. *J. Food Sci.* **1979,** *44*, 717-722.

271. Satterlee, J. D., Fundamental concepts of NMR in paramagnetic systems part I: the isotropic shift. *Concepts Magn*. *Reso*. **1990,** *2*, 69-79.

272. Goodman, C. M.; McCusker, C. D.; Yilmaz, T.; Rotello, V. M., Toxicity of Gold

Nanoparticles Functionalized with Cationic and Anionic Side Chains. *Bioconjugate Chem.* **2004,** *15*, 897-900.

273. TEShukla, R.; Bansal, V.; Chaudhary, M.; Basu, A.; Bhonde, R. R.; Sastry, M., Biocompatibility of gold nanoparticles and their endocytotic fate inside the cellular compartment: A microscopic overview. *Langmuir* **2005,** *21*, 10644-10654.

274. Li, H.; Zhu, W.; Wan, A.; Liu, L., The mechanism and application of the protein-stabilized gold nanocluster sensing system. *Analyst* **2017,** *142*, 567-581.

275. Tsoli, M.; Kuhn, H.; Brandau, W.; Esche, H.; Schmid, G., Cellular Uptake and Toxicity of Au55 Clusters. *Small* **2005,** *1*, 841-844.

276. Walkey, C. D.; Olsen, J. B.; Guo, H.; Emili, A.; Chan, W. C. W., Nanoparticle size and surface chemistry determine serum protein adsorption and macrophage uptake. *J*. *Am*. *Chem*. *Soc*. **2012,** *134*, 2139-2147.

277. Ahn, S.; Seo, E.; Kim, K.; Lee, S. J., Controlled cellular uptake and drug efficacy of nanotherapeutics. *Sci. Rep.* **2013,** *3*, 1997.

278. Zhang, X.-D.; Wu, D.; Shen, X.; Liu, P.-X.; Yang, N.; Zhao, B.; Zhang, H.; Sun, Y.-M.; Zhang, L.-A.; Fan, F.-Y., Size-dependent in vivo toxicity of PEG-coated gold nanoparticles. *Int*. *J*. *Nanomed*. **2011,** *6*, 2071-2081.

279. White, C. A.; Kennedy, J. F., Methods of enzymatic analysis. *Br*. *Polym*. *J*. **1985,** *17*, 379-379.

280. Leopold, L. F.; Tódor, I. S.; Diaconeasa, Z.; Rugină, D.; Ştefancu, A.; Leopold, N.; Coman, C., Assessment of PEG and BSA-PEG gold nanoparticles cellular interaction. *Colloids Surf*. *Physicochem*. *Eng*. *Aspects* **2017,** *532*, 70-76.

281. Necela, B. M., Folate receptor-α (FOLR1) expression and function in triple negative tumors. *PLoS One* **2015,** *10*.e0127133

282. Yang, T.; Xu, F.; Fang, D.; Chen, Y., Targeted Proteomics Enables Simultaneous Quantification of Folate Receptor Isoforms and Potential Isoform-based Diagnosis in Breast Cancer. *Sci*. *Rep*. **2015,** *5*, 16733.

283. Borghei, Y.-S.; Hosseini, M.; Dadmehr, M.; Hosseinkhani, S.; Ganjali, M. R.; Sheikhnejad, R., Visual detection of cancer cells by colorimetric aptasensor based on aggregation of gold nanoparticles induced by DNA hybridization. *Anal. Chim. Acta* **2016,** *904*, 92-97.

284. Shi, J. J.; Wang, B. H.; Chen, Z. Y.; Liu, W.; Pan, J. J.; Hou, L.; Zhang, Z. Z., A Multi-Functional Tumor Theranostic Nanoplatform for MRI Guided Photothermal-Chemotherapy. *Pharm. Res.* **2016,** *33*, 1472-1485.

285. Mansoori, G. A.; Brandenburg, K. S.; Shakeri-Zadeh, A., A Comparative Study of Two Folate-Conjugated Gold Nanoparticles for Cancer Nanotechnology Applications. *Cancers* **2010,** *2*, 1911-1928.

286. Ding, L.; Li, J.; Huang, R.; Liu, Z.; Li, C.; Yao, S.; Wang, J.; Qi, D.; Li, N.; Pi, J., Salvianolic acid B protects against myocardial damage caused by nanocarrier TiO(2); and synergistic anti-breast carcinoma effect with curcumin via codelivery system of folic acid-targeted and polyethylene glycol-modified TiO(2) nanoparticles. *Int. J. Nanomed.* **2016,** *11*, 5709-5727.

287. Kumar, S. S. D.; Mahesh, A.; Antoniraj, M. G.; Rathore, H. S.; Houreld, N. N.; Kandasamy, R., Cellular imaging and folate receptor targeting delivery of gum kondagogu capped gold nanoparticles in cancer cells. *Int. J. Biol. Macromol.* **2018,** *109*, 220-230.

288. Chen, H.; Li, S.; Li, B.; Ren, X.; Li, S.; Mahounga, D. M.; Cui, S.; Gu, Y.; Achilefu, S., Folate-modified gold nanoclusters as near-infrared fluorescent probes for tumor imaging and therapy. *Nanoscale* **2012,** *4* , 6050-6064.

289. Hou, Z.; Gattoc, L.; Connor, C.; Yang, S.; Wallace-Povirk, A.; George, C.; Orr, S.; Polin, L.; White, K.; Kushner, J.; Morris, R. T.; Gangjee, A.; Matherly, L. H., Dual Targeting of Epithelial Ovarian Cancer Via Folate Receptor α and the Proton-Coupled Folate Transporter with 6-Substituted Pyrrolo[2,3-*d*]pyrimidine Antifolates. *Mol. Cancer Ther.* **2017,** *16*, 819.

Appendix Information

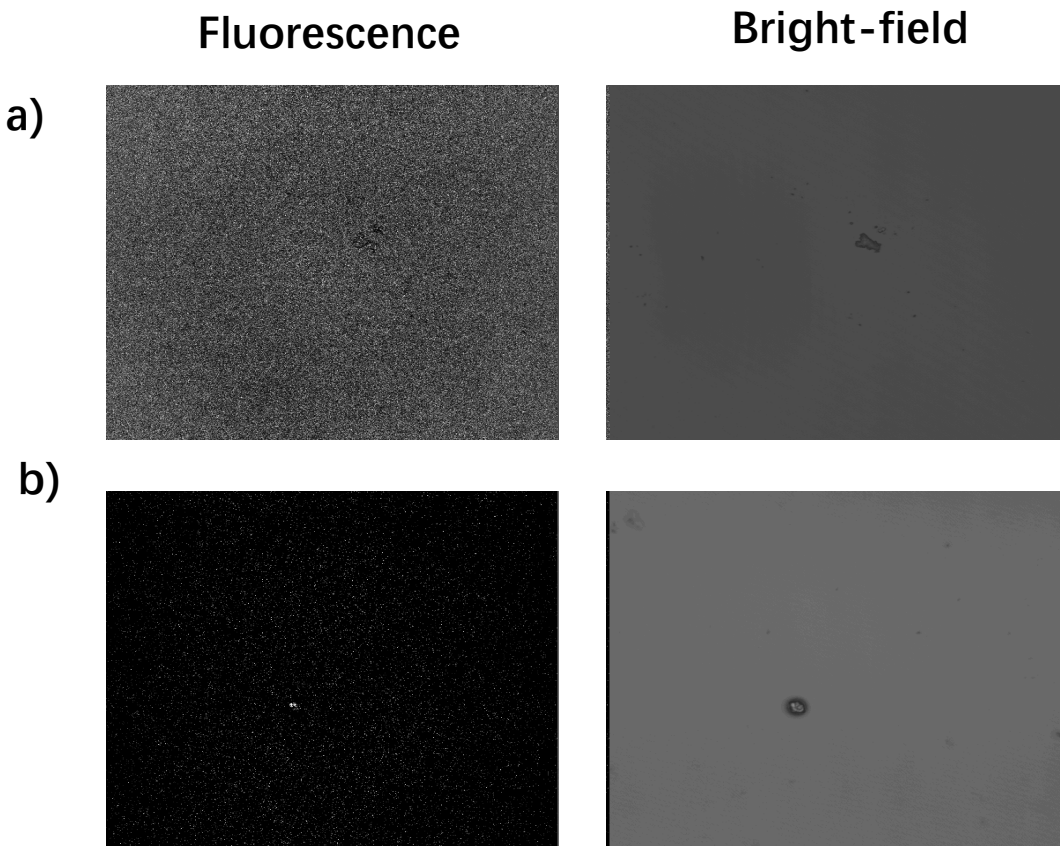

Figure A.1 Confocal imaging of **(a)** FA-PEG-TA ligands **(b)** FA-Au NCs; left images show emission recorded under excitation of 405nm. Right are corresponding bright field images (image full size is 100 μm).

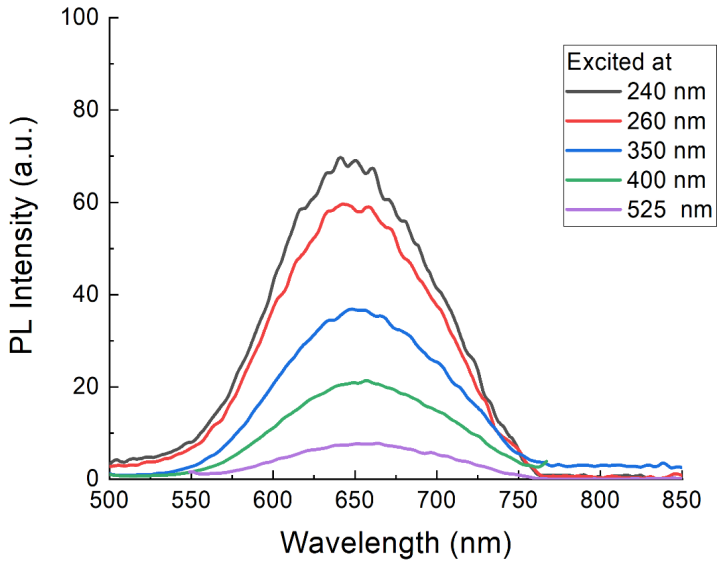

Figure A.2 Photoluminescence spectra of TA-PEG-OCH_3 capped AuNCs.

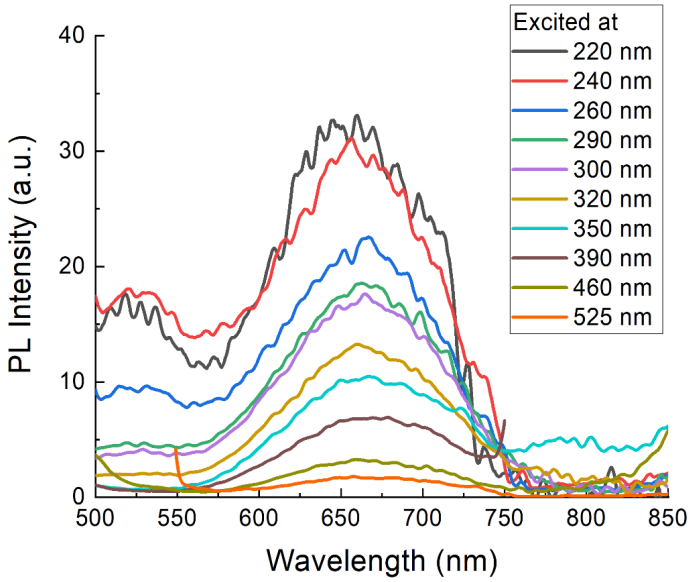

Figure A.3 Photoluminescence spectra of TA-PEG-NH_2 capped AuNCs.

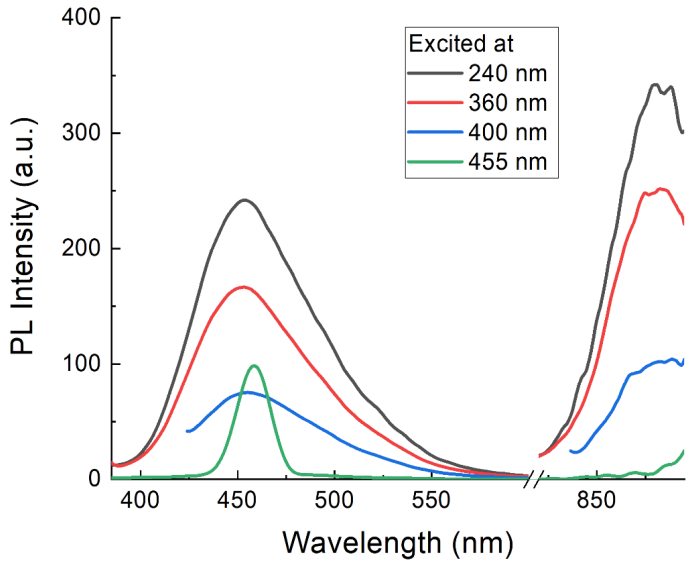

Figure A.4 Photoluminescence spectra of FA-NH-PEG-TA capped AuNCs.

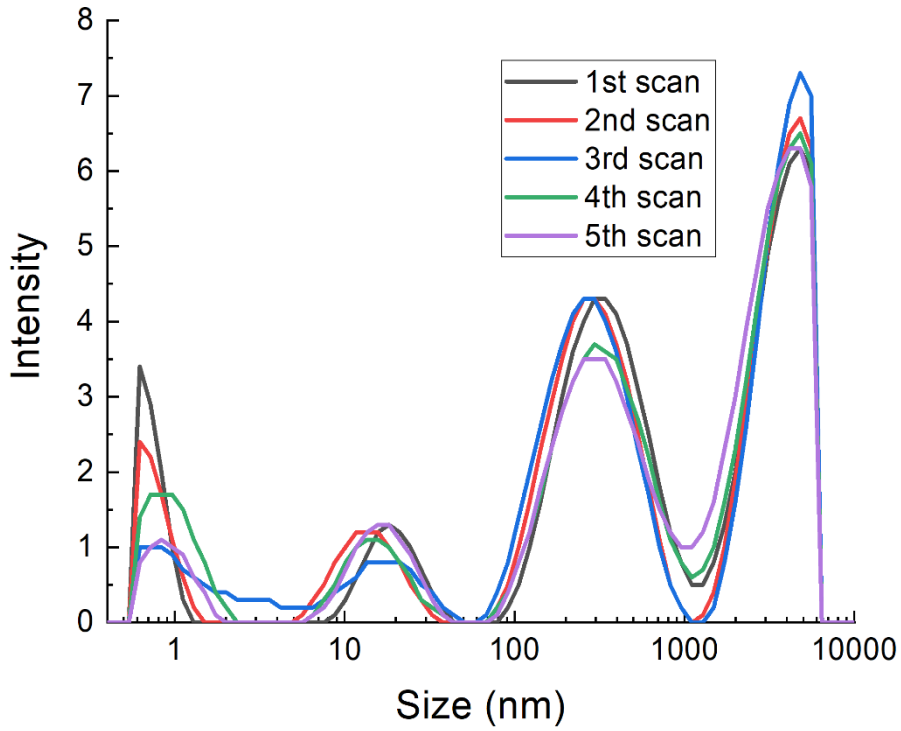

Figure A.5 Dynamic light scattering spectra of TA-PEG-OCH_3 capped AuNCs

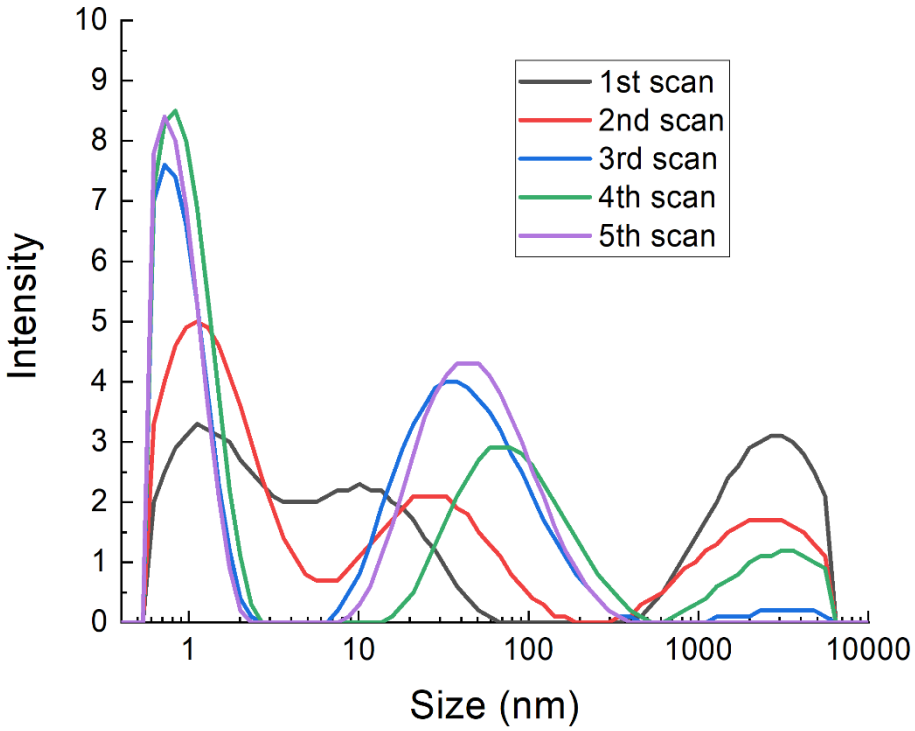

Figure A.6 Dynamic light scattering spectra of TA-PEG-NH_2 capped AuNCs

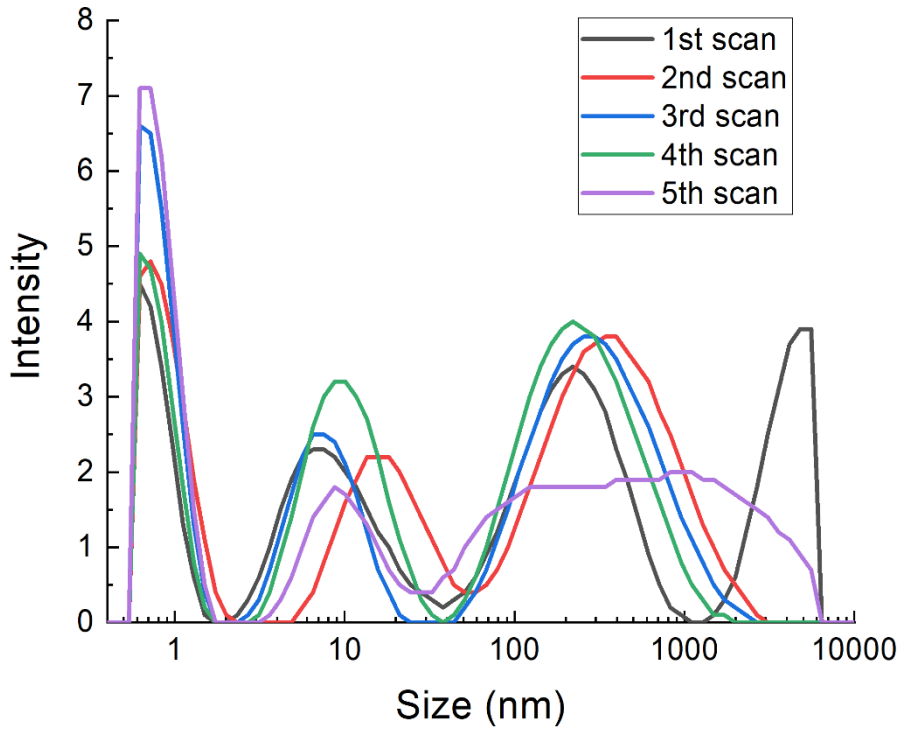

Figure A.7 Dynamic light scattering spectra of FA-NH-PEG-TA capped AuNCs